12 RESEARCH AND DEVELOPMENT PROGAM

12.1 Introduction

The overall NSLS-II design philosophy is to use low-risk technology, requiring minimum research and development, to achieve the facility's baseline performance while, at the same time, having significant upgrade potential. Use of electron storage rings for photon production is a proven technology, and well understood; however, extending that technology to achieve unprecedented levels of brightness, flux, and stability imposes some technical risk. The major procurements require only limited R&D and present low technical risk. There are no known technical "show stoppers" in constructing NSLS-II.

R&D will be conducted in areas where opportunities exist for mitigating existing technical risk, achieving cost reductions, and/or enhancing performance. The following seven main areas have been identified for R&D:

- high spatial resolution optics
- nanopositioning instrumentation
- high energy resolution optics
- metrology and reflective optics
- advanced detectors
- advanced insertion devices
- stabilization of magnet–girder support systems

The R&D program for the first six items is described in this chapter. The R&D plan for the last item is described in Section 7.2.3.9. In addition to these principle R&D areas, there will also be important, but smaller scale, R&D efforts in several other areas. These are described in the appropriate sections of this CDR.

The R&D efforts supported by the NSLS-II project are targeted at meeting the needs of specific project deliverables. In the case of R&D related to experimental facilities, the approach taken is to first identify the specific technical requirements and then develop a solution to meet that defined need. In the case of the program on mirrors and detectors, these needs are expected to vary greatly depending on the specific experiment. Therefore, R&D efforts in these two areas that are specifically required to meet the needs of beamlines that are selected to be constructed out of the experimental facilities trust fund, discussed in Chapter 11, will also be funded out of the trust fund. As such, the initiation of efforts on mirrors and detectors will begin following identification of the suite of project beamlines.

12.2 High-Spatial Resolution Optics

12.2.1 Introduction and Overview

The goal of achieving ever-higher resolution in x-ray focusing is one that has been pursued by the worldwide x-ray optics community with impressive results. As Figure 12.2.1 shows, up until about a decade ago nearly all the progress in submicrometer focusing was accomplished with Fresnel zone plates as soft x-ray (<1 keV) optics. However, within the past decade, remarkable advances have been made in the development of a variety of optic types for focusing hard (8–20 keV) x-rays to sub-100 nm spot sizes. To surpass this historical trend and reach a 1 nm resolution target will require sustained effort as part of the NSLS-II project.

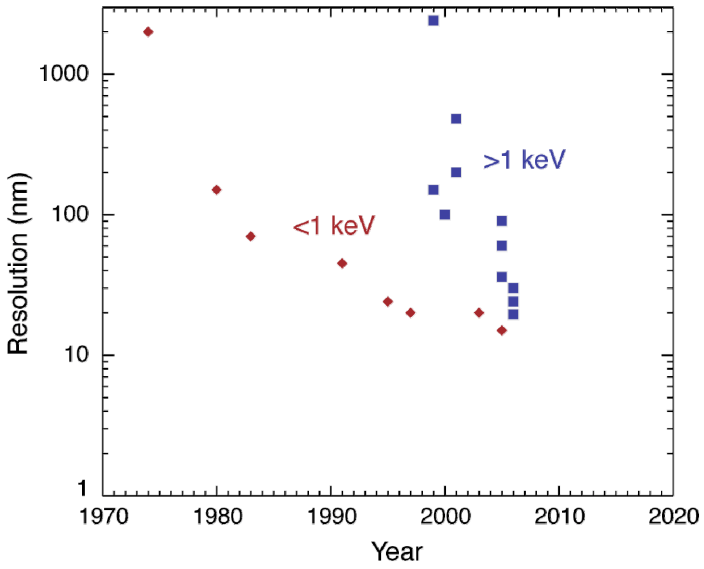

Figure 12.2.1 Historical trends in the best resolution of x-ray optics have involved rapid progress in the initial establishment of focusing techniques for a particular energy range, followed by progress resulting from sustained R&D efforts by the worldwide optics community. For E=1.24 keV, the limiting resolution is 1 nm. For hard x-rays, where we chose a characteristic energy of E=12.4 keV, λ and the limiting resolution is 0.1 nm.

In this section we provide some background on x-ray optics, and examine various possible approaches to achieving 1 nm spatial resolution.

12.2.1.1 Imaging Modes

We first consider the two major types of x-ray imaging systems in use today: those that use optics to form an image by collecting and focusing radiation scattered by an object, full-field imaging, and those that use optics to form a small focus through which the specimen is scanned (Figure 12.2.2). The types of information one can gain, and the requirements on specimen illumination, are very different between these two approaches. Full-field imaging is primarily restricted to transmission imaging, while scanned imaging allows one to use a greater range of signals (energy-resolved fluorescent photons, photo- and Auger-electrons, etc.). The same optics can be used as high-resolution objective lenses for both full-field and scanned image approaches. (There is an important difference: scanning systems can usefully employ optics with large off-axis aberrations, while full-field imaging systems cannot.) Here, we address optics that can produce a small point focus in scanning systems, since the flexibility of imaging signal (fluorescence, microdiffraction, etc.) is of great advantage to many hard x-ray studies of the properties of nanoscale materials.

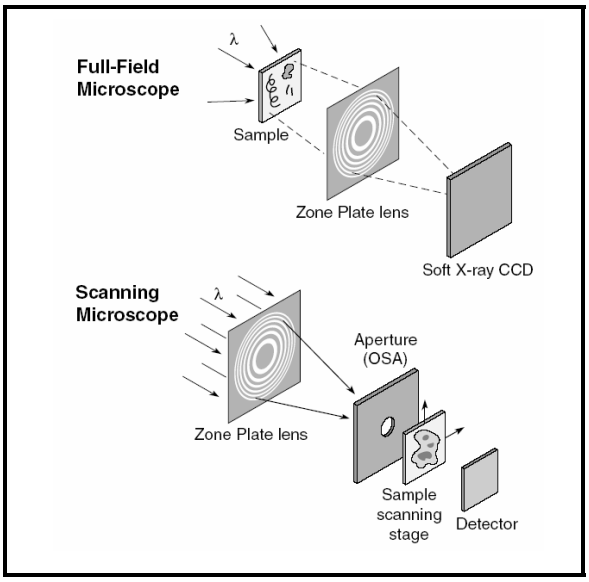

Figure 12.2.2 A schematic of two major kinds of x-ray microscope, the full-field microscope (top) and a scanning microscope (bottom). In the full-field case, the sample is illuminated incoherently, and a high resolution optic is placed downstream of the sample. The sample is imaged pixel by pixel onto the CCD. The scanning microscope has an optic upstream of the sample which is coherently illuminated, creating a small focused spot on the sample. The schematic representations of x-ray microscopes are reproduced with permission from Prof. D.T. Attwood, www.coe.berkeley.edu/AST/sxreuv.

12.2.1.2 X-Ray Interactions with Matter

The optical properties of materials in the photon energy range above about 30 eV are related quite directly to the atomic scattering factors. The index of refraction, n, of a material is typically written as $n = 1-\delta-i\beta$; the parameters δ and β are called the refractive index decrement and the absorption index, respectively. Many of the differences between x-ray and visible light optics are due to three facts 1) the real part of the refractive index $1-\delta$ is less than one, 2) δ is of order 10^{-6}, and 3) the ratio β/δ, which is related to the phase shift induced in an absorption length, is much smaller than for visible optics.

The index of refraction of a material is related to the scattering factors of the individual atoms:

$$n = 1-\delta-i\beta = 1-\frac{r_e}{2\pi}\lambda^2\sum_i n_i f_i = 1-\frac{r_e}{2\pi}\lambda^2\sum_i n_i(f_{1i}+if_{2i}), \qquad (12.2\text{-}1)$$

where r_e is the classical electron radius, λ is the wavelength, and n_i is the number of atoms of type i per unit volume. For photon energies larger than the electron binding energies, f_1 for an element tends to approximately Z, the number of electrons in the atom. f_2 is derived from the atomic photo-absorption cross-section, τ, and is defined as

$$f_2 = \frac{\tau}{2r_e\lambda}. \qquad (12.2\text{-}2)$$

The consequence of δ being small is that even the most dense material deflects x-rays only slightly. The critical angle, which is the maximum deflection angle a single mirror bounce can impart, is given by $\theta_c=\sqrt{(2\delta)}$, and is on the order of 10^{-3}. For both mirrors and refractive optics, this small θ_c results in limitations of the numerical aperture (see discussion below), and limits the resolution for a single optic t order λ/θ_c. As $\theta_c \propto \lambda$, this resolution is independent of energy and simply depends on the electron density of the material. For diffractive optics, the small δ also makes it difficult to fabricate the required zone plate thickness. A 2π phase-shift thickness is λ / δ, which can be in the microns or tens of microns range, making it necessary to fabricate zones that are just microns thick yet nanometers wide—an aspect ratio that is very large and difficult to fabricate.

12.2.1.3 Important Metrics of Focusing Optics

Here, we briefly summarize quantities that can be used to parametrize and compare the different optics; where possible, we estimate values.

12.2.1.3.1 Resolution and Numerical Aperture

As shown in Figure 12.2.3, the transverse resolution of any optic is limited by diffraction from its pupil function; for a circular lens with numerical aperture or semi-angle θ_{NA}, the Rayleigh resolution limit may be given by $\Delta_t = 0.61\lambda/\theta_{NA}$. (Strictly speaking, the numerical aperture is NA = $n\sin\theta_{NA}$, but $n \cong 1$, and for the regime considered here, the approximation NA$\approx \theta_{NA}$ is a good one.) For a wavelength of 0.1 nm, an optic of 1 nm resolution requires a numerical aperture of 0.06.

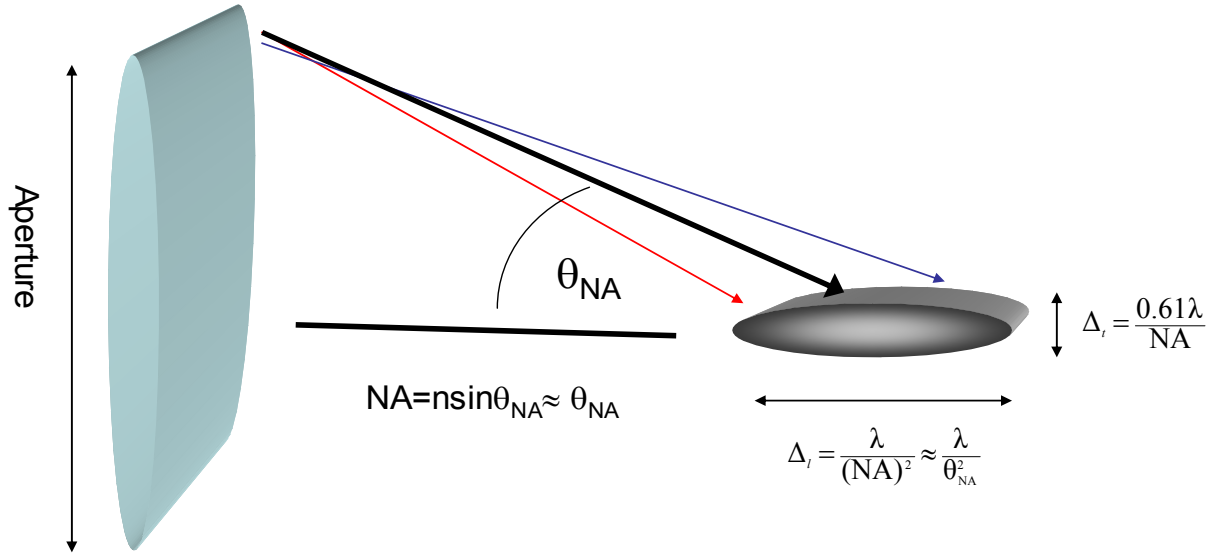

Figure 12.2.3 Illustrating the lens aperture, the numerical aperture (NA), the optics transverse resolution Δ_t, and the longitudinal resolution Δ_l, commonly referred to as depth of focus. Also shown schematically is the effect of a chromatic optic focusing different wavelengths, represented by the red, black, and blue arrows focusing at different focal lengths.

Fabricating hard x-ray optics with such large NA is a challenging task, compared with the state of the art in other methods of microscopy. For visible optical photons, one can commercially purchase microscope objectives with NA as large as 0.7 [12.2.1]. In the extreme ultraviolet with λ = 13.5 nm, a state-of-the-art mirror pair optic for lithography applications [12.2.2] has been constructed with NA = 0.3. For electron microscopes, the NA is on the order of tens of mrad, although here the significantly shorter wavelength compensates for the small NA. In comparison, commercially available zone plates for hard x-ray photons with 50 nm resolution currently have NA $\approx 10^{-3}$.

12.2.1.3.2 Depth of Field (DOF)

The depth of field for a coherently illuminated optic is $\Delta_l = \lambda/(\mathrm{NA})$. For NA of 0.1, we find the DOF is on the order of 10 nm. This sets important constraints on sample manipulators; one needs nm-precision translators of the sample in all directions. Furthermore, for diffraction-limited optics with a transverse resolution of $\Delta_t = 0.61\lambda/\theta$, the depth of focus also can be expressed as $\Delta_t = 2.7\Delta_t(\Delta_t / \lambda)$. Note that the DOF shrinks as the square of the transverse resolution, but grows linearly with photon energy.

12.2.1.3.3 Aperture

The aperture is the actual physical size of the optic, and determines the total photon flux arriving at the lens. It is *f**NA, where *f* is the focal length.

12.2.1.3.4 Efficiency

Most real optics do not have perfect transmission, and will not focus the entire flux incident on the optic into the focal spot. The role that optic efficiency plays is very different in scanning versus full-field imaging experiments. In a full-field imaging system, the optic is located downstream of the specimen; this means that if an optic with efficiency ε and numerical aperture θ is used to collect the photons emerging from the specimen, one will have to expose the specimen to an extra dose of

$$\frac{1}{\varepsilon}\frac{2\pi}{\pi\theta^2} = 2/\left(\varepsilon\theta^2\right) \tag{12.2-3}$$

to collect the same information that would have been obtained by a 100% efficient, 2π collection solid-angle optic. As a result, high efficiency, ε, large numerical aperture θ optics are essential for full-field imaging of radiation-sensitive specimens. In scanned imaging systems, the optic is located upstream of the specimen, so it is the efficiency of the detector that determines whether the specimen must undergo any extra exposure.

12.2.1.3.5 Chromatic Properties

An important characteristic of an optic is its behavior as a function of energy. Some optics have their best efficiencies for particular photon energies. For example, solid metal mirrors are relatively achromatic up to a critical energy before this efficiency drops off. Also, for solid metal mirrors the position of the focus is independent of energy. For zone plate optics the focal length varies with photon energy, and for purely refractive optics the focal length varies as the square of the photon energy.

12.2.1.3.6 Modulation Transfer Function

As Figure 12.2.4 shows, it is important to consider the fraction of energy that is delivered outside of the central focus, as that can lead to incorrect interpretation because information from other regions is mixed in with information from the selected area. The Modulation Transfer Function is a metric that allows one to compare quantitatively the spectral response of an optic. MTF is defined as the power recorded at a given spatial frequency, divided by the power present in the object at that frequency.

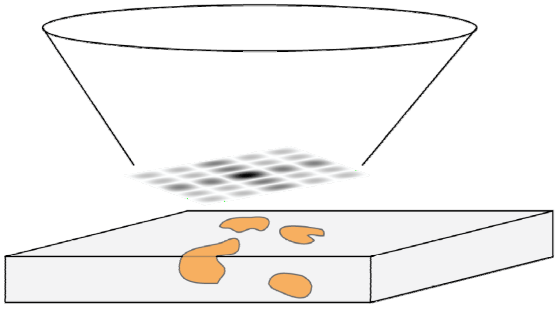

Figure 12.2.4 Illustration of the importance of having a "clean" central focus with minimal sidelobes for quantitative studies of heterogeneous materials. Excessive energy in the sidelobes can lead to mixing of signals from adjacent sample regions.

12.2.2. Basic Focusing Optics

12.2.2.1 Mirrors

The critical angle for total external reflection can be expressed in terms of a grazing critical angle relative to the surface normal as

$$\theta_C' = \sqrt{2\delta} = \lambda\sqrt{2\alpha f_1} \,. \tag{12.2-4}$$

This indicates that high-density materials and high energies give a slightly higher critical angle. More importantly, however, this relationship sets a fundamental limit to the resolution of reflective optics, because the maximum numerical aperture θ cannot exceed twice the critical angle. As a result, for a cylindrically symmetric reflective mirror, the Rayleigh resolution limit becomes

$$\Delta = 0.22/\sqrt{\alpha f_1} \,. \tag{12.2-5}$$

This limit is plotted for nickel and platinum in Figure 12.2.5.

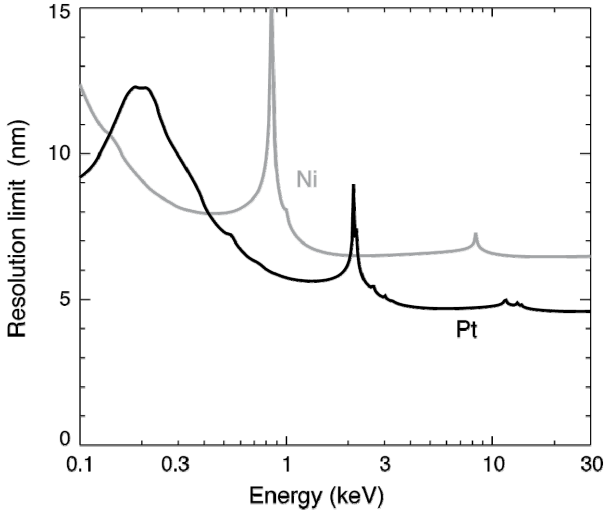

Figure 12.2.5 Theoretical resolution limit for grazing incidence single-bounce reflective optics with perfect figure and finish.

Reflective optical systems have achieved very impressive results for 1D focusing at the 30 nm level, and they have the advantage of being achromatic optics. However, we do not consider them to be a promising path to achieve 1 nm resolution, for several reasons. First, there is the intrinsic single-bounce resolution limit shown in Figure 12.2.6; in principle this could be overcome by using a multiple bounce system, or by using multilayer coatings to increase the critical angle. However, there still remain the challenges of producing the correct figure and finish over a very large optical area (see Figure 12.2.6), properly aligning the optic to avoid off-axis aberrations, and (for multiple-bounce systems) achieving the correct relative alignment of separate mirror segments. In a reflective system, the length of the mirror along the beam direction sets a limit to the lowest spatial frequencies that can contribute to the focus (rays from bottom left in Figure 12.2.6), and reductions in this length have the same effect as increasing the central stop fraction *a* and thereby introducing sidelobes about the central focus (Figure 12.2.4). In contrast, Figure 12.2.6 shows that for a transmission optic, all "ray bending" is accomplished in a more compact area, improving tolerance to fabrication inaccuracies.

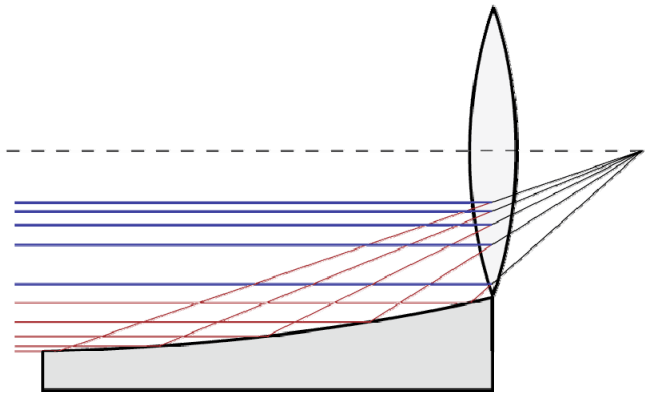

Figure 12.2.6 Illustration of the challenges faced by a reflective optical system relative to a transmission system.

In all sub 100 nm resolution demonstrations of x-ray focusing using reflective optics, anomalously strong sidelobes are observed around the central focus and often a diffuse scattering background signal, as well. For these reasons, we believe that while reflective optics will play a crucial role as achromatic optics at NSLS-II, they do not represent a viable path for 1 nm spatial resolution.

12.2.2.2 Fresnel Zone Plates and Multilayer Laue Lenses

Fresnel zone plates have provided the highest resolution x-ray foci for the past two decades, reaching 15 nm resolution in a recent demonstration [12.2.3]. FZPs are diffractive optics with a grating period $2\Delta_m$ that decreases with zone number n (and also with radius), so that from each local region of the zone plate an incident plane wave undergoes m^{th} order diffraction toward a point focus by an angle $\theta = m\lambda / (2\Delta_m)$, as shown in Figure 12.2.7. (The radius r_n of the nth zone boundary is well approximated by $r_n^2 = n\lambda f$, where f is the focal length).

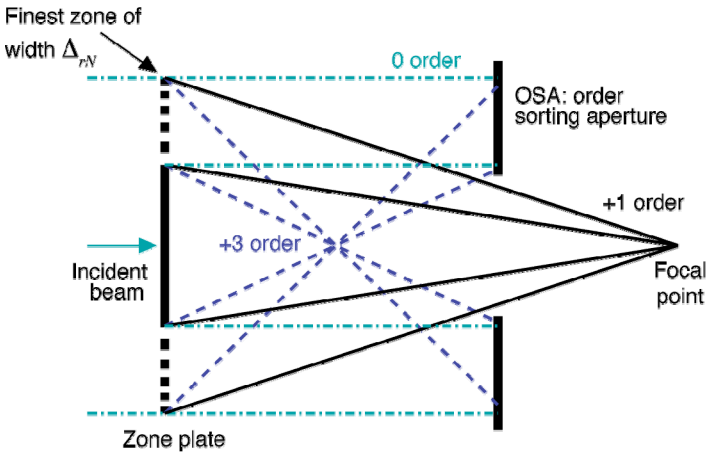

Figure 12.2.7 Schematic of a Fresnel zone plate as used in a scanned imaging configuration, where an order-sorting aperture (OSA) is used to isolate the first-diffraction-order focus.

As a result, the Rayleigh resolution Δ_t is set by the width of the N^{th}, narrowest, outermost zone as

$$\Delta_t = 0.61\lambda/\theta = 1.22\Delta_{rN}/m \,. \qquad (12.2\text{-}6)$$

In addition, the zones must be accurately placed to within about m/3 of their width to avoid phase errors that would otherwise degrade the focal spot. For a zone plate with diameter d, the m^{th} diffraction order focal length is given by

$$f = d\Delta_{rN}/(m\lambda) = d\Delta_t/(1.22\lambda). \tag{12.2-7}$$

The lens diameter required to achieve 1 nm resolution with a focal length of at least 1 mm is shown in Figure 12.2.8.

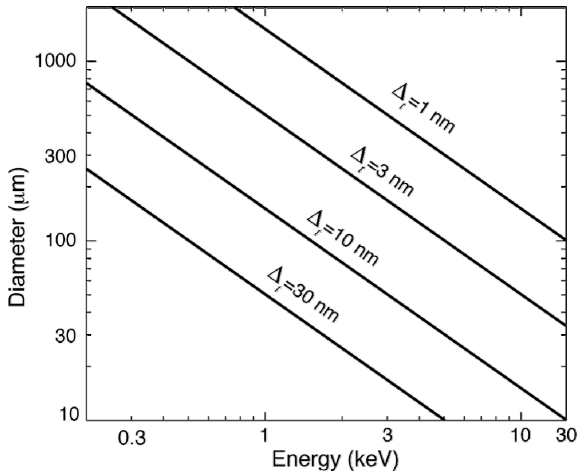

Figure 12.2.8 Diameter required of Fresnel zone plates designed to achieve a given Rayleigh resolution Δ_t as a function of x-ray energy.

The efficiency of thin, binary zone plates can be calculated using a relationship [12.2.4] that takes into account both phase shift and absorption in the zone material (see Figure 12.2.9). In general it is especially favorable to use materials at energies below particular absorption edges, to maximizes the ratio of phase shift to absorption. For energies below 1 keV, thicknesses of ~150 nm of gold or nickel give sufficient efficiency, and for energies above 1 keV, nickel becomes increasingly less practical due to the thicker films with correspondingly less favorable aspect ratios. For photon energies of 10 keV and higher it is more practical to use a high-density material such as gold with a thickness of 500 nm or more.

Most zone plates are fabricated by a process that involves 1) electron beam lithography to define the zone pattern, 2) reactive ion etching to transfer this pattern into a thick polymer plating mold, and 3) electroplating to produce the zone structures themselves. This fabrication procedure presents several challenges. To produce the highest possible resolution, the finest zone width Δ_{rN} must be as fine as possible, yet sidescattering of the electron beam in the photoresist makes lines below 10 nm extremely challenging to produce. At the same time, zones must be thick along the x-ray beam direction (indicated as zone thickness in Figure 12.2.9). This means that very high aspect ratio structures are desired. For 1 nm resolution from a zone plate operated in m=5th order at 10 keV, one would want to fabricate zones with a width of Δ_{rN}=4 nm and a height in gold of at least 600 nm, or an aspect ratio of 150:1. This is far beyond what has been achieved to date, which includes aspect ratios of 8:1 at Δ_{rN}=20 nm [12.2.5] and 14:1 at Δ_{rN}=32 nm [12.2.6]. Finally, the electron beam lithography system must be able to place zones with a 1σ absolute placement accuracy of Δ_{rN}/m over the entire optic diameter. For these reasons, circular zone plates do not appear to be a viable alternative for reaching 1 nm resolution.

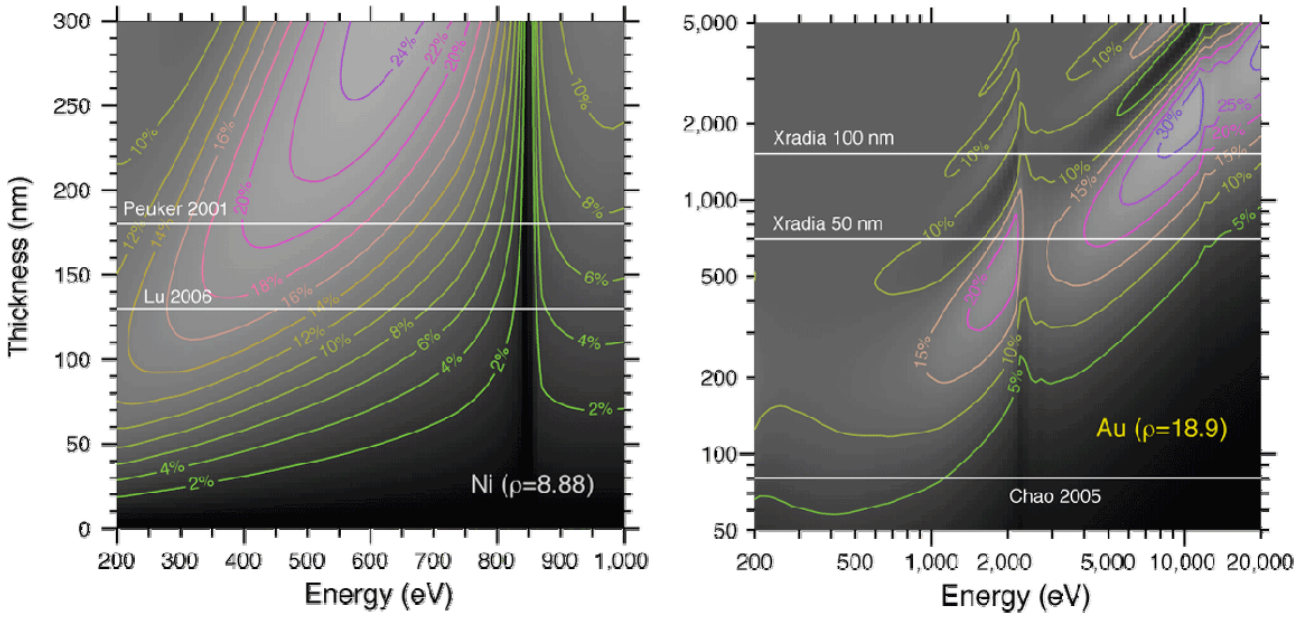

Figure 12.2.9 Diffraction efficiency of thin binary transmission zone plates as a function of material thickness and photon energy, based on the formula by Kirz [12.2.4]. In the soft x-ray range, zone plate thicknesses of 100 nm or more are required to achieve high efficiency, while at 10 keV, thicknesses of 500 nm or higher are required.

The above limitations to electron beam fabrication of zone plates have long been recognized. As early as 1980, Schmahl et al. [12.2.7] proposed an alternative approach to zone plate fabrication: Start with a wire, and deposit alternating layers of high and low-density materials to fabricate a zone plate pattern. The completed structure can then be sliced and thinned to yield a zone plate resembling a slice of a jelly-roll cake (Figure 12.2.10). While a number of researchers have pursued this approach over the years, the results obtained have not been encouraging: it is very difficult to produce a wire of the required roundness, and when sputtering multiple layers, any roughness and thickness errors accumulate to unacceptable values before one reaches the thinnest, resolution-determining outermost layers.

An alternative to this approach was proposed by Maser et al. in 2004 [12.2.8]. Optics of this new type have been given the name of Multilayer Laue Lenses. In MLLs, one starts from the outermost zones and works in. Rather than face the challenge of depositing thin films on the inside curvature of a cylinder with a radius of curvature of some tens of micrometers, a flat substrate is used to produce half of a linear zone plate (Figure 12.2.11). In this way one can start from a well-polished flat surface, with an error accumulation of zero at the thinnest, outermost zone; errors will build up only towards the innermost zones, which are coarser and thus more tolerant.

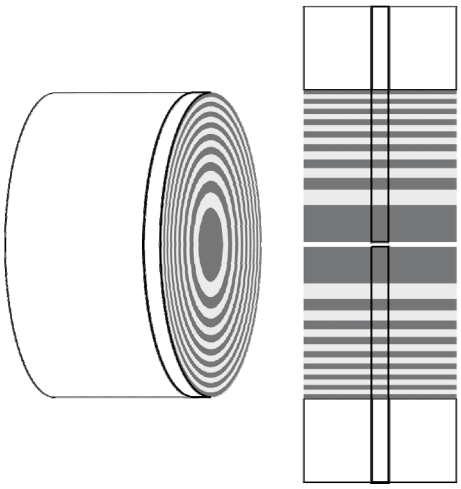

Figure 12.2.10 Sputter-sliced zone plates (left) and multilayer Laue lenses (right). For sputter-sliced zone plates, successive layers are deposited onto a wire in the order of coarser zone to finer zone. For MLL, successive layers are deposited onto a flat substrate in the order of finer zone to coarser zone. In each case, a slice of the structure yields the final optic. In the case of MLL, the result is half of a linear optic, which can be paired with its twin and put with a pair of orthogonal optics to yield a lens with 2D focusing properties.

Each half-linear zone plate produces a line focus, which appears like light coming from a slit; placing two half-linear zone plates next to each other therefore produces a double-slit interference pattern in the far field. As the two half-linear zone plates are brought into registry, the double-slit interference fringes in the far field overlap region become coarser and coarser until they disappear when the two half-linear zone plates are aligned. Since there is no horizontal focusing from the vertically focusing optics and vice versa, an orthogonal pair of half-linear zone plates produces a 2D focus with the characteristics of crossed linear lenses.

Producing zones using thin layer deposition techniques followed by slicing to obtain a zone plate with the desired thickness along the x-ray beam direction, removes any aspect ratio limit in the fabrication. However, the zones are now a volume grating, so that the Bragg condition must be met to yield high diffraction efficiency. For an optic of intermediate thickness, this can be achieved by giving each zone a "wedged" thickness, as shown in Figure 12.2.11. One can also satisfy the Bragg condition over a certain range of zone widths by taking a non-wedged optic and tilting it. This approach has been used by Kang et al. [12.2.9], who have demonstrated a 30 nm line focus at 19.5 keV.

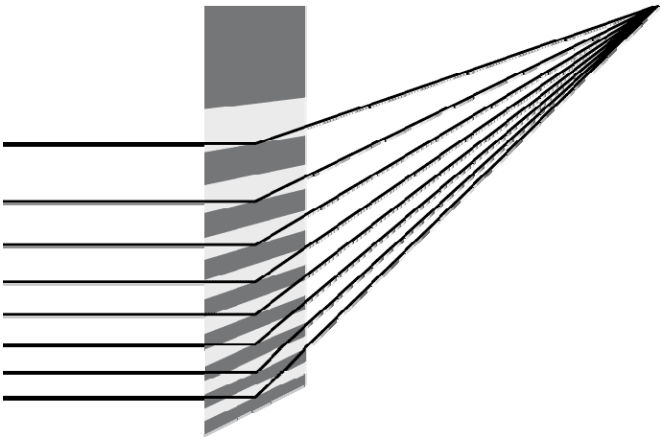

Figure 12.2.11 It is necessary to continuously adjust the tilt of individual zones in a multilayer Laue lens to meet the Bragg condition. We refer to this case (which applies to an optic of intermediate thickness) as having "wedged" zones.

12.2.2.3 Refractive Optics

Refractive optics and compound refractive optics for hard x-rays were discussed as far back as 1948 [12.2.10], but were dismissed at that time as being impractical. For a single refracting surface with a reasonable radius of curvature, since δ is so small, one obtains a relatively long focal length. For example, a 1 cm radius results in a focal length of order 10^4 m. Consequently, it was suggested by three groups independently [12.2.10, 12.2.11, 12.2.12] that compound lenses could bring the focal length down to

reasonable values. To first order, N lenses of focal length f_0 will have an effective focal length of f_0/N. The physical implementation of Snigirev [12.2.12] was a crossed array of cylindrical holes drilled in aluminum. Subsequently, a parabolic profile was suggested as a better approximation of an ideal lens, and this was also implemented [12.2.13].

However, for all practical variations of the refractive optic, absorption limits the aperture. If one considers the familiar parabolic profile with thickness t as a function of y, where y is the distance from the optic axis, then $t=y^2/(2\delta f)$ for a pure refractive optic. The lens absorption as a function of the radial lens coordinate is then given by $\exp(-4\pi\beta t/\lambda)$. One finds that the aperture is limited, and the effective lens aperture is proportional to $\sqrt{f}$. Consequently, the resolution is also proportional to $\sqrt{f}$, resulting in a gain that is dependent only on δ and β.To get a 1 nm spot, one finds for a focal length of order 1 μ an aperture of 100 nm, using silicon as a lens material; this aperture is clearly unacceptable.

12.2.2.4 Waveguides

One possible path to a 1 nm spot size on a sample is to use an optical path that includes a waveguide to serve as a secondary, coherent source. A conceptual arrangement is shown in Figure 12.2.12. The benefits of this arrangement are:

- a reduced requirement on the demagnification, and a resulting increase in potential working distance
- a source that is diffraction limited in both directions
- reduced sensitivity to beam motion

This path relies on the fact that a waveguide with a single mode illuminated radiates as a coherent source, and that the size of a waveguide that can carry a single mode is in the 30 to 50 nm range.

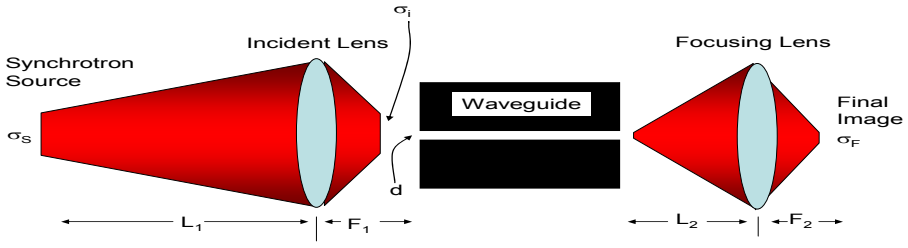

Figure 12.2.12 Schematic diagram showing the use of a waveguide in an optical system for achieving a 1 nm focal spot.

From an optics point of view, there are two disadvantages of synchrotron-based sources of radiation in comparison with visible light optics. First is the relative inaccessibility of the source. Due to heat load and radiation issues, it is difficult to adjust the source size with slits close to the source without perturbing the overall ring—and, in addition, the slits are engineering challenges. Secondly, all synchrotrons have relatively large electron beam source sizes, of the order of microns, which then also constrain the photon source size. To reach small x-ray spots requires a large demagnification factor, and leaves very little useful working distance.

Waveguides have been recognized as a possible mechanism to provide small beams. However, they have two drawbacks: waveguides need to work in the near field, and it has been difficult to couple light efficiently into the waveguide modes. Recent experiments with a direct coupling scheme as shown in Figure 12.2.12

have significantly improved the efficiency of coupling. In this scheme, the synchrotron source is demagnified by the incident lens on to the front of a waveguide with aperture *d*. The demagnification in this step,

$$\frac{L_1}{F_1}, \tag{12.2-8}$$

can be quite large with a small F_1. Since this illuminates only the waveguide, the working distance F_1 can be made as small as is necessary. As suggested in Figure 12.2.12, the incident lens focuses the source size σ_S to an image size σ_i, which is bigger than d, the width of the waveguide.

The waveguide, which only accepts a diffraction-limited fan, serves to pass the appropriate coherent fraction in the vertical, and since the source is close to diffraction limited in the vertical, most of the vertical fan can be coupled into the waveguide.

The portion of light that gets accepted by the waveguide propagates down the waveguide, with some loss due to wall roughness and wavefield overlap with the guiding materials. At the exit, the mode radiates coherently, with an effective size d, into another demagnifying lens. Since the source size is now 30 nm instead of 6 μ, the demagnification required is 30 instead of 10^4, and so one can have L2 be 3 m and F2 be 0.1 m, resulting in a significantly larger and more useful working distance than the 10 mm of a more conventional optics arrangement. Note that this would be most useful with broad bandpass optics. If one uses a square waveguide then, one can end up with a virtual source that is diffraction limited in both the vertical and horizontal.

Another advantage of this scheme is its potential stability. Given the dimensions listed above, it is possible to mount all the optics components and the sample stages on a single, vibrationally quiet table. The main disadvantage is that all the components introduce loss.

12.2.3 Basic Source Properties

12.2.3.1 Source Size, Divergence, and Estimate of Optic Size

In a 5 m, low-β straight section, NSLS-II is currently projected to have an effective vertical photon source size of 5.9 microns, a horizontal source size of 39 microns, and vertical and horizontal divergences of 12 and 18.6 μrad, respectively. We first consider a diffraction-limited optic focusing in just the vertical. The focused spot will be a convolution of the diffraction-limited spot with a demagnified image of the source; for Gaussian quantities, we can add in quadrature. Thus, to achieve a net 1 nm focus size we need √(1/2) nm from demagnification of the source, and √(1/2) nm from the diffraction-limited optic. The demagnification required is, therefore, 10^4 or better.

With the demagnification set, we now consider possible working distances (focal lengths). At 50 m, the focal length is 5 mm; at 100 m it is 10 mm. Using the beam divergence, we can estimate the size of the beam at these points and hence the size of the required optic. In the vertical, the 1σ size of the beam is 60 microns at 50 m and 120 microns at 100 m. In the horizontal, the 1σ sizes are 95 and 190 microns, respectively. As is discussed in Section 12.4, the approach to handling larger horizontal source size and divergence is to trade off flux for better a focal spot—for example, by slitting down the beam size in the horizontal.

12.2.3.2 The Smallest Spot Needs Coherent Illumination

Consider a beam from a distant source of width *a,* from which the optic subtends a full angle of ϕ (Figure 12.2.13). If the source distance, *s*, is many times the optic's focal length *f*, it will be imaged at a distance

$s' \approx f(1+f/s)$ so that the angle subtended by the optic from the image will be well approximated by the numerical aperture θ.

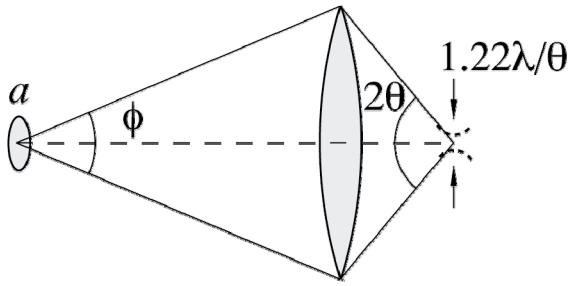

Figure 12.2.13 Illustration of the phase space area of scanned imaging, where one must restrict the product $a\phi$ to be less than λ.

By Liouville's theorem, the width of the geometrical image from this source will be b and the phase space product of the image will be $b\theta = a\phi$. We can then consider the ratio p of this spot size to that of the diffraction-limited focus, which is given by

$$p = \frac{b}{1.22\lambda/\theta} = \frac{a\phi/\theta}{1.22\lambda/\theta} = \frac{a\phi}{1.22\lambda}. \qquad (12.2\text{-}9)$$

A more detailed calculation involves convolution of the geometrical image with the diffraction-limited optic's point spread function; such a calculation for the case of incoherent brightfield imaging indicates that values of p of about 1 or less deliver nearly fully diffraction-limited image resolution (Figure 12.2.14). This leads to an important (and well-known) result: to obtain the finest possible focus spot from a lens, one requires either a spatially coherent source, or one must aperture an incoherent source to use only the spatially coherent fraction.

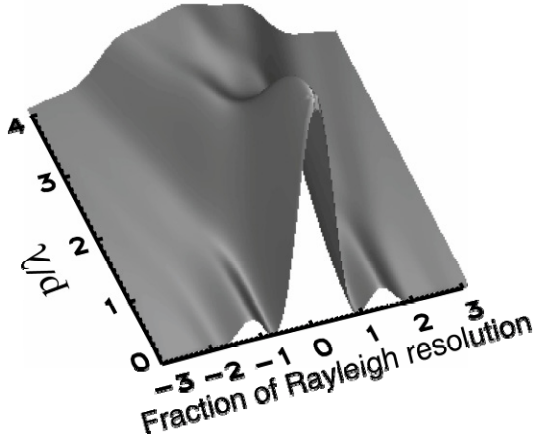

Figure 12.2.14 To achieve a perfect diffraction-limited focus in a scanned imaging system requires spatially coherent illumination; that is, the size-angle product p of the illumination must be restricted to about 1λ or less. NSLS-II will provide nearly coherent beams, making a large fraction of its flux available for achieving excellent spatial resolution in scanned imaging and microprobe experiments.

Figure: Winn et al. [12.2.14].

12.2.3.3 The Importance of Emittance

In this section, the effect of the electron beam emittance on determining the flux into a focused spot is considered. It is shown that for a diffraction-limited optic, improving the emittance of the ring increases the flux into a desired focus spot. When electron emittance is negligible, all the light goes into the focused spot.

By definition, for a diffraction-limited photon source,

$$\sigma\sigma' = \frac{\lambda}{4\pi}, \tag{12.2-10}$$

or, in terms of **f**ull **w**idth **h**alf **m**aximum, one finds $(d\times\theta)_{FWHM}\approx\lambda/2$, where d is the FWHM size of the source and 2θ is the FWHM angular divergence of the source.

For NSLS-II, the source is close to diffraction limited in the vertical, but in the horizontal the emittance is of order 1 nm. For ideal emittance preserving optics with a NA approaching 1 and a physical aperture larger than the beam, one could focus all the light into a 1 nm spot. However, optics with such perfection do not exist. In Figure 12.2.15 we consider the effect of finite emittance on the fraction of flux focused into the spot.

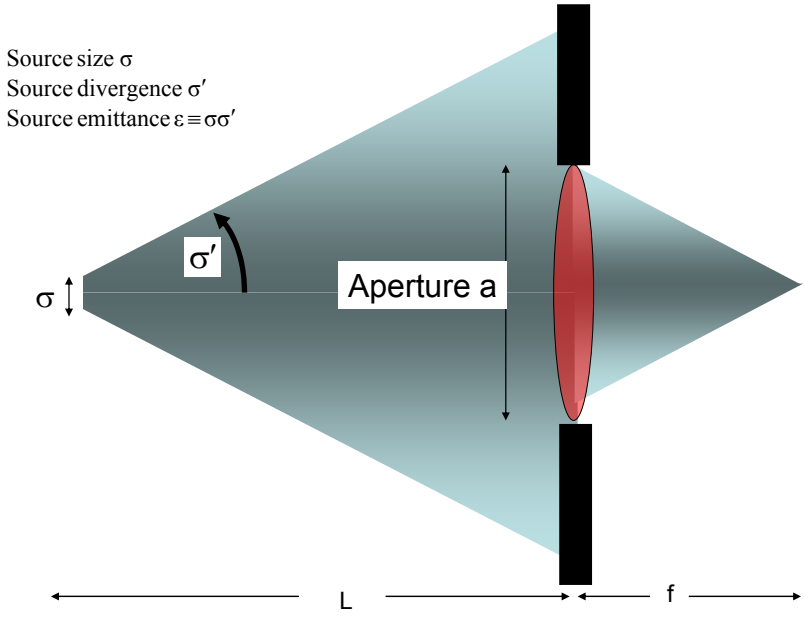

Figure 12.2.15
The requirement to coherently illuminate an optic results in reduced flux into the focused spot. The flux subtended by the optic is $\frac{a}{L}\frac{1}{\sqrt{2\pi}\sigma'_s} = \frac{a}{L}\frac{\sigma_s}{(\sqrt{2\pi})\varepsilon}$.

Then by replacing for σ_s with the constraint of coherent illumination, the fraction into the spot is $\frac{\lambda}{4\pi\varepsilon}$.

The effective emittance of the source is

$$\varepsilon = \sigma_s\sigma_s' = \sqrt{\sigma_e^{\,2} + \sigma_{ph}^{\,2}}\ \sqrt{\sigma_e'^{2} + \sigma_{ph}'^{\,2}}\ , \tag{12.2-11}$$

with σ_e representing the electron source size and σ_{ph} representing the photon source size, etc. As the electron emittance becomes vanishingly small, the source emittance simply becomes that of a diffraction-limited photon source, $\lambda/4\pi$. For NSLS-II, the electron beam is small in the vertical, but dominates in the horizontal.

To understand the role the emittance plays, consider a simple 1D model, shown in Figure 12.2.15 above, in which photons from a source of emittance, ε, are incident on an optic of size a, focal length f, at a distance L from the source, and hence with a NA of a/f. To obtain the smallest spot, d, allowed by an optic, it must be illuminated coherently, requiring

$$(d\ x\ 2\theta)_{FWHM} = (\sqrt{2\pi}\sigma_m\ x\ \frac{a}{L}) \le \frac{\lambda}{2}\ . \tag{12.2-12}$$

One can obtain a reduced source size of σ_m from the σ_s by slitting down, and this results in a reduction of the flux from the source to $(\sigma_m/\sigma_s)I_s$. Finally, if we consider the fraction of light that is incident on the optic, we find that the fraction is

$$\frac{a}{L}\frac{1}{\sqrt{2\pi}\sigma'_s}, \tag{12.2-13}$$

which compares the divergence of the source with angular size of the optic. The flux into the focused spot is then $(\sigma_m/\sigma_s)I_s(a/(L\sqrt{2\pi}\,\sigma_s')) = I_s\,(\lambda/4\pi\varepsilon)$.

The above arguments apply to the typical case of an aperture that is smaller than the full fan. For optics larger than the full radiation beam, the result is the same. In this case, the aperture size is $L\sqrt{2\pi}\sigma'_s$, from which we deduce that we need a source size

$$\sigma_m = \frac{\lambda L}{a2\sqrt{2\pi}} = \frac{\lambda L}{(L\sqrt{2\pi}\sigma')(2\sqrt{2\pi})} = \frac{\lambda}{4\pi\sigma'}, \tag{12.2-14}$$

and the fraction of flux into the focused (σ_m/σ_s), again becomes

$$\frac{\lambda}{4\pi\sigma\sigma'} = \frac{\lambda}{4\pi\varepsilon}. \tag{12.2-15}$$

In this limit, the fraction of flux into the focused spot is commonly referred to as the undulator coherent fraction.

As shown in Figure 12.2.16, the fraction of flux from the source that is focused into the spot tends to 1, as the electron emittance tends to 0, and the net (photon plus electron) emittance tends to $\lambda/4\pi$. From the figure we also see that the point of diminishing gains occurs when the electron emittance becomes less than the diffraction limit of $\lambda/4\pi$.

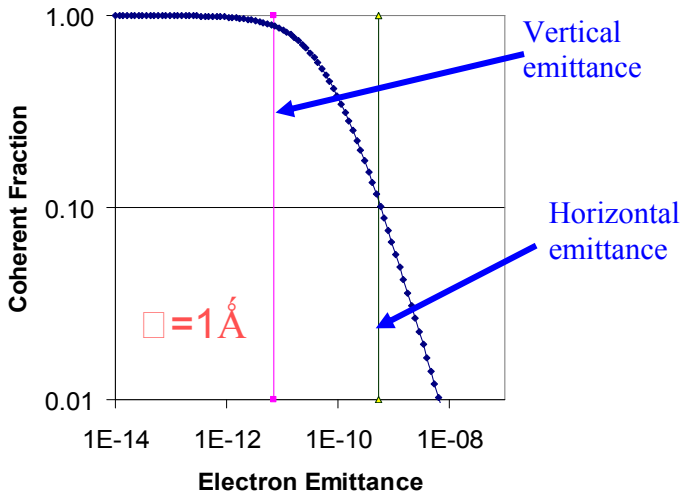

Figure 12.2.16 Effect of varying the electron beam emittance on the fraction of light delivered into a focused spot by a diffraction-limited optic for a photon energy of 12.4 keV.

These arguments indicate that if one is willing to sacrifice flux, a desired spot size can always be generated from a source of any emittance. However, improving the electron emittance allows more photons to be put into the focused spot. For NSLS-II, these considerations imply that there will have to be slits in the horizontal direction, but not in the vertical.

12.2.3.4 Incoherent Illumination is Better for Full-Field Imaging

The situation with full-field imaging is much different. Each pixel of the object acts as its own single-mode source for illuminating the objective lens, and for incoherent imaging (e.g., the generally preferred mode of transmission imaging, and fluorescence imaging systems) no optical phase correlation is desired from pixel to pixel. As a result, the challenge in full-field imaging is not one of providing the smallest possible phase space of the photon beam, but a much larger phase space. To illuminate a field of view corresponding to N pixels, one must provide N optical modes. It is for this reason that full-field imaging systems are often best suited to operation with incoherent sources such as bending magnets rather than undulators (Figure 12.2.17).

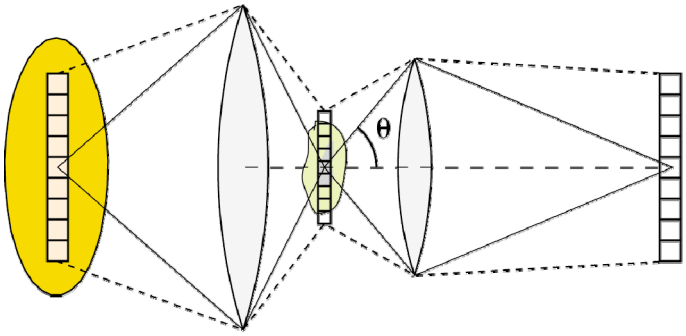

Figure 12.2.17 Illumination phase space requirements for full-field imaging. If the illumination of each pixel is to be uncorrelated with that of its neighbor (incoherent imaging), then the desired source phase space area is equal to the number of image pixels in each of two orthogonal directions.

12.2.4 Some Implications of Metrics, Source, and Optics

12.2.4.1 The Effect of Apodization on the Modular Transfer Function

Consider the case of optics that have a central obscuration, which is a fraction a of the optic diameter (such as the central stop-order sorting aperture pair required by Fresnel zone plates, as will be discussed below). A large central stop will slightly decrease the radius of the central focus while simultaneously putting a larger fraction of energy into sidelobes; this has the effect of reducing the MTF or fraction of specimen signal captured at various specimen size scales (Figure 12.2.18). Optics that allow work without central "stops" or at least with small values of a have very distinct advantages over optics with large central stops or large values of a.

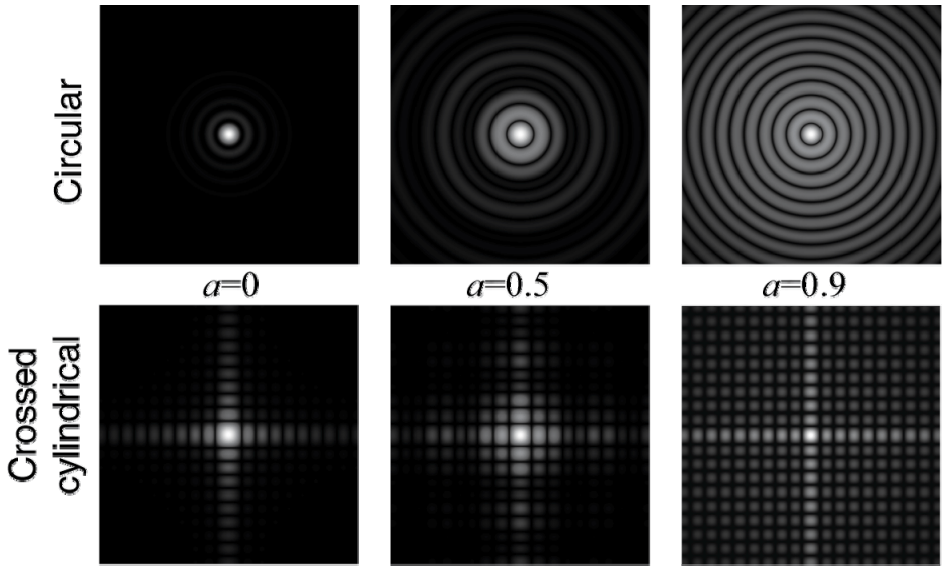

Figure 12.2.18 Point spread function for both circular and crossed cylindrical optics with various central stop fractions *a*. These images show the square root of the intensity as shades of grey, normalized to the peak value in the center. These images illustrate that it is not enough to simply achieve high numerical aperture; it is also important to have a lens with response reasonably near its center.

This is especially important when considering optical systems that use crossed cylindrical lenses to produce 2D focusing. (This is the case of MLLs and K-B mirrors, for example). In such systems, the loss of cylindrical symmetry in the optic naturally leads to a loss of cylindrical symmetry in the point spread function. When combined with a large fractional central obscuration, *a*, this can mean that the sidelobes beyond the central focus can be quite significant (Figure 12.2.18). There are likely to be experiments where users will choose a lower resolution but cylindricallysymmetric, low-*a* optic over higher resolution but crossed-orthogonal, high-*a* optics. While it may seem beneficial to narrow the central focus by increasing the diameter of a central stop, the contrast of an image (or, for example, the accurate fluorescent analysis of how much of an element is in what region of a specimen) will be degraded by the increasing presence of the sidelobes. This is especially problematic for imaging systems made up of orthogonal pairs of cylindrical lenses. As a result, circular optics with unobscured apertures will be favored for some experiments, even though a finer focus probe is available from orthogonal pairs of cylindrical optics with large central stops.

12.2.4.2 Limitations of Crossed Linear Lenses

A potentially serious limitation for the high-resolution optics of the types considered here is the use of the crossed-pair of 1 nm lenses to approximate a radially symmetric lens, and to produce a point focus. In this geometry, one focuses in one direction with one optic, and then places further downstream a lens focusing in the other direction. The leading optics candidates for high spatial resolution, Multilayer Laue Lenses and kinoforms, are each fabricated in a crossed linear geometry. For small NA, the Fresnel approximation is valid and the crossed lens is a good approximation to a radially symmetric lens. However, for large enough NA we expect the Fresnel approximation to break down, and the question is, in this new regime, are crossed lenses still a valid approach? Here we find that while there is some broadening of the central spot, the most significant effect is a reduction in contrast in the MTF, with less light in the central spot, and we therefore conclude that the crossed geometry is a reasonable, albeit not ideal, geometry.

In the Fresnel approximation, spherical secondary wavelets are replaced by wavelets with parabolic wavefronts. The starting point for such an analysis is the Fresnel-Kirchoff diffraction formula. With the usual approximation of a "thin" optic, then, following Goodman [12.2.16], the equation takes the form:

$$U(P_0) = \frac{1}{i\lambda} \iint_{(\xi,\eta)} U(P_1) \frac{\exp(ikr_{01})}{r_{01}} \cos\theta \, ds \,, \tag{12.2-16}$$

where

$$k = \frac{2\pi}{\lambda} \,, \tag{12.2-17}$$

and

$$r_{01} = \sqrt{z^2 + (x-\xi)^2 + (y-\eta)^2} \tag{12.2-18}$$

with (x, y, z) in the image plane and (ξ, η) in the "thin" object plane. One can expand r_{01} in a series, and retaining terms to the second order brings us to the Fresnel approximation for r_{01}:

$$r_{01} \approx z[(1 + \frac{1}{2}(\frac{x-\xi}{z})^2 + \frac{1}{2}(\frac{y-\eta}{z})^2] \tag{12.2-19}$$

showing the replacement of the spherical wave by a pair of orthogonal parabolic terms. Within this approximation then, the crossed linear pair of lenses are separable, and each lens focuses independently of the other. Examining higher order terms that were neglected, the limit of validity of this approximation is:

$$z^3 \geq \frac{\pi}{4\lambda}\left[(x-\xi)^2+(y-\eta)^2\right]^2 \qquad (12.2\text{-}20)$$

if we pick λ on the order of 0.1 nm and a physical aperture of 100 microns, which is a typical order of magnitude for the size of a hard x-ray focusing optic. We find that z, or the lens focal distance, is greater than or equal to 1 cm, corresponding to a diffraction-limited focused spot size of order 10 nm. In other words, for 100 micron aperture lenses, we expect a crossed lens pair to be able to focus at least down to 10 nm. However, this condition is sufficient, and is perhaps overly stringent; numerical simulations are required to clarify the true limits of the crossed pair.

Figures 12.2.19 and 12.2.20 show the results of such a simulation. Here we chose a cylindrically symmetric wave incident on an aperture. In the absence of a lens, the cylindrical wave results in a line focus at f_0 (not shown). The left panel shows that when a single cylindrical lens is placed in the aperture in a crossed geometry, the result is a 2D point focus. The same data are shown in the central and right panels. As we expect, for small NA for which the Fresnel approximation is known to hold, the sharp central component has approximately the same scaled width as a radially symmetric lens. Figure 12.2.20 shows a larger NA, on the order of 0.1. We can see that the sharp component maintains its width, but intensity shifts to the tails.

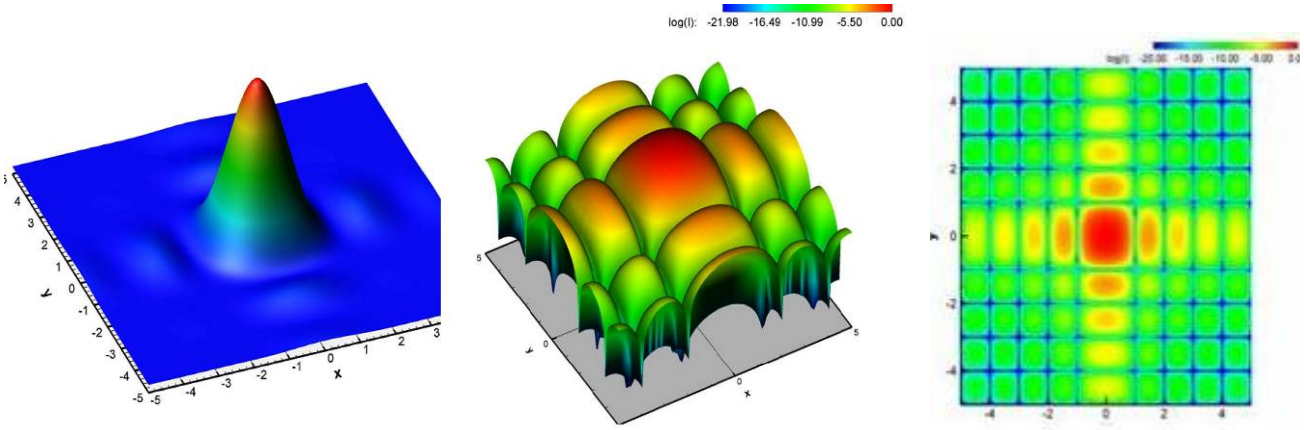

Figure 12.2.19 Results of simulations of a crossed linear lens arrangement in the limit of small NA (0.05). On the left are the data with the intensity on a linear scale showing the 2D focusing of a crossed pair. In the center we see the same data plotted in units of λ / NA with a log scale in order to highlight the subsidiary maxima; color represents intensity. The crossed geometry retains a sharp central focus, with a resolution very close to that of the radially symmetric lens. The right figure is the same data plotted as a 2D projection.

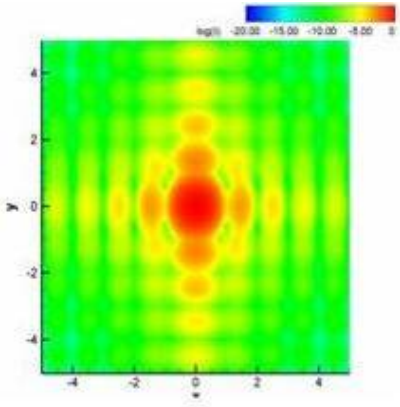

Figure 12.2.20 For NA=0.1 there is increased intensity in the tails surrounding the sharp central component. However, the sharp central component has approximately the same scaled width as the smaller NA shown in Figure 12.2.19.

12.2.5 Leading Candidate Approaches to Achieving 1 nm Resolution

Having outlined some of the fundamental issues associated with optics and achieving 1 nm spatial resolution at a synchrotron source, we now examine the leading candidates for approaches to achieve this, and the issues that are required to be solved for each. The first discussion concerns multilayer Laue lenses. Following that, kinoforms are discussed in detail.

12.2.5.1 Multilayer Laue Lenses (MLLs)

Because MLLs can be fabricated by depositing thin films on flat substrates, they offer a relatively straightforward route to high resolution x-ray focusing: in the simplest concept, one could deposit alternating atomic layers to obtain an x-ray focus with atomic dimensions. Such a simple picture, however, ignores factors such as focusing efficiency and the need to satisfy the Bragg condition.

In the discussion on planar Fresnel zone plates, we noted that the thickness of the zones along the x-ray beam direction plays a crucial role in determining the focusing efficiency of the optic (Figure 12.2.9). The aspect ratio of MLLs is even higher; while an exact calculation of the thickness can be found from considering the pendellösung phenomenon in dynamical diffraction theory, a good approximation at small numerical aperture for the desired thickness t of zones is given by

$$t = \lambda / \left(2\left[\delta_A - \delta_B\right]\right), \tag{12.2-21}$$

which works out to be about 5 μm for Mo as material A and Si as material B, at 10 keV. If the Bragg condition is also satisfied, a diffraction efficiency well above the theoretical limit of 40.1% for "thin" phase gratings can then be achieved. However, satisfying the Bragg condition introduces a new set of complications, shown in Figure 12.2.21.

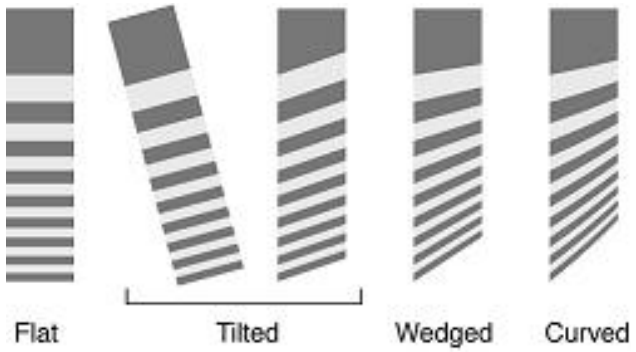

Figure 12.2.21 Types of MLL arrangements: flat, tilted, wedged, and curved. Tilted zones can be achieved either by tilting a straight cut from the substrate, or by cutting along the tilt angle.

If a simple perpendicular cut through a thin film stack is mounted perpendicular to the x-ray beam, each diffracting plane will be off-Bragg relative to the desired diffraction direction and the optic will have very low diffraction efficiency for all but the innermost zones (the "flat" case of Figure 12.2.21). If instead we tilt the perpendicular cut, or make a cut through the layer stack at a slight angle, this satisfies the Bragg condition for a particular set of zones only; this is called the "tilted" case in Figure 12.2.21. A better solution is to arrange for the zones at each radius to be at the proper tilt angle for satisfying the Bragg condition; this is called the "wedge" case in Figure 12.2.21. However, if the thickness of the optic exceeds the depth of focus [which is $\Delta_l = 2.7\Delta_t\left(\Delta_t / \lambda\right)$, giving $2\Delta_l$=54 nm for Δ_t=1 nm transverse resolution at λ=0.1 nm wavelength], then one must change the Bragg angle in depth through the optic, giving rise to the "curved" case of Figure 12.2.21. If such a curved-zone MLL could be fabricated, Schroer [12.2.17] has shown that it could, in principle, deliver a 1 nm resolution focus. The more realistic scenario involves making choices between tilted and wedged MLLs. As discussed further in Section 12.2.5.1.2, to go from 10 nm to 2 nm spatial resolution, it is essential to

develop approaches to fabricating wedged MLL zones. Unpublished calculations from Schroer's group show that this result holds down to 1 nm.

12.2.5.1.1 Characteristics of a Multilayer Laue Lenses

What are the characteristics of a multilayer Laue lens for 2D focusing? The optic would consist of four half-linear focusing components; at 10 nm resolution, each of these four components could be a tilted half-diameter linear focusing optic. The tilt would have to be set to the right value to meet the Bragg condition for the desired x-ray wavelength. Next, two such opposing optics would need to be aligned with respect to each other in translation and azimuthal rotation at nanometer precision so that their two line foci would completely overlap; the x-ray interference scheme shown in Figure 12.2.22 could be used to accomplish this, and then a laser interferometer could be used in a feedback loop to dynamically adjust the piezos to maintain alignment against thermal drifts. The orthogonal optic pair would then be aligned separately, and the two optics pairs would be combined to produce a crossed linear focus.

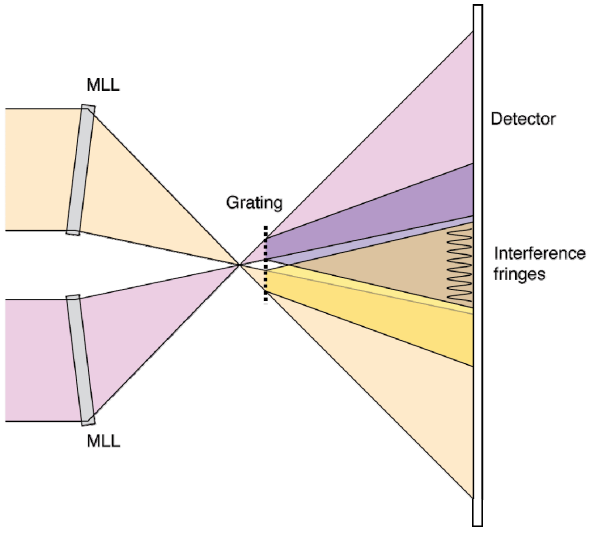

Figure 12.2.22 Possible alignment scheme for pairs of half-linear-focusing multilayer Laue lenses. A grating downstream of the focus could be used to cause the wavefield from each optic to interfere at a detector plane, and provide a diagnostic on the relative alignment of the two half-optics.

Such an optic might be used for tuning over a modest energy range, such as required for recording a XANES spectrum from the focal point. However, when tuning over a larger energy range, it would likely be necessary to readjust the tilt of each MLL, and then redo the translation and azimuthal orientation alignment. Note that because the optics would be tilted to be on-Bragg for a single incident beam direction, it is likely that they would have a very limited field of view when used as imaging rather than probe-forming optics.

12.2.5.1.2 Challenges Associated with Reaching 1 nm Resolution with Multilayer Laue Lenses

A number of significant challenges exist when contemplating extension of the MLL approach from values of ~10 nm toward the NSLS-II goal of 1 nm resolution focusing. Consider the case of a λ=0.1 nm optic with a focal length of only 1 mm (which is about as short as imaginable for practical experiments), the values of zone number n, distance of the zone from the optical axis r_n, zone width Δ_{rn}, and corresponding Rayleigh resolution are shown in Table 12.2.1.

Table 12.2.1 Resolution Dependence of MLL Optics Parameters.

Rayleigh resolution (nm)	Zone width Δ_{rn} (nm)	Zone number *n*	Distance of zone from optical axis r_n (μm)
10.0	8.2	370	6.1
5.0	4.1	1490	12.2
2.5	2.1	5,960	24.4
1.2	1.0	26,000	51.0
1.0	0.8	37,210	61.0

As the table shows, such an optic involves very thin zones throughout nearly its entire area. In fact, simply by going from a resolution of 5 nm to a resolution of 1 nm, one needs to go from 1,490 zones to 37,210 zones; the challenges in fabrication of the optic increase steeply with relatively small changes in the resolution goal. In fact, current examples of MLLs have all had less than 1,000 zones. (Note also that the monochromator resolving power, E/ΔE, should be comparable to the number of zones divided by 2 to achieve the desired spatial resolution.)

In addition, as discussed above, as the resolution is reduced below 10 nm, it will be necessary to move from tilted to wedged zones to keep all zones close enough to the Bragg condition to deliver uniform efficiency. (Further, if one does not meet the Bragg condition or have the proper thickness for each range of zone widths, both the amplitude and phase of the local exit wave from the optic will be degraded, which in turn will degrade the line spread focus profile of the optic.) An example of the need to move from tilted to wedged zones is shown in Figure 12.2.23; at 2.4 nm Rayleigh resolution corresponding to 2 nm zone width, only a narrow range of zones will be on-Bragg unless one can fabricate the MLL with wedged zones. Another way of illustrating the same conclusion is provided in Figure 12.2.24, which shows the calculated efficiency and Rayleigh-like resolution for flat, tilted, and wedged MLLs with various zone widths.

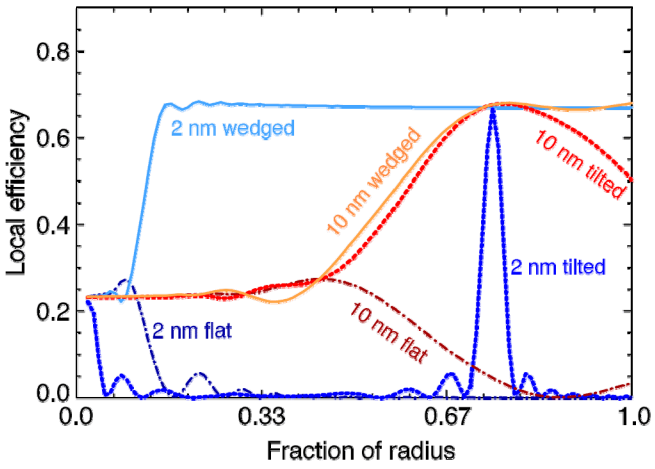

Figure 12.2.23 Local diffraction efficiency of zones at various radii as calculated for a Mo/Si MLL operating at 10 keV. For an outermost zone width of 10 nm, the simple tilted zone case gives high diffraction efficiency for a wide range of zone widths, although the 10 nm wedged case is superior. For an outermost zone width of 2 nm, the tilted zone case works only for a narrow range of zones which properly satisfy the Bragg condition; it becomes essential to fabricate wedged zones to achieve high focusing efficiency across the optic, to obtain a high-quality focus.

Figure adapted from Kang et al. [12.9].

The calculation for Figure 12.2.24 involves an estimate of the local diffraction efficiency from zones used as simple gratings to diffract light into a desired far-field diffraction order. In fact, this calculation is incomplete, in that since the optic thickness exceeds the depth of focus $2\Delta_l$, or about 54 nm for a 1 nm Rayleigh resolution optic at λ=0.1 nm, it will be necessary to move from wedged to curved zones because the Bragg condition will change through the depth of the MLL. The good news is that recent simulations by Schroer have indicated that curved-zone MLLs can, in principle, achieve a 1 nm resolution focus; however, no realistic scheme has yet been put forward for practical fabrication of curved 1 nm zones.

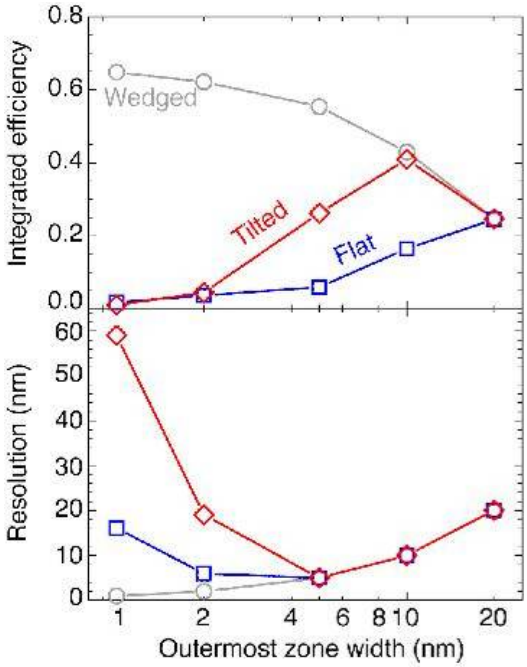

Figure 12.2.24 Calculated efficiency and Rayleigh-like resolution for MLLs with various values of outermost zone width for the flat, tilted, and wedged zone cases. As can be seen, a 5 nm resolution target with flat MLLs appears to be achievable at reduced efficiency. Better efficiency is attained if tilted zones are used. And if wedged zones are used, better efficiency and resolution are attainable.

The discussion thus far has assumed that layers of the proper thickness can be deposited with perfect thickness control, without thickness error or roughness accumulation, and with no interlayer diffusion. In recent years the EUV lithography program has been a huge driver in improving the quality of synthetic multilayer mirrors, and multilayer coatings as thick as 70 μm have been fabricated with roughness below 5 nm by a process of sputtering, interleaved with ion beam polishing. However, the fact that normal incidence reflectivity for sputtered multilayer mirrors continues to be poor at wavelengths below about 5 nm means that interlayer diffusion is likely limiting the performance of sputtered layers on dimensions of 1–2 nm, which is right at the ultimate resolution goal of the NSLS-II project. One possible solution to this problem is to use Molecular Beam Epitaxy rather than sputtering to fabricate the alternating zone layers, and preliminary calculations show that there are no significant focusing errors associated with forcing zone boundaries to line up with integer multiples of MBE monolayer thicknesses. In addition, while a key appeal of MLLs is the ability to start at the outermost zones so that error accumulation is zero when the zone width is the smallest, a glance at the table of zone widths and numbers in Table 12.2.1 reveals that for very high-resolution optics there is still ample opportunity for small fractional thickness variations to accumulate, leading to dephasing of zone positions from their proper values, which, in turn, will produce aberrations in the focus, or the choice of very large central stop fractions *a* that will provide a narrow focal spot at the cost of needing to tolerate very strong sidelobes.

12.2.5.1.3 Simulations for MLLs

For the leading candidate MLL optic, the push to a resolution of 1 nm raises a number of new questions. Any physical implementation of a MLL will deviate from the idealized structure, and it is important to understand if these imperfections would prevent the achievement of 1 nm resolution. In order to resolve these issues, or at least gain some physical intuition, some simulations have been performed. The optics imperfections addressed by these simulations are the 1) discreteness of the underlying material, 2) density contrast difference between the constituent layers, 3) interfacial roughness, 4) growth rate errors, and 5) apodization or elimination of the central portion of the optic. Briefly, these simulations suggest that many of these deviations from the ideal case do not prevent one from obtaining 1 nm resolution. Rather, most of the imperfections result in a reduction in intensity of the central high resolution feature but maintain the same width, with a concomitant growth of "tails" to the focused spot; in other words these imperfections lead to a

reduction of efficiency of the optic. However, one imperfection is quite disruptive to the high-esolution feature. If the growth rate for the constituent deviates significantly from the desired growth rate, the result is zones that are not placed at the idealized locations, leading to phase errors that destroy the focusing properties.

These results are consistent with existing intuition developed for standard binary zone plates; however, without these simulations it was not clear a priori that the extreme nature of these optics would not require different intuition. For example, for the most serious error, that of the growth rate, the standard intuition is that zones need to be placed to within an accuracy of one-third of the width of the zone in order to preserve the required phase accuracy. The other errors, such as randomization of boundary locations due to a discrete lattice or interface roughness, preserve the overall phase accuracy and hence preserve the optic resolution, albeit with some reduction of intensity. Note that there are limits to the simulations performed, because they are performed in the "thin" lens limit, which effectively compresses the optic into a single plane. We expect that this work will need to be reproduced in the "thick lens" limit to strengthen the conclusions.

Discrete Lattice Implementation

One potential physical implementation of a MLL is to grow these optics in a lattice-matched materials system. The single crystal nature of this implementation would have potentially significant advantages. First, the interfaces can be made atomically flat, as has been demonstrated [12.2.18]. Second, the single-crystal nature will result in reduced small-angle scattering. Third, these films can be made thinner as a result of the reduced roughness.

These advantages come at a price. The boundaries of transition between the different zones are fixed multiples of the materials chosen. For example if one chooses BaBiO3 and MgO as the materials pair from which to construct the MLL, the C-axis lattice parameters are 0.43 nm and 0.42 nm respectively, and so the thickness of any given zone can only be discrete multiples of these basic lattice units. However, the ideal zone plate functional form is $u_n = \sqrt{(n\lambda f + 0.25n^2\lambda^2)}$ and cannot be placed onto such a discrete lattice, leading inevitably to errors in the placement of the zone boundary placement. Numerically, the best choice v_n that approximates u_n using the underlying discrete lattice is chosen, and the simulation of the resulting profile is performed. What the simulations show is that in spite of the discretization of the zone profile, the width of the focused spot is not significantly different from an equivalent zone plate with the ideal zone profile. However, the intensity in the central component is reduced relative to the intensity in the tails.

Density Contrast Difference

The results obtained by varying the ratio of density contrast between the two layer compounds fit neatly with established intuition. The focus intensity is simply proportional to the contrast difference between the layers, with no effect on the optic resolution.

Interface Roughness

Here the results obtained by simulation are also consistent with naïve expectations. As long as the roughness is much smaller than the smallest zone width, the resolution of the optic is unchanged, though the intensity of the focus decreases with increasing roughness. The location of the diffuse scattering depends on the specific form of the roughness. For the Gaussian roughness chosen here, the unfocussed light goes into a uniform background. A conformal roughness will give a different distribution of the unfocused light. The numerical aperture of the optic will be limited to a size such that the smallest zone becomes comparable to the roughness. The net effect is that the numerical aperture is determined by the point at which the roughness becomes comparable to a zone width.

Growth Rate Errors

Growth rate errors are the most significant obstacle to the production of high resolution MLL optics. The reason is that growth rate errors can result in the center of mass being placed in a different location from its ideal location. This kind of error is in marked contrast with the other imperfections, which have the zone center of mass ideally placed, but with some randomness in the specific boundary location. This sort of error results in phase errors, and the simulations show that small errors can result in significant broadening of the focus.

Apodization

Existing examples of MLL optics are apodized, i.e., regions of the optics are blocked (effectively, there is a central stop). Our simulations show that increasing the central stop zone results in increased tails, but still maintains a sharp, high-resolution central feature. Figure 12.2.25 shows examples of simulations of five different sizes of central stops.

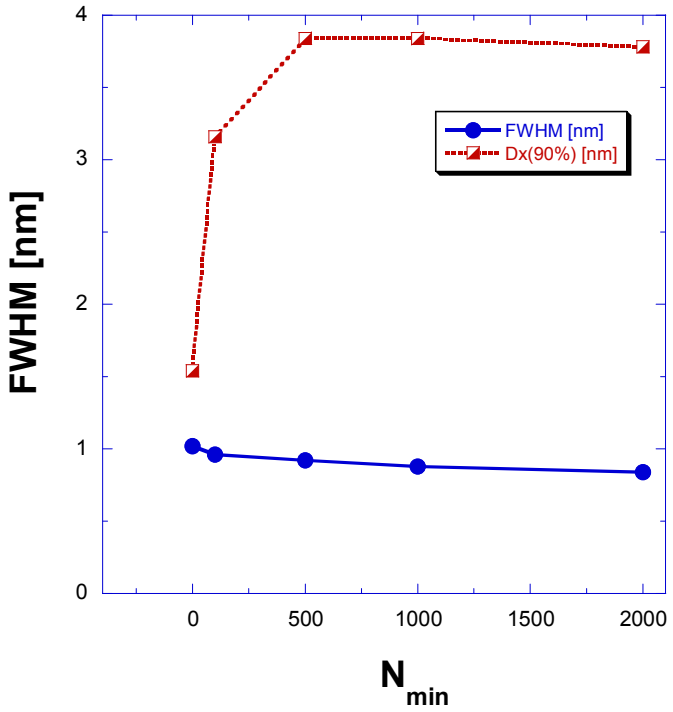

Figure 12.2.25 The blue curve shows the width of the central feature, extracted from the full width at half maximum (FWHM). The red squares and line include effects of the width of the tails or broad feature, determined by extracting the width containing 90% of the integrated intensity. The bottom axis is the size of the obstructed region measured by the number of zones. The full size of the zone plate is 20,000 zones.

Not shown in the figure is a reduced intensity of the central component with increased apodization. Clearly, while apodization results in increased intensity in the tails, the central FWHM is relatively unchanged. Consequently, apodization is not an obstacle to 1 nm resolution optics, but will result in a reduced sensitivity to high spatial frequencies.

Even with these potential limitations, MLLs offer one of the most promising paths toward focusing resolution on the nanometer scale. However, it is also likely that MLLs will not be the optic of choice for all experiments, as in some cases it may be preferable to use cylindrically symmetric optics with small central stop fractions *a* to minimize the energy distributed outside the central focus; in other cases, the achromatic nature of reflective optics may be preferred.

While Fresnel zone plates rely on the difference in optical properties between one material and vacuum, MLLs rely on the difference in optical properties between two different materials (typically with different densities and atomic numbers). Because the ratio of phase shift to absorption improves roughly as the square of increases in photon energy, this means that MLLs are not suitable for use at energies below a few keV. (The same argument apples to refractive lenses and kinoforms, as well.) As NSLS-II will be a powerful

source of coherent soft x-rays, it will be important to have available high-resolution Fresnel zone plates for soft x-ray focusing experiments at NSLS-II.

One final consideration involves thermal loading of the optic. Thermal engineering studies are required to set a limit on distortion of a MLL due to absorption of some fraction of the x-ray beam. Paradoxically, this is more of a problem at low photon energies than at high, because of the improvement of the ratio of f_1/f_2 at higher energies, so that a MLL becomes more and more of a pure phase optic.

In Figure 12.2.26, layer positions were measured using a standard Scanning Electron Microscope. While standard SEMs do well at measuring the size of small features within the field of view, current systems tend not to have very accurate absolute position measurement capabilities. For example, while one can observe that zones at the 10 μm layer position have a width of about 5 nm, one cannot determine that the boundary of zone 487 is at the required position of 10.0034 μm. Absolute zone placement errors must be kept to below about a third of a zone width (or 0.3 nm, which is the size of an atom) to meet the 1 nm resolution goal of NSLS-II.

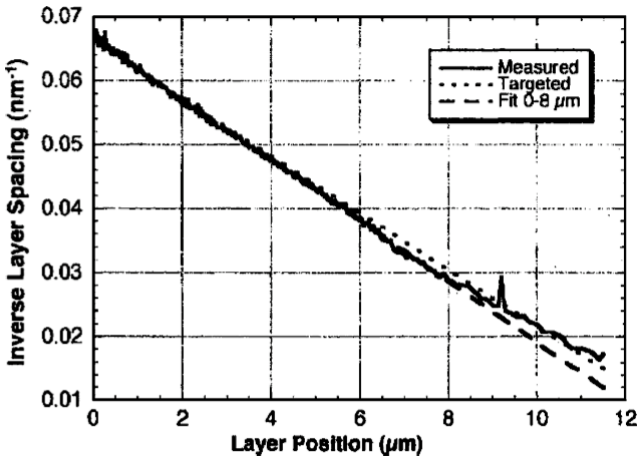

Figure 12.2.26 Example of present-day diagnostics used to evaluate zone placement accuracy in MLLs [12.2.21].

12.2.5.1.4 Effort Required to Reach 1 nm Resolution with Multilayer Laue Lenses

MLLs were first developed at Argonne National Laboratory, where there is an ongoing program to develop MLLs based on DC magnetron sputtering for layer deposition. We propose to complement the effort at Argonne, while keeping in contact with their efforts, in the following ways:

- BNL has unique capabilities in ultra precise layer deposition using Molecular Beam Epitaxy. With MBE, one can deposit material layers with a thickness that is controlled down to an integer number of crystallographic unit cells, offering the potential for improvement in the minimum zone width that one can really achieve without the compromising effects of interlayer diffusion, and also improved layer smoothness, which in turn can make zones stay in phase by being in the proper absolute position over a larger distance. We propose to embark on a program of MLL fabrication using BNL's existing MBE system to test the ability to produce MLLs with only a modest number of layer pairs (limited by the slow rate of deposition of MBE layers) but with high focusing efficiency. We will also examine the effects of producing layer boundaries at integer multiples of crystallographic unit cells, and compare the artifacts caused by this with numerical simulations that we are currently working on.
- We propose to explore new high-density/low-density materials pairs beyond those demonstrated by Argonne to check theory against calculation and to see if there are additional favorable materials pairs that should be considered.
- We propose to develop an MBE system with more rapid layer deposition.
- We propose to explore ways to fabricate wedged layers, such as by partial masking of the substrate during part of each deposition cycle.

- We propose to acquire or develop a system able to measure zone locations on an absolute position scale, rather than relying on a standard SEM. A good candidate for this is a scanning tunneling microscope with laser-interferometer scan axis control and in-situ electron diffraction.
- We propose to develop a system for mounting and aligning four MLLs to 1 nm tolerance using x-ray interferometry, and preserving their alignment using laser interferometer feedback on the MLL support mounts.

This effort will involve people with expertise in the fields of thick-film deposition, sectioning, numerical simulations, and engineering. It will be one of the major components of the NSLS-II R&D program and will explicitly complement and extend the related efforts at Argonne National Laboratory. We expect that the newly established group at BNL will keep in frequent contact with the Argonne effort.

12.2.5.2 Kinoforms

12.2.5.2.1 Introduction

Kinoforms [12.2.19] are computer-generated phase optics that, when illuminated, generate an image of a mathematically desired final object. It is possible to form a lens kinoform where the desired object is a single point and the incident illumination is a parallel plane wave; it is also possible to create kinoforms with other desired optical functions. Kinoforms (Figure 12.2.27) can be considered equivalently from two points of view; either as an array of coherently interfering lens-segments or as an optimally blazed zone plate.

.

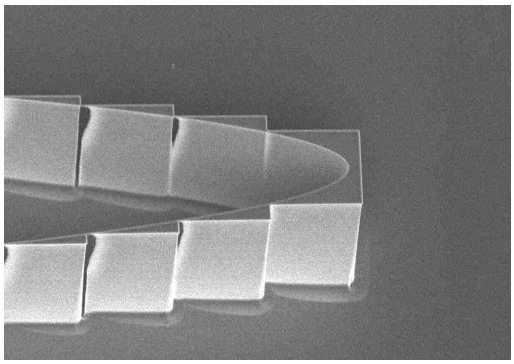

Figure 12.2.27 Kinoform structure etched into silicon with deep reactive ion etching. The step-like structure shows the material that is removed to give 2π phase shifts and is 30 microns for the designed energy of this lens. X-rays incident from the right will be focused to a line focus on the left.

Typical materials parameters of refractive lenses for hard x-rays result in an effective aperture that is limited by absorption in the thicker parts of the lens. The consequence of the absorption is that the numerical aperture, and hence the resolution, is limited. Kinoform lenses provide a route around this limitation. Shown in Figure 12.2.28 is a refractive lens and two kinoform lens equivalents of the refractive lens. For the refractive lens the mathematical derivation of the lens profile is straightforward. Given a refractive index δ, a focal length F, and a parallel beam illuminating the lens, the analog profile for a loss-less lens is

$$y^2+(2\delta-\delta^2)x^2-2\delta Fx=0\,, \qquad (12.2\text{-}22)$$

in other words, an ellipse. To obtain the kinoform structure, a volume of material is removed in integer multiples of λ/δ, where λ is the desired operating wavelength. There are two limiting kinoform structures, the "long" structure shown in Figure 12.2.28b, and the "short" structure shown in Figure 12.2.28c. The long structure is quite clearly related to the refractive lens, and the short structure has strong analogies to the standard zone plate. Both kinoform structures have a reduced absorption in comparison with the solid refractive structure shown in Figure 12.2.28a.

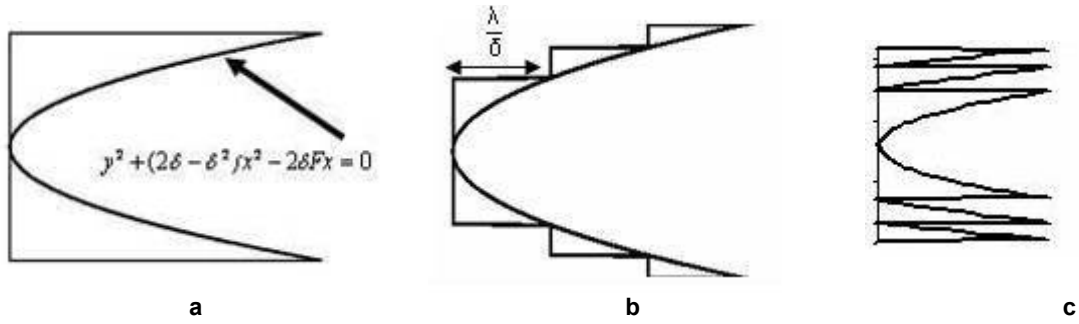

Figure 12.2.28 **a)** A solid refractive lens. **b)** Elliptical profile of "long" kinoform lens, and the sections removed from the solid refractive lens shown in **a** to reduce loss. A parallel beam comes from the left and the focused spot is on the right. **c)** A "short" kinoform lens, where the segments are folded into one plane; this is the more familiar kinoform structure, and the similarity to the binary zone plate is clear.

Shown in Figure 12.2.29 is a comparison of the absorption as a function of distance from the optic axis. On the left is the absorption of a solid refractive lens, and on the right is the same plot for the kinoform. The average transmission of the kinoform asymptotically approaches

$$T = e^{-\left(\frac{2\pi\beta}{\delta}\right)}, \qquad (12.2\text{-}23)$$

but the crucial difference is that the absorption is almost uniform across the lens aperture, and hence absorption no longer limits the NA and resolution of the lens. At 10 keV, for silicon T is 0.88, and for diamond T is 0.9937.

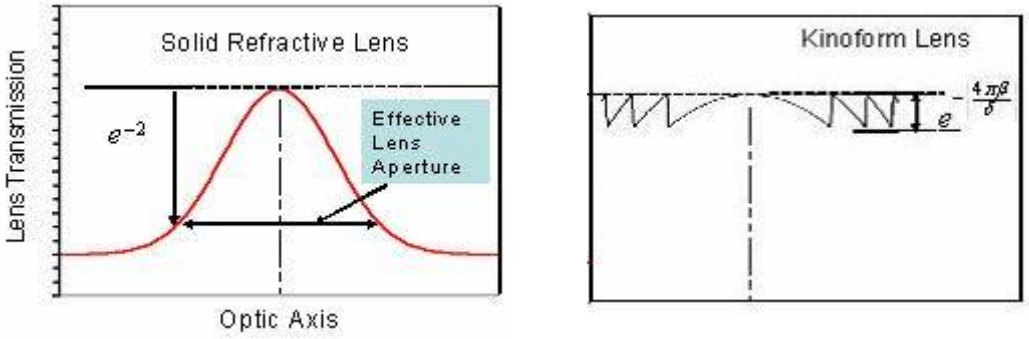

Figure 12.2.29 Comparison of the absorption across the aperture of a lens for a refractive lens on the left, and a kinoform lens on the right.

12.2.5.2.2 Analogy to the Zone Plate

While we obtained the kinoform structure by removing material of size integer multiples of λ / δ from a solid refractive lens, the resulting structure has strong analogies to a zone plate. Here we clarify the analogy to the zone plate, and then later we build on this to obtain some analytic results that have practical implications. y_m are the locations of the standard zone plate boundaries of a zone plate at x=0 for a focal length F and wavelength λ, where

$$y(0)_m = \sqrt{2mf\lambda + m^2\lambda^2}, \qquad (12.2\text{-}24)$$

as shown in Figure 12.2.30. If one evaluates the kinoform boundaries at x=$\frac{\lambda}{\delta}$, one finds that

$$y(\frac{\lambda}{\delta})_m = \sqrt{(2mf\lambda + \lambda^2(m^2 - (\frac{2m}{\delta}))} \ . \tag{12.2-25}$$

The first observation is that the boundaries $y(\lambda/\delta)_m$ correspond to the classic zone plate but with $F \rightarrow (F - (\lambda/\delta))$.

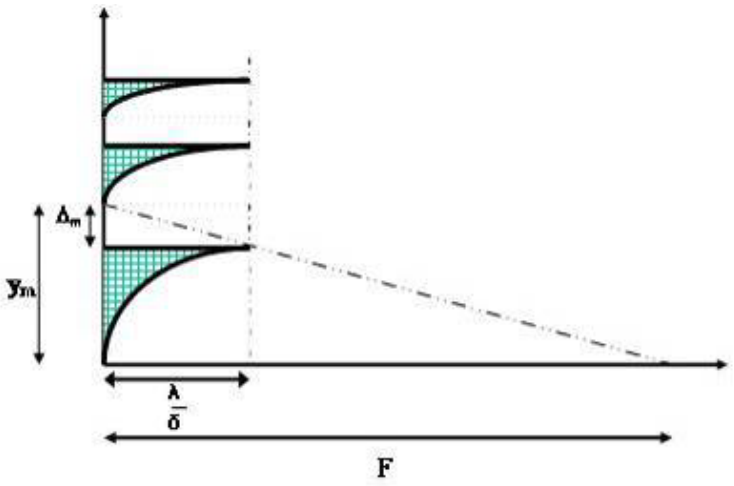

Figure 12.2.30 Connection between the kinoform and the zone plate. Evaluating the locations of the boundaries from the refractive point of view matches the zone plate boundaries if the limit δ is large.

Also, as δ tends to infinity, the thickness of the kinoform lens tends to zero, and the boundaries tend to the classic zone plate boundaries:

$$y(0)_m = \sqrt{2mf\lambda + m^2\lambda^2} \ . \tag{12.2-26}$$

This is consistent with the observation by Sweatt [12.2.22] that a thin holographic optical element can be considered as a "degenerate" lens, where the index of refraction approaches infinity, and curvatures and thicknesses approach zero for a fixed focal length.

12.2.5.2.3 The Kinoform as an Efficient Zone Plate

An ideal phase zone plate with no absorption can have ~40.4% of the light in the primary focus, and the higher order foci will have intensities

$$\frac{0.404}{n^2}, \tag{12.2-27}$$

where n is the index of the focus. In contrast, an ideal kinoform structure with no absorption operating at the primary or fundamental n=1 focus can have 100% efficiency. The reason for this difference is that for the binary zone plate, there is intensity in the higher order foci, whereas for the kinoform there is only one focus. As is shown later, the binary zone plate phase profile is a square wave profile within each Fresnel zone, which upon Fourier transforming allows the odd (±1, ±3, ±5,) harmonics to exist. In contrast, for the kinoform (which has a smoothly varying profile within each Fresnel zone), one can tailor the profile to have zeros at all

the alternate foci, resulting in all the light going into the fundamental, and giving a more efficient optic. We summarize the case for the kinoform graphically in the three panels of Figure 12.2.31.

In panel a, we show all the potential foci F/n that would result from a Fourier transform of the Fresnel zone structure of a lens. In the middle panel we show the "form factor" that is the result of the Fourier transform of the kinoform phase profile that repeats within each zone. The key feature of this panel is that the kinoform form factor has zeros at all the potential foci, except the one the kinoform phase profile is designed to maximize. In panel **c**, the bottom panel, is shown the product of the two terms, showing the only surviving focus, resulting in an efficiency of 100% for loss-less ($\beta = 0$) lens material. For real materials, β is not zero, and the net efficiency becomes

$$e^{-\left(\frac{2\pi\beta}{\delta}\right)}, \qquad (12.2\text{-}28)$$

as indicated above.

Figure 12.2.31 Normalized focal length.

a) All the allowed foci at 1/n in normalized units.

b) Form factor with zeros at most of these allowed foci.

c) The product, leaving a single focus.

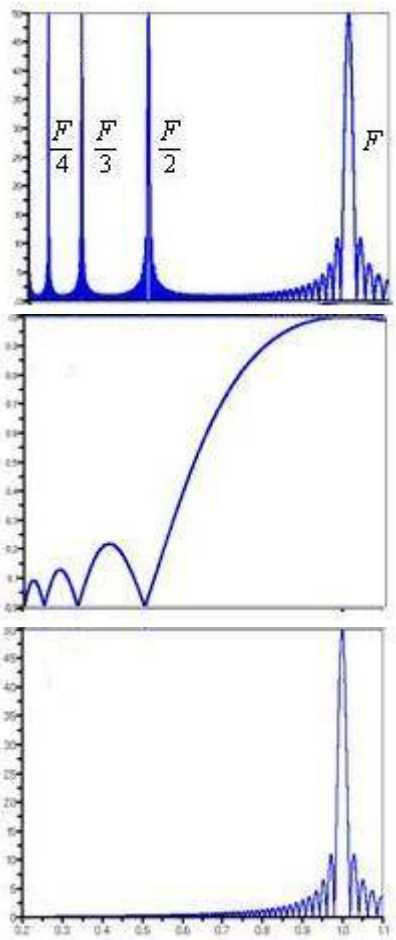

12.2.5.2.4 Higher Order Foci Enabled by the Efficient Kinoform

We briefly summarize here the analytic basis for the results illustrated in Figure 12.2.31, and extend it slightly, to show how to optimize not just the fundamental n=1 focus, but any focus of choice. This has an important practical implication. For the standard binary phase zone plate, the optic resolution is on the order of the size of the smallest zone. Most fabrication methods have a minimum feature size that can be fabricated with precision. One way to improve the resolution is to operate the zone plate at one of the higher order foci,

since the optic resolution or spot size of the nth order focus is 1/n times the size of the smallest zone. However, as we know from above, this comes at a substantial flux penalty: the n^{th} order focus has $1/n^2$ the intensity of the fundamental. The kinoform, by steering all the light into the chosen focus, allows us to efficiently operate with a resolution that can be significantly smaller than the smallest feature size in the lens. This is not un-physical; a classical optical lens is much bigger than the lens resolution.

To understand this analytically, we assume we have an optic with focal point *f* and aperture consisting of Fresnel zones with boundaries at

$$\sqrt{n2\lambda f}\ , \tag{12.2-29}$$

up to a maximum of N, i.e., a fixed maximum radius of

$$\sqrt{N2\lambda f}\ . \tag{12.2-30}$$

We will consider an optic consisting of kinoform or binary zone plate structures that are periodic in M multiples of Fresnel zones, and so the smallest feature is approximately M times larger than the smallest Fresnel zone. The new zone boundaries will be at

$$\sqrt{nM2\lambda f}\ , \tag{12.2-31}$$

where the dummy index n will run up to N/M, i.e.,the optic aperture stays fixed. In the paraxial limit, the phase shift required by the kinoform leads to a structure thickness

$$t(\rho) = \frac{\rho^2}{2\delta f} - nM\frac{\lambda}{\delta} \tag{12.2-32}$$

in the nth zone, where ρ is the radial distance from the optic axis. Using the Kirchoff Fresnel integral to find the amplitude A, at point z along the axis it can be shown that:

$$A(z) \propto \sum_n \frac{\left[e^{i\pi\alpha v}\right]_{v_n}^{v_{n+1}}}{i\pi\alpha} = \left\{\frac{2\sin(\pi\alpha M\lambda f)}{\pi\alpha}\right\}\left\{\sum_n e^{(i\pi\alpha M 2\lambda f)n}\right\}, \tag{12.2-33}$$

where

$$\alpha \equiv \frac{1}{\lambda}\left(\frac{1}{f} - \frac{1}{z}\right), \tag{12.2-34}$$

and v is ρ^2. One can consider the product of two terms as a "form factor"

$$\left\{\frac{2\sin(\pi\alpha M\lambda f)}{\pi\alpha}\right\} \tag{12.2-35}$$

and an array of "Bragg peaks"

$$\left\{\sum_n e^{(i\pi\alpha M 2\lambda f)n}\right\} \tag{12.2-36}$$

in the terminology of diffraction from crystalline arrays. In this case the Bragg peaks occur at the allowed foci. For M=1, the largest focal length is f, and the higher orders are f/n, with n = (± 1,± 2,± 3,…). For M=2 the largest focal length is 2f and the allowed foci are 2f/n; for M=3 the allowed foci are 3f/n, and so on. This makes physical sense; because we use zones of size M times the fundamental, the lowest order focal length is Mf.

However, the form factor term has zeros at all z = Mf/n with n = (±1,±2,±3,…), except for z = f, when, since in the limit α→o, we have

$$\lim_{\alpha \to 0} \frac{\sin(\beta\alpha)}{\alpha} = \beta\,, \tag{12.2-37}$$

which is nonzero. This focus at z = f, then, has nonzero intensity, and all the other foci have zero intensity. We have demonstrated in previous publications experimentally, and here analytically, that one can design kinoform hard x-ray optics to optimize the intensity of a higher order focal point. This is done to fabricate optics with resolution exceeding that allowed by the minimum size of a given fabrication method. Very few fabrication techniques and materials can give us the precision needed to fabricate the optical quality, nm-sized structures necessary to produce nm-sized beams. By using kinoforms in higher order, we anticipate an easier path for fabricating optics that can produce such focused beams.

12.2.5.2.5 Compound Kinoforms

A single kinoform lens has an aperture that is not limited by absorption. However, for hard x-ray photons, with the kinoform lens material refractive index <1, the optic resolution is limited by the critical angle, because of the required lens profile. Using Fermat's theorem, for a source infinitely far from a lens that is then focused to a point, the correct phase profile can be shown be an elliptical kinoform shape. Other source-to-lens and source-to-object distances will require other lens profiles that also can be deduced from Fermat's theorem. The elliptical shape immediately leads to the result that for a single lens there is a resolution limit ≈ λ/θ_c , because for a given focal length F, there is a maximum lens aperture = $F\theta_c$. For a single silicon lens at 11.3 keV, $0.61\lambda/\theta_c$ ~25 nm. The solution to this resolution limitation is to consider compound lenses, just as is done in conventional optical microscopy, and as shown in Figure 12.2.32. A single lens has a NA of θ_c, but an array of M lenses can have NA of $M\theta_c$. In fact, compound kinoform lenses have already been fabricated; however, these lens arrays consisted of identical parabolic kinoform lenses, and the resulting phase profile did not achieve the optimal performance. What is required is to create an array of kinoform lenses where each is designed to match the waveform from the lens prior to it to a new focus (i.e., from a virtual focus f_1 to a new focus f_2).

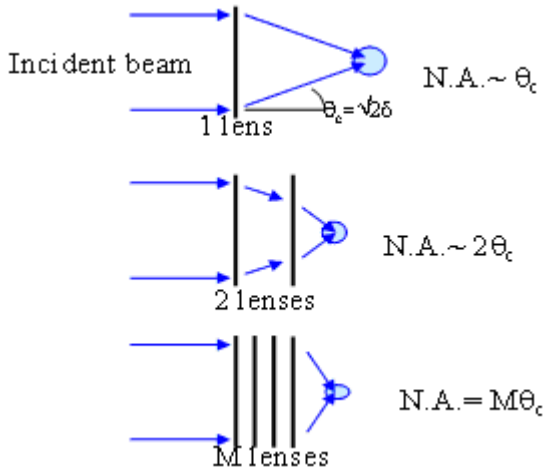

Figure 12.2.32 Using compound lenses to exceed the critical angle limit. A single lens has a maximum NA of θ_c, but M lenses can be arranged to have an NA of $M\theta_c$, resulting in a resolution of $0.61\lambda/M\theta_c$ for the array of lenses.

We have demonstrated a compound lens of this type. Shown in Figure 12.2.33 are results from a compound kinoform of four lenses, with a designed maximum deflection angle of $2\theta_c$, an expected lens resolution of 12.5 nm, and a lens aperture of 300 microns. The experimental data show a net deflection θ_d of $1.1\theta_c \pm 0.05\theta_c$, demonstrating that one can use compound kinoform lenses to focus down to below the critical angle limit.

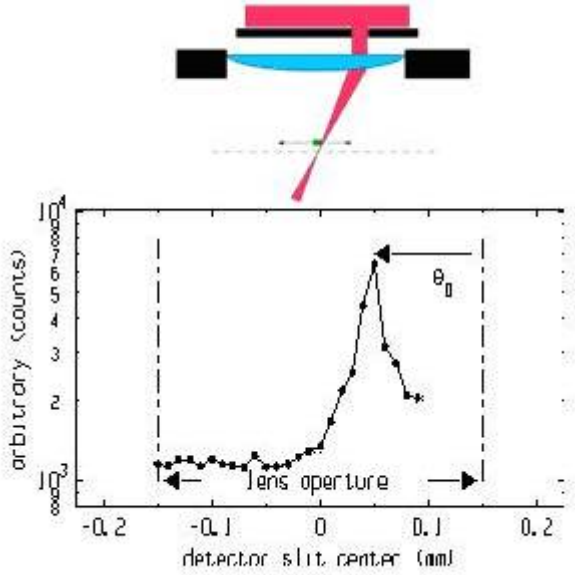

Figure 12.2.33 Experimental verification that one can exceed θ_c with an array of kinoform lenses. The top figure schematically describes the experimental layout, showing a slit limiting incident radiation to the outer part of the lens. A lithographically defined metal marker is scanned through the focus, and the fluorescent signal is shown as a function of position in the bottom panel of the figure.

The optic is an array of four lenses. The bottom panel shows that the array functions as a lens because of the peaked structure. If the peak structure were located at zero, it would function as designed. However, this lens has an aberration. When we measure the deflection angle θ_d, we find that θ_d of $1.1\theta_c = \pm 0.05\theta_c$, clearly larger than θ_c.

12.2.5.2.6 Challenges Associated with Reaching 1 nm with Kinforms

Shown previously in Figure 12.2.27 is a physical implementation of a kinoform structure in silicon. Silicon has been the material chosen to demonstrate many of the kinoform properties because of ease of fabrication. This structure is created by the following steps. A hard mask, typically SiO_2, is deposited as a uniform film onto the lens material. Using electron beam lithography methods, the desired pattern is written into a resist, and this pattern is now transferred into the hard mask. Next, using Reactive Ion Etching methods, the pattern is etched deep into the material, using the patterned hard mask to transfer the pattern. The Bosch process for deep RIE is used.

To move the technology beyond current state of the art and obtain 1 nm spots, we need to address the following issues: limitations of the crossed geometry, etching limitations, and alternative materials and refractive index metrology.

Crossed Lens Geometry

A lens of the type shown will give a line focus, as shown in Figure 12.2.34a. To create a spot, one uses a crossed pair (panel b). Shown in panel c is data showing a spot obtained from such a crossed geometry. The measured spot size was 0.6×4 microns^2, with most of the measured size due to the source and not due to intrinsic properties of the lens. In an earlier section we have addressed the limitations of the crossed geometry. The simulations suggest that the crossed geometry will result in reduced sensitivity to the sharpest spectral features as the numerical aperture of the lenses increases. We do not expect the crossed geometry to be a limitation for 1 nm resolution optics (though to go further one would need to develop radially symmetric lenses, not the linear ones considered here).

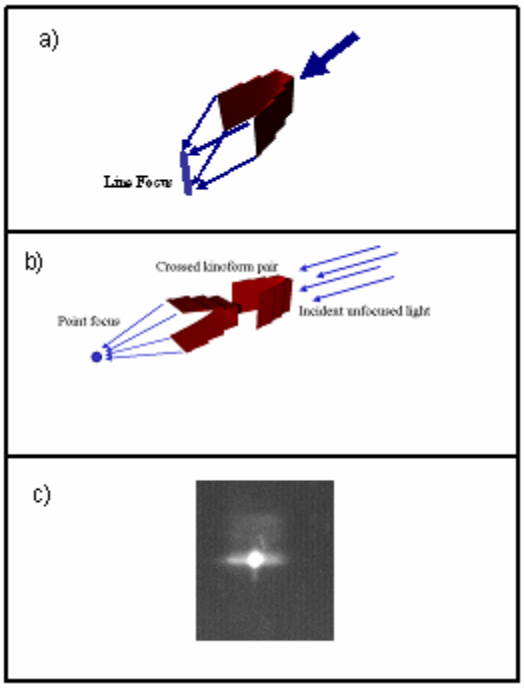

Figure 12.2.34 Use of linear, 1D kinoforms to obtain a focused spot.

a) Single 1D kinoform produces a line focus.

b) Two successive 1D kinoforms, operated as a crossed pair, produce a focused spot.

c) Experimental results from crossed lenses.

Etching Limitations

To obtain high-quality optics, the profile of the optic must match the ideal profile with phase errors less than $\pi/4$. Using micro-fabrication techniques, this is easily achievable due the precision of electron beam writers, which have a spatial placement error of the order of 1 to 10 nm over a 500 micron field. For a typical material with δ of order 10^{-6}, this precision corresponds to phase errors of order $(\lambda * 1\text{nm})/\delta$, approximately $10^{-4}\ \pi$, clearly more than adequate. In fact, the limitations of lens fabrication are primarily due to the etching processes that transfer the electron beam lithographic profiles to the substrate. Shown in Figure 12.2.35 are examples of the etching limitations.

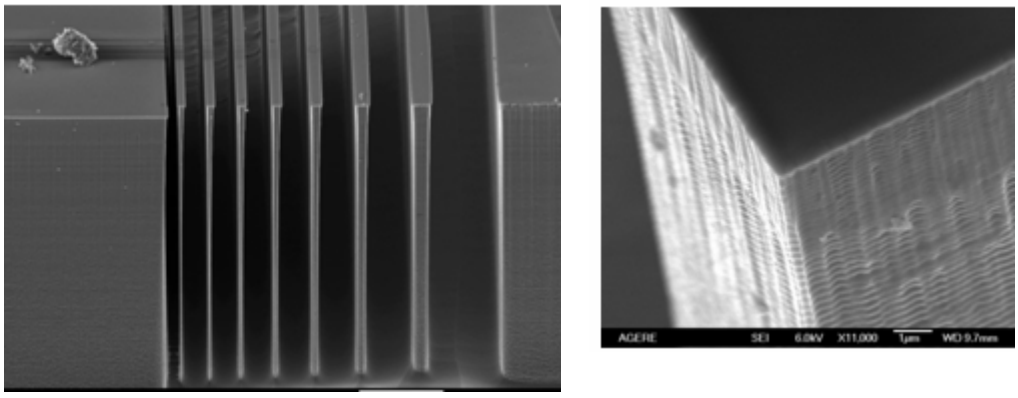

Figure 12.2.35 Two of the current limitations in Si etching technology. Left: Cut-away of a lens structure showing the depth of etching (88 microns, here). Right: Scalloping due to the Bosch process.

On the left is a structure that has been etched down 88 microns. The thinner features exhibit depth-dependent variation in thickness. For optics, it is important to keep a precise shape all the way down the etch depth; in other words, the sidewalls must have 90-degree angles. A further issue seen here is a rounding of the profile near the base. Finally, the right panel shows the scalloping results from the Bosch process. As shown, the scallops measure 200 nm, peak-to-valley.

We believe that both of these problems are solvable. For example, D. Olynick [12.2.23] at LBL has developed a smoother etch process that creates only 10 nm scalloping. Further, the RIE process routinely etches through whole wafers, a depth of 750 microns, and—depending on feature size—can produce the vertical and smooth sidewalls required. Finally, alternative etching methods, such as electrochemical methods, seem to have great potential but have not yet been evaluated for these types of applications.

Alternative Materials

Although silicon has been the material of choice up to this point, to achieve high spatial resolution with reasonable efficiencies requires materials with better optical properties than silicon. We have identified single crystal diamond as one of the better choices, since the transmission through a single lens is 99.4% at 10 keV. However, not only must the optical properties of the materials be better, the precision with which the required lens profiles can be transferred to the materials is just as important to the final lens performance. One must therefore develop fabrication methods for diamond, a project that is already underway. Diamond is a low-density alternative. Some high-density alternatives are Ge and InSb. The advantage of high-density materials is that fewer lenses are needed, which reduces the complexity. For each of these new materials all the steps have to be redeveloped: the deep etch, the hard mask, and the resist. However, for most materials of interest, other market pressures have already spurred some development; commercial etching recipes and tools for these materials are available. However, only in the case of silicon etching do the processes developed comfortably exceed our goals.

12.2.5.2.7 Achieving 1 nm Spot Sizes with Kinoform

There are three key features of kinoforms that potentially enable them to obtain 1 nm spots. First, the kinoform has a transmission function that is almost uniform as a function of increasing lens aperture, so the NA of the lens is not limited by absorption. This contrasts with the pure refractive lenses, which have a transmission function that decreases near the periphery of the lens.

Second, the kinoform does not have to be fabricated with structures as small as the resolution of the lens. This contrasts with the zone plate class of optics, where for efficient operation the smallest feature fabricated is the resolution of the lens. A refractive lens can be fabricated to operate in higher order, but there is a loss of efficiency. A kinoform profile can be optimized to maximize the higher-order focus.

Third, a compound kinoform lens sidesteps the issue of small δ that limits the focusing power of a single lens and otherwise limits the spatial resolution to $0.61\lambda/\theta_c$.

All the key items above have been demonstrated, and no new technology is required to fabricate these lenses. What will be required is to optimize existing fabrication and testing technology. In particular, the weakest link in the process is the quality of the etching process. While no new technology is required, improvements in technology will result in improved performance.

The kinoform lens would consist of an array of at least $(\theta_c\Delta_t)/(0.61\lambda)$ lenses—at least 25 lenses if the material were silicon, 20 lenses for diamond, and 14 for Ge. In all cases these are lower limits, and we expect to actually use approximately 1.5 times as many lenses as this, depending on the manufacturing tolerances. For a manufacturing process that allows smoother sidewalls and smaller feature sizes, the number of lenses will be close to the lower limit.

12.2.5.2.8 Effort Required to Reach 1 nm

To pursue this approach will require access to a high-precision electron beam lithography infrastructure and an etching research infrastructure. It is important that the lithography is precise over areas as large as possible. Usually this requires a stitching together of smaller areas, commonly referred to as the e-beam writing field. The precision of the stitching will limit the pattern placement accuracy, and this in turn will limit the optic resolution.

The etching research effort will have a main direction: using RIE methods on different materials. There will be a small effort to investigate alternative etching methods, such as electrochemical methods, that may have some advantages over RIE but are speculative.

A computational research program will be necessary to further understand the properties of these optics. All the simulation work pursued so far is in the thin lens approximation, and being able to simulate the 3D volume structure, will give increased confidence in understanding the properties and limitations of these optics.

In summary, the kinoform is one possible optics path to focus down to 1 nm. The aperture is not limited by absorption, the structures do not have to be as small as the optic resolution, and by using compound lenses one can exceed the critical angle limit to the numerical aperture. No new technology needs to be invented, but significant optimization and metrology will be required.

12.2.6 Testing of Optics

Traditional interferometric methods (such as those used for telescope mirrors and optical mirrors in state-of-the-art lithography systems) are not directly transferable to the fabrication of hard x-ray optics, because hard x-ray reflective optics must work at grazing rather than normal incidence, and diffractive and refractive optics depend on the transmission properties through a thickness of material rather than just a single surface profile measurement.

12.2.6.1 Investigating Modular Transfer Function

Several techniques have been used to measure the performance of x-ray lenses. Microfabricated test patterns (in particular, “Siemens star” patterns, which contain a broad range of spatial frequencies in a set of radial spokes) provide one approach, while the finest structure sizes can be achieved by viewing thin-film deposition layers end-on or as sliced cross-sections. Since the Modulation Transfer Function of an imaging system is given by the power recorded at a spatial frequency divided by the power present in the object at that frequency, objects of known structure can be used to measure the MTF. However, getting the “known” structure can have its own challenges, because test patterns suitable for x-ray imaging are usually too thick for transmitted electron characterization, and scanning electron microscopes are even more restricted to viewing only the surface layer of a test pattern. Since phenomena such as interlayer diffusion can affect materials’ boundaries at the 1 nm resolution level, it can be challenging to decouple the imaging system from the object. One simple alternative is to use a thin film with random point scatterers known to be smaller than the size of the probe; the power spectrum of an image of such a sample (which could also consist of high-contrast dopant atom clusters in a substrate) can be used to gauge the modular transfer function of the optical system. If there are distinct zeros in the contrast transfer function, one can even attempt to infer that there exist phase reversals in the imaging systems’ transfer function; this is an approach commonly used in electron microscopy.

12.2.6.2 Iterative Phasing Method

Another class of tests has begun to emerge, using iterative phasing methods to go from knowledge of the optic’s pupil function and measurement of the far-field diffraction pattern of the probe, to an estimate of the complex point spread function of the optical system [12.2.24]. These methods are strongly related to lens-less imaging. They offer a way to evaluate the focus of an optic without any need for a particular test pattern, and can be built on expertise available through nearby groups working in coherent diffraction x-ray imaging at Stony Brook University.

12.2.6.3 Coherent Illumination Methods

While incoherent illumination can provide powerful information on optics tested in a full-field imaging system, coherent illumination provides the best mechanism to map spatial frequency response versus position on the optic. (The loss of coherence means the loss of the ability to assign simultaneously precise position and direction values to ray paths in the optical system.) Therefore, it is crucial that NSLS-II have a coherent optics test beamline, and it will be important to develop improved hard x-ray coherent optics test capabilities now, using either NSLS or other sources until NSLS-II comes on line.

References

[12.2.1] Mitutoyo Corporation.

[12.2.2] K.A. Goldberg, P. Naulleau, P.E. Denham, S.B. Rekawa, K. Jackson, E.H. Anderson, and J.A Liddle, "At-wavelength alignment and testing of the 0.3 NA MET optic," *J. Vac. Sci. Technol*. B **22**(6), Nov/Dec 2004.

[12.2.3] W. Chao, B.D. Harteneck, J.A. Liddle, E.H. Anderson, D.T. Attwood, "Soft x-ray microscopy at a spatial resolution better than 15 nm." *Nature* **435**, (June 2005) pp 1210 ff.

[12.2.4] J. Kirz, *J. Opt. Soc. Am.*, **64** (1974).

[12.2.5] M. Panitz, G. Schneider, M. Peuker, D. Hambach, B. Kaulich, S. Oestereich, J. Susini, and G. Schmahl, "Electroplated Gold Zone Plates as X-ray Objectives for Photon Energies of 2–8 keV," AIP Conf. Proc. **507**, 676 (2000).

[12.2.6] Xradia, Inc.

[12.2.7] G. Schmahl, D, Rudolph, and N. Niemann, AIP Conf. Proc., **75** 255(1981).(1980).

[12.2.8] J. Maser, G.B. Stephenson, S. Vogt, et al., Proc SPIE **5539** 185(2004).

[12.2.9] H.C. Kang, J. Maser, G.B. Stephenson, C. Liu, R. Conley, A.T. Macrander, and S. Vogt, "Nanometer linear focusing of hard x rays by a multilayer Laue lens," *Phys. Rev. Lett*. **96**, 127401 (2006).

[12.2.10] P. Kirkpatrick, and A.V. Baez, *J. Opt. Soc. Am*., **38**, 766 (1948).

[12.2.11] S. Suehiro, H. Miyaji, and Hayashi, "Refractive lens for x-ray focus," *Nature* **352**, 385 (1991).

[12.2.12] A. Snigirev, V. Kohn, I. Snigireva, et al., *Nature* **384**, 49 (1996).

[12.2.13] B. Lengeler, C. Schroer, J. Tummler, et al., "Imaging by parabolic refractive lenses in the hard X-ray range," *J. Sync. Rad*. **6**, 1153 (1999).

[12.2.14] Winn et al., *J. Sync. Rad*. **7**, 395 (2000).

[12.2.15] Q. Shen, "X-Ray Flux, Brilliance, and Coherence of the Proposed Cornell High Energy-Recovery Synchrotron Source," CHESS Tech Memo, 01-002, March 2001,.

[12.2.16] J.W. Goodman, *Introduction to Fourier Optics*, McGraw-Hill (Standord Univ.)1996.

[12.2.17] Schroer, *Phys Rev B* **74** 0033405 (2000).

[12.2.18] Bozovic et al., *Nature* **421**, 873 (2003).

[12.2.19] J.A. Jordan, P.M. Hirsch, L.B. Lesem et al., "Kinoform lenses," *Applied Optics*, 9(8), 1883-87 (1970).

[12.2.20] A.I Erko, V.V. Aristov, and B. Vidal, *Diffraction X-Ray Optics*, IOP Publishing, Bristol, Philadelphia (1996).

[12.2.21] Lui et al., *J. Appl. Phys.* **98**, 113519 (2005).

[12.2.22] W.C. Sweatt, "Describing holographical optical elements as lenses," *J. Opt. Soc. Am*. **67** (6), 803-808 (1977).

[12.2.23] D. Olynick , private communication.

[12.2.24] H.M. Quiney, A. G. Peele, Z. Cai, D. Paterson, and K. A. Nugent, "Diffractive imaging of highly focused x-ray fields," *Nature Physics,* 2006.

12.3 Nanopositioning Instrumentation

At NSLS-II, the required instrument positioning performances and capabilities—such as resolution, dynamic range, repeatability, speed, and multiple axes synchronization—will exceed the limit of commercial availability. In this section, we present the nanopositioning instrumentation requirements and techniques to be developed for the NSLS-II project.

12.3.1 Real-Space Linear Nanopositioning for a Nanoprobe Scanning System

Given NSLS-II's outstanding brightness, a hard x-ray nanoprobe with nanometer scale resolution (Section 11.4) will be a very powerful x-ray characterization tool for the nanoscience community. This kind of unique instrument will also offer diverse capabilities in studying nanomaterials and nanostructures, particularly for embedded structures. The combination of diffraction, fluorescence, and phase contrast in a single tool will provide unique characterization capabilities for nanoscience. Multi-axis scanning stages with subnanometer, real-space positioning resolution are key components for the x-ray nanoprobe with 1 nm focal spot.

12.3.2 Requirements and Issues

The major technical challenge for the design of a scanning stage system for the NSLS-II nanoprobe is its requirement for positioning resolution and stability on the sub-nanometer scale, together with a travel range on the order of centimeters. With advances in the fabrication of novel x-ray optics and an optimized beamline design, we expect to be able to achieve a 1 nm focal spot at NSLS-II. Imaging and spectroscopy at this resolution will require staging of x-ray optics and specimens with a relative mechanical stability and repeatability of better than 0.3 nm.

Figure 12.3.1 shows a multidimensional scanning stage system for a typical scanning hard x-ray nanoprobe. As shown in the figure, the nanoprobe consists of three major component groups: a supporting base, a stage group for the x-ray focusing optics, and a stage group for sample holders.

The stages for x-ray focusing optics provide a 3D positioning capability with 0.3 nm resolution in a 12×12×12 mm travel range. An x-ray optics holder is mounted on the top of the stage group, which consists of two sets of mini stages: a pair of x–y stages for alignment of the optical Order-Sorting Aperture (OSA), and a set of hybrid micro stages for alignment of the x-ray focusing optics. The stage group for the sample holder is composed of x–y–z scanning stages and a rotary stage for x-ray tomography applications. Table 12.3.1 shows an expected design specification for the NSLS-II x-ray nanoprobe.

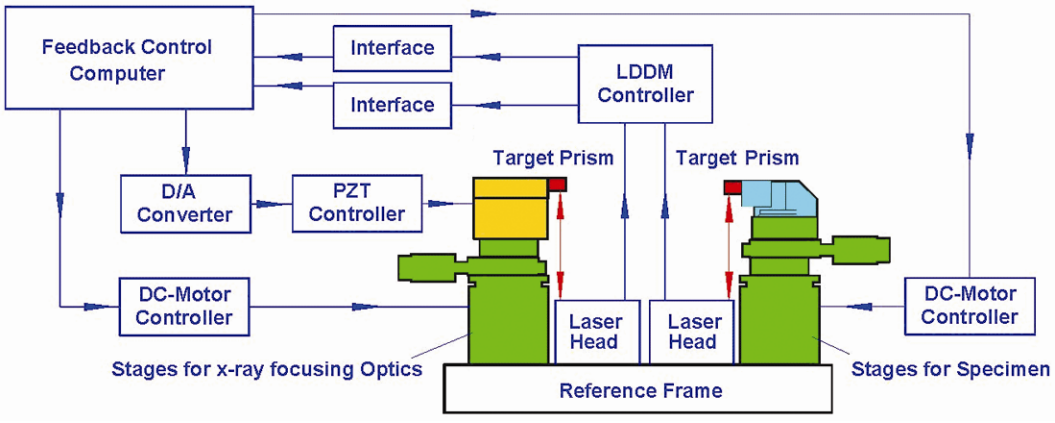

Figure 12.3.1 Schematic of multidimensional scanning stage system for a typical scanning hard x-ray nanoprobe.

Table 12.3.1 Expected Specifications for the NSLS-II Nanoprobe Scanning Stages.

	X-ray focusing optics scanning stages	Sample scanning stages
Overall dimension [mm]	230 (X) x 236 (Y) x 230 (Z)	230 (X) x 268 (Y) x 230 (Z)
Normal load capacity [kg]	3	3
Coarse motion stage type	DC-servo motor with gearhead	DC-servo motor with gearhead
Coarse motion dimension	3 linear	3 linear, 1 rotational
Coarse travel range [mm]	12 (X) x 12 (Y) x 12 (Z)	12 (X) x 12 (Y) x 6 (Z)
Coarse min. incremental motion [nm]	100	100
Coarse unidirectional repeatability [nm]	200	200
Fine motion stage type	PZT with motion reduction	Rotation stage range: Continuous
Fine motion dimension	2 linear	Min. incremental motion (μrad) 6.3
Fine travel range [mm]	2 (X) x 2 (Y)	Rotational repeatability (μrad) 50
Fine min. incremental motion [nm]	0.05	
Fine unidirectional repeatability [nm]	0.3	

Ambient vibrations will be a serious problem for such a facility. For example, at APS, the typical vibration level on the floor in the experimental station is about 10 nm in the frequency range below 10 Hz. This will be a major issue for operating of the scanning stage system in such an environment with a relative mechanical stability and repeatability of better than 0.3 nm. At NSLS-II, the facility will be designed literally from the ground up, to minimize sources and transmissions of vibration. Further, the sandy soil of the NSLS-II site has good vibration damping characteristics. Finally, a detailed finite element analysis of the entire facility, with particular attention to the nanoprobe beamline, will be carried out with a view to taking extra isolation measures for that beamline. Nevertheless, active vibration control on the subnanometer scale will be one of the key technical approaches for this project.

12.3.3 Survey of Technical Approaches

Subnanometer positioning resolution has been achieved by positioning stages for Scanning Tunneling Microscopes and various scanning Atomic Force Microscopes for many years. However, there are major specification differences between stages for STMs or AFMs and stages for scanning hard x-ray nanoprobes. As shown in Table 12.3.2, the working distance between the cantilevered working tip of an STM or AFM and the sample surface is on a nanometer scale, but the working distance between a hard x-ray focusing optic and its specimen for the NSLS-II hard x-ray nanoprobe will be ~10 mm. Further, the weight of a scanning microscope's cantilevered tip is typically in grams or significantly less. The weight of a single soft x-ray zone plate (for example) may be in the same range, but a group of such plates for a hard x-ray nanoprobe with its alignment structures and any optical OSA could weigh a few hundred grams. Finally, in the case of using hard x-ray focusing optics with multilayered diffractive lens techniques or advanced KB mirror systems, the weight of a hard x-ray optics system with 1 nm focal spot may weigh more than a kilogram, using today's commercially available stages.

Requirements for the stage's travel range also differ greatly between typical STM sand AFM stages and the stages for a hard x-ray nanoprobe. The travel range for a typical tip-tilt PZT scanning device is in the range of 50 microns. In contrast, required travel ranges are typically 10×10×10 mm for the stages carrying x-ray focusing optics. Based on these comparisons, it is clear that there are no simple solutions for mounting optics on a small, light, stiff scanning stage along the lines of the STM approach without a significant compromise on the stages specifications because of the 2 to 6 orders of magnitude difference between them.

Table 12.3.2 Comparisons of Scanning Stages for STMs, AFMs, and a Hard X-Ray Nanoprobe.

	Stages for STM and AFMs	Stages for hard x-ray nanoprobe
Working distance [mm]	< 0.00001	10–30
Load capacity [kg]	< 0.001	0.2–1
Travel range [mm]	< 0.1	> 10

A hard x-ray nanoprobe is currently being constructed at the Center for Nanoscale Materials at APS. The system is designed to accommodate x-ray optics with a resolution limit of 10 nm; therefore, it requires staging of x-ray optics and specimens with a mechanical repeatability of better than 5 nm [12.3.1]. A prototype of the APS/CNM nanoprobe, which is acting as an "Early User Instrument" or EUI, is operational. It demonstrated a relative mechanical stability and repeatability of better than 4 nm between its zone plate optics holder and sample holder [12.3.2]. Because this EUI stage system represents the current design, we use it as an example of the technical approaches for the development of an NSLS-II nanoprobe scanning stage system.

12.3.3.1 General Structure of the APS/CNM EUI

As shown in Figure 12.3.2, the EUI developed by APS/CNM consists of three major component groups: a supporting base with 2D differential laser Doppler displacement encoder system, a stage group for the x-ray optics, and a stage group for sample holders [12.3.2]. The entire scanning system was designed with high stiffness, high repeatability, low drift, flexible scanning schemes, and the possibility of fast feedback for differential active vibration control. To allow maximum flexibility in the design of the stage group for specimen holders, all high-precision positioning and scanning is performed by the optics stage group, whereas the specimen stage group is used for coarse positioning only.

Ideally, the base structure should be made from materials with good thermal stability, such as invar or Zerodur. The APS prototype is built of aluminum alloy. Four sets of laser heads and 16-reflection optics for the Laser Doppler Displacement Meter [12.3.3] were mounted on the base structure to perform 2D differential measurements between the x-ray optics holder and the sample holder. To ensure stability of the LDDM, a set of thermal and acoustic shields reduces the influence of heat from the laser heads.

The stages for zone plate optics provide 3D positioning capability with 0.125 nm resolution in the 12x12x12 mm range. The EUI includes three commercial DC-motor driven translation stages and two PZT-driven high-stiffness stages developed at Argonne using a redundantly constrained laminar structure weak-link mechanism for ultra precision motion control. A zone plate holder was mounted on the top of the stage group, which consists of two sets of mini stages: a pair of x–y commercial DC-motor stages for optical OSA alignment, and a set of picomotor-driven weak-link x–y–z stages developed at Argonne for aligning multiple zone plate optics.

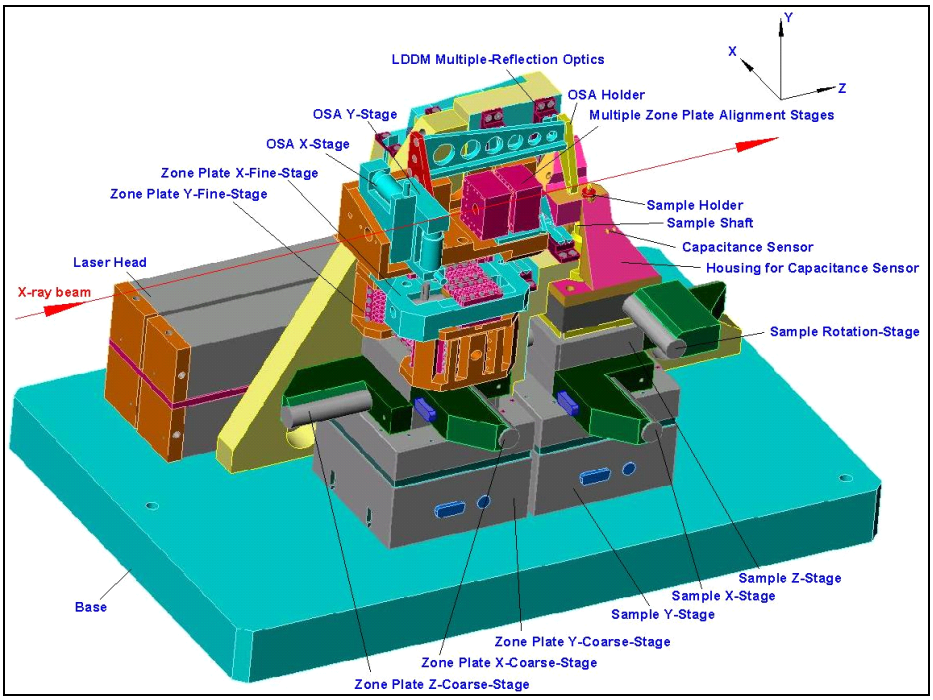

Figure 12.3.2 Model for the x-ray nanoprobe prototype at Argonne. Thermal shields are not shown.

The stage group for the sample holder is composed of three commercial DC-motor driven x–y–z scanning stages and a DC-motor-driven rotary stage for x-ray tomography applications. To improve the sample positioning accuracy, two pairs of capacitance sensors were used to dynamically measure the angular and displacement shifts of the rotation axis. The position of the sample will be determined by a combination of the LDDM system and the capacitance sensor system.

The APS/CNM EUI incorporates a number of design innovations that would also be utilized in any NSLS-II instrument. The first of these is to use a laser encoder system from Optodyne, Inc. with excellent performance (2 mm resolution) that is independent of polarization. This allows the use of multiple reflections (Figure 12.3.3) to create a novel design with subnanometer linear resolution [12.3.4–12.3.6]. In this design the optical path provides eight times greater resolution for linear displacement measurement and encoding. The travel ranges for these stages are ~12 mm, more than sufficient for these applications. Figure 12.3.3 shows the placement of the prisms on the optics stages and on the sample stages.

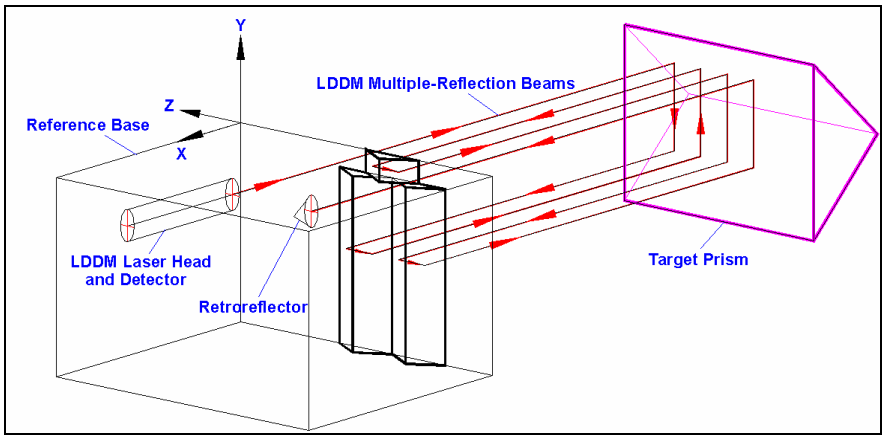

Figure 12.3.3 Schematic of the self-aligning multiple-reflection optical design. With the same laser source and detector electronics, this optical path provides eight times greater resolution.

The second design innovation is to use novel weak-link linear motion reduction mechanisms to perform linear motion closed-loop control at the sub 100 pm level with a micron-level travel range. The structure

consists of four groups of overconstrained, weak-link parallelogram mechanisms [12.3.7, 12.3.8]. The precision of the modern photochemical machining process using lithography techniques makes it possible to construct a strain-free (or strain-limited) overconstrained mechanism on a thin metal sheet. By stacking these thin metal weak-link sheets with alignment pins, a solid complex weak-link structure can be constructed at reasonable cost.

Two sets of piezoelectric-transducer-driven horizontal and vertical high-stiffness weak-link stages have been developed with different travel range and resolution for fine-motion control. The high-resolution, weak-link stages have a 0.02 nm resolution with a 1/15 motion-reduction mechanism and a travel range of 1.5 microns [12.3.7]. For the medium-resolution, weak-link stages, multiple PZT drivers are applied, to guarantee the linear motion trajectory accuracy in a specific direction. The resolution of the stage is 0.3 nm, with a travel range of 15 microns. Physik Instrumente™ PZT actuators with strain-gauge sensor servo-control modules were used to drive both high- and medium-resolution weak-link stages [12.3.9].

12.3.3.1.1 Gap between NSLS-II Requirements and Current EUI Achievement

The EUI differential scanning stage system with the high-resolution weak-link stages has been tested at APS [12.3.7]. As shown in Figure 12.3.4, a series of 1 nm and 3 nm vertical and horizontal differential displacement steps (between zone plate optics holder and specimen holder) have been demonstrated with closed-loop control.

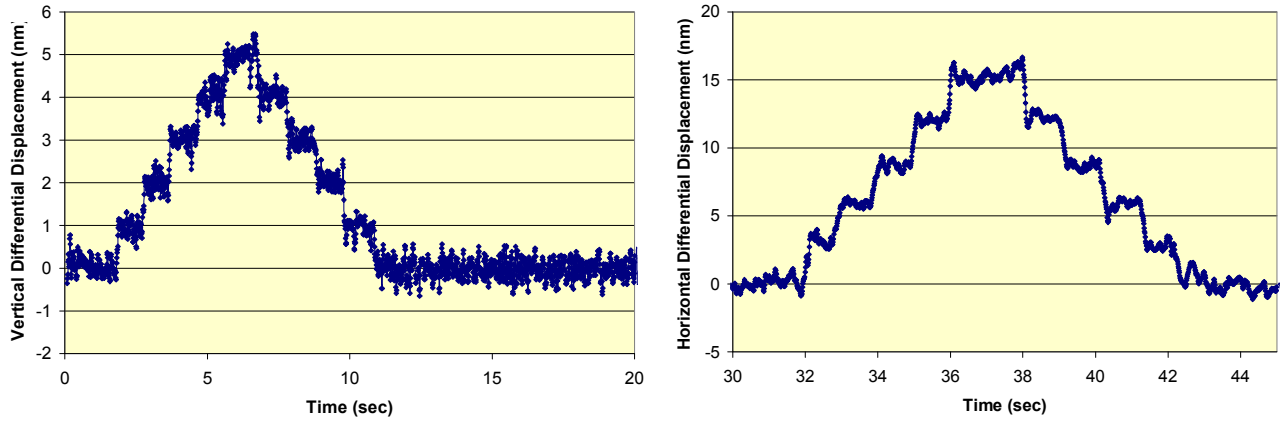

Figure 12.3.4 Closed-loop controlled differential displacement steps test with high-resolution weak-link stages.

Figure 12.3.5 shows an active vibration control test with the prototype system. During this test, the closed-loop control system performed a damping action in response to a single external mechanical disturbance (an 80 kg mass dropped to the floor from 0.2 m height at 3 m away).

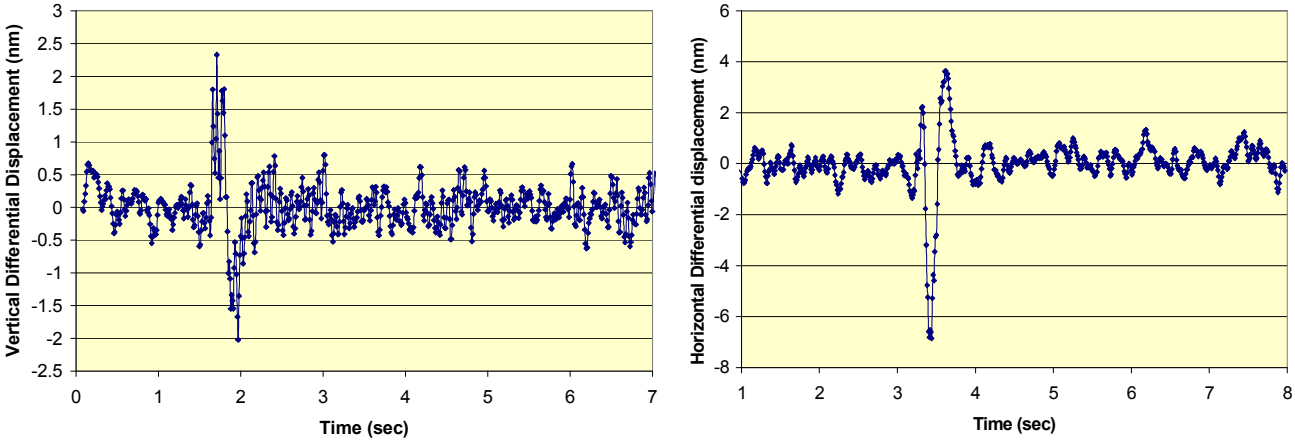

Figure 12.3.5 Active vibration control test with high-resolution weak-link stages.

It is obvious that there is a gap between the positioning resolution requirement for the NSLS-II nanoprobe and the test results from the APS/CNM EUI scanning stage system. For the differential positioning resolution in the vertical direction, the NSLS-II system will need a more than three-fold improvement. A 10-fold improvement will be required in the horizontal direction. Therefore, to meet the technical goal of the NSLS-II nanoprobe project, a significant research and development effort is necessary.

12.3.3.1.2 R&D Program

Figure 12.3.6 shows an active vibration control test result at APS with a 1D stage using a similar LDDM encoder system. A series of 0.1 nm, 0.2 nm, and 0.3 nm steps is demonstrated [12.3.2]. The laser beam is reflected back and forth 12 times between the fixed base and the moving target in this test. This result indicates that the goal of 0.3 nm positioning resolution is achievable in a 1D stage system with a rigid supporting structure. The challenge will be to duplicate this performance in a 3D stage system with significant travel. These results suggest that this is possible, but it will require detailed analysis and development work.

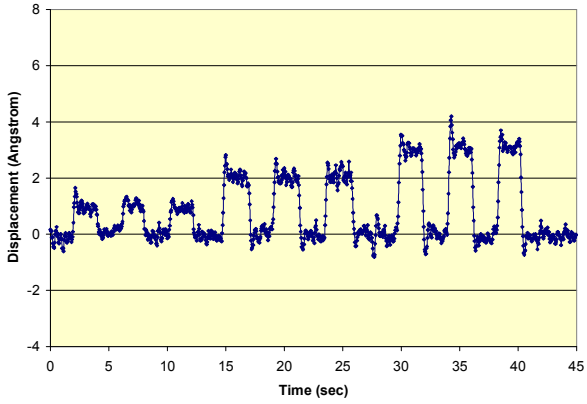

Figure 12.3.6 Closed-loop control scheme test for a 1D setup. A series of 0.1 nm, 0.2 nm, and 0.3 nm steps is demonstrated.

The R&D program will focus on the design, analysis, and development of a stage system with superb structural rigidity and advanced control strategy for multidimensional active vibration control. Specifically, a new prototype stage system will be built and tested under this R&D program to prove the design principle for

the NSLS-II scanning stage system and to ensure the success of the novel NSLS-II nanoprobe instrument. The tasks of this R&D program include:

- designing a scanning stage system that meets the system resolution and load capacity requirements with high stiffness and a 3D size as small as reasonably achievable
- optimizing the stage's motion trajectory accuracy to reduce the coupling motion between dimensions
- developing advanced control mechanism for multidimensional active vibration control

12.3.3.1.3 Real-Space Angular Positioning and 6D Angular/Linear Hybrid Positioning

Besides the 3D linear positioning stages, there are needs for high-precision angular positioning stages and 6D angular/linear hybrid positioning systems for the hard x-ray nanoprobe instrument. Most of these stages are commercially available for customization, such as a precision rotary stage for tomography applications and a 6D robot-arm-based detector manipulator for microdiffraction applications.

However, there are technical challenges in the design of angular positioning devices for the alignment of x-ray focusing optics with 1 nm focal spot, such as the MLL [12.3.10]. The challenges come from not only the level of precision and stability required by the x-ray optics, but also from the requirements of the structure for compactness and from the complexity of the multidimensional alignment system—because the motion tolerances needed to avoid crushing these tiny, fragile, expensive lenses are very tight. Moreover, since these alignment devices comprise the bulk of the load of the scanning stages, they must also be designed with high stiffness and to be as lightweight as possible.

Using MLL optics as an example, four linear Laue lenses are needed to obtain a 2D x-ray focus. Each lens requires individual remote 3D angular adjustment and 1D or 2D linear adjustment [12.3.11]. Since a typical lens has dimensions of 1×0.3×0.025 mm, the interface between the lens and the alignment stages needs a special, high-stiffness mounting coupling.

The 3D angular adjustment requires a resolution of 10 mrad that is achievable with a PZT-driven weak-link structure over a travel range of 1 to 2 degrees. Since one of the 3D angular motions requires a 22-degree travel range [12.3.11], a special high-stiffness rotary shaft must be developed.

12.3.3.1.4 R&D Program for Miniaturized Angular Positioning

This R&D program will focus on the development of a set of miniaturized goniometers to meet the needs of remote alignment for novel hard x-ray focusing optics such as the MLL. The tasks of this R&D program include:

- designing a 3D miniaturized motorized (or PZT-driven) goniometer system with high stiffness and a size as small as reasonably achievable
- optimizing the goniometer's structural dynamics performance to ensure the optics positioning stability for a 1 nm hard x-ray focal spot
- developing an equipment protection control strategy for the hard x-ray focusing optics

Two prototypes may be developed through this R&D program. The first prototype will provide an early working test-bed for the hard x-ray focusing optics. This first prototype will also provide the practical information for optimizing the design specifications for the second prototype, which will ensure that the final design goal for the NSLS-II nanoprobe project is achieved.

12.3.3.1.5 Absolute Accuracy at Subnamometer Scale

Finally, we note that for motion resolution on the 10 pm scale, with traceability to NIST standards, we have an existing strategy [12.3.12] that has been proven [12.3.13] to work, and is compatible with the NSLS-II environment. This would be most useful for measuring on an absolute scale the size of the focused spot, for

spot sizes ~1 nm. The x-ray interferometer was invented by Bonse and Hart [12.3.14] and has since found most application in x-ray physics to extremely precise measurements of x-ray scattering factors. It was immediately realized that its extreme sensitivity to displacements, down to 10 pm or less, makes it a very powerful metrological tool. Hart [12.3.15] showed that a suitable elastic translation could be built into the interferometer to give total displacements on the order of one micron, hence giving a useful overlap with larger-scale transducers, and this has been used to refer the silicon crystal spacing to the NIST optical (krypton) standard. Since silicon crystals are available with high perfection in bulk for the semiconductor industry, this provides a portable absolute length standard to a precision of 1 part in 10^6, referred to the krypton standard. Figure 12.3.7 shows a conceptual schematic of the interferometer for this application.

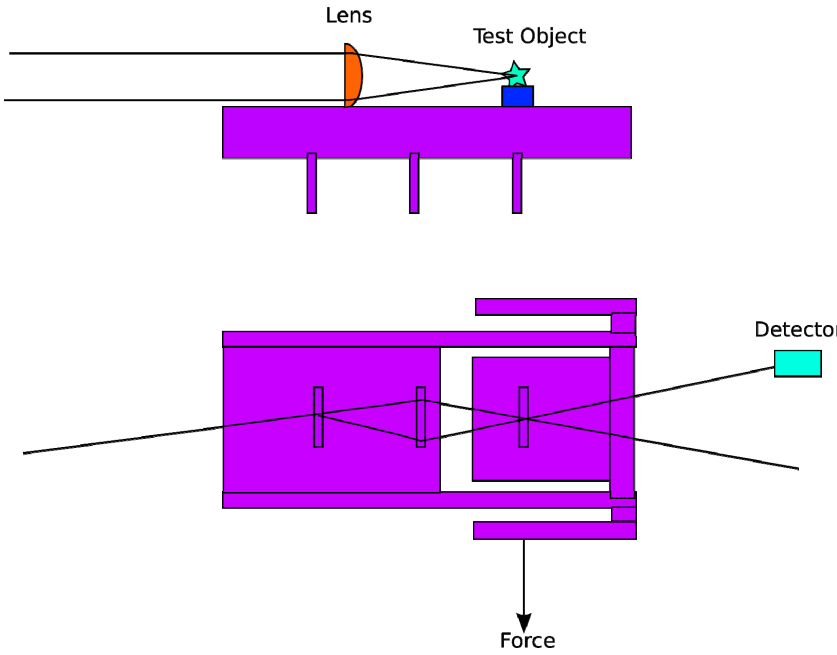

Figure 12.3.7 Conceptual schematic of an interferometer to precisely measure x-ray scattering factors.

References

[12.3.1] J. Maser, G. B. Stephenson, D. Shu, B. Lai, S. Vogt, A. Khounsary, Y. Li, C. Benson, G. Schneider, SRI 2003, AIP Conf. Proc. 705, (2004) 470-473.
[12.3.2] D. Shu, J. Maser, B. Lai, and S. Vogt, SRI 2003 Conf. Proc., 705, AIP (2004) 1287-1290.
[12.3.3] LDDM is a trademark of Optodyne, Inc., 1180 Mahalo Place, Compton, CA 90220, U.S.A.
[12.3.4] U.S. Patent granted No. 5,896,200, D. Shu, 1999.
[12.3.5] U.S. Patent granted No. 6,822,733, D. Shu, 2004.
[12.3.6] D. Shu, J. Maser, B. Lai, S. Vogt, M. Holt, C. Preissner, A. Smolyanitskiy, B. Tieman, R. Winarski, and G.B. Stephenson, to be published in the proceedings of X-ray Microscopy 2005, Himeji, Japan, July 2005.
[12.3.7] D. Shu, J. Maser, M. Holt, B. Lai, S. Vogt, Y. Wang, C. Preissner, Y. Han, B. Tieman, R. Winarski, A. Smolyanitskiy, and G. B. Stephenson, to be published in the proceedings of SPIE Optomechanics 2005.
[12.3.8] U.S. Patent granted No. 6,607,840, D. Shu, T. S. Toellner, and E. E. Alp, 2003.
[12.3.9] Instruction manual, Physik Instrumente GmbH & Co., Germany, 2003.
[12.3.10] H. C. Kang, J. Maser, G. B. Stephenson, C. Liu, R. Conley, A. T. Macrander, and S. Vogt, "Nanometer Linear Focusing of Hard X Rays by a Multilayer Laue Lens," *Phys. Rev. Lett*. **96**, 127401 (2006).
[12.3.11] J. Maser, private communication, May 2006.
[12.3.12] D. G. Chetwynd, D. P. Siddons, and D. K. Bowen, *J. Phys. E: Sci. Instrum*. **16**, 871 (1983).

[12.3.13] D. K. Bowen, D. G. Chetwynd, and D. R. Schwarzenberger, *Meas. Sci. Technol.* **1**, 107 (1990).
[12.3.14] U. Bonse and M. Hart, *Appl. Phys. Lett.* **6**, 155 (1965).
[12.3.15] M. Hart, J. Phys. D: *Appl. Phys*. **1**, 1405 (1968).

12.4 High Energy Resolution Optics

One of the goals of the NSLS-II project is to achieve 0.1 meV energy resolution for inelastic x-ray scattering experiments. This is an extremely challenging goal and represents more than an order of magnitude increase in resolution over the existing state-of-the-art. In addition to placing very high demands on the x-ray source to produce very high fluxes per unit bandpass, achieving this energy resolution will require new optics developments. In this section, we outline the R&D necessary to accomplish this.

12.4.1 Introduction

High-resolution inelastic x-ray scattering spectrometers are currently in use at all of the third-generation x-ray sources. The highest resolution achieved at these instruments to date is ~1 meV; routine resolution for practical experiments is 1.5 → 2 meV. Without exception, all these spectrometers (at ESRF, SPring-8, and APS) utilize high-order Bragg reflections from perfect Si crystals, operating at near-backscattering energies, to achieve the high resolution and high-angular acceptance that is required. Analyzer crystals used in these instruments are comprised of large numbers of perfect blocks glued to a spherical substrate to ensure the inelastically scattered x-rays are collected over a large solid angle (to increase count rates) without at the same time introducing the strain broadening that would otherwise be incurred by bending perfect crystals. This spherical curvature of the collection of small diced blocks acts to focus the reflected x-rays onto a detector located near the sample. Typically, several such analyzer–detector combinations are employed to increase data rates by collecting data from multiple positions in reciprocal space simultaneously.

In the left panel of Figure 12.4.1, the energy width of various Si reflections are plotted as a function of the photon energy for which these reflections occur in back-scattering. The size of the points is proportional to the reflectivity of that reflection. The general trend is very clear: to achieve high energy resolution, one is forced to utilize high photon energies. Further, the higher the resolution (smaller ΔE), the smaller the reflectivity. These fundamental facts have three negative consequences.

First, the higher photon energies mean that one is forced to utilize a non-optimum portion of the undulator spectrum—specifically, well beyond the maximum flux. This problem is particularly severe for a medium-energy ring such as NSLS-II. As can be seen from Figure 12.4.1, operating at ~1 meV resolution requires photon energies of >21 keV and to achieve 0.1 meV would require photon energies in excess of 31 keV. Figure 11.5.2 shows that at these energies the flux output from a U19 device, for example, is lower by more than two orders of magnitude at 30 keV compared to 10 keV, as measured in ph/meV, the figure of merit for an inelastic experiment. Second, the high-order Bragg reflections have increasingly smaller reflectivities, and thus any device based on such reflections will be increasingly inefficient—a real problem for this technique in which experiments are extremely photon-hungry. Third, operating at high photon energies, while offering some advantages in terms of penetration depth, also means inherently worse reciprocal space resolution for the same collection solid angle, relative to lower photon energies.

For these reasons, extending existing Si technology to use in inelastic analyzers operating at 0.1 meV energy resolution does not appear practical and it is necessary to seek alternatives.

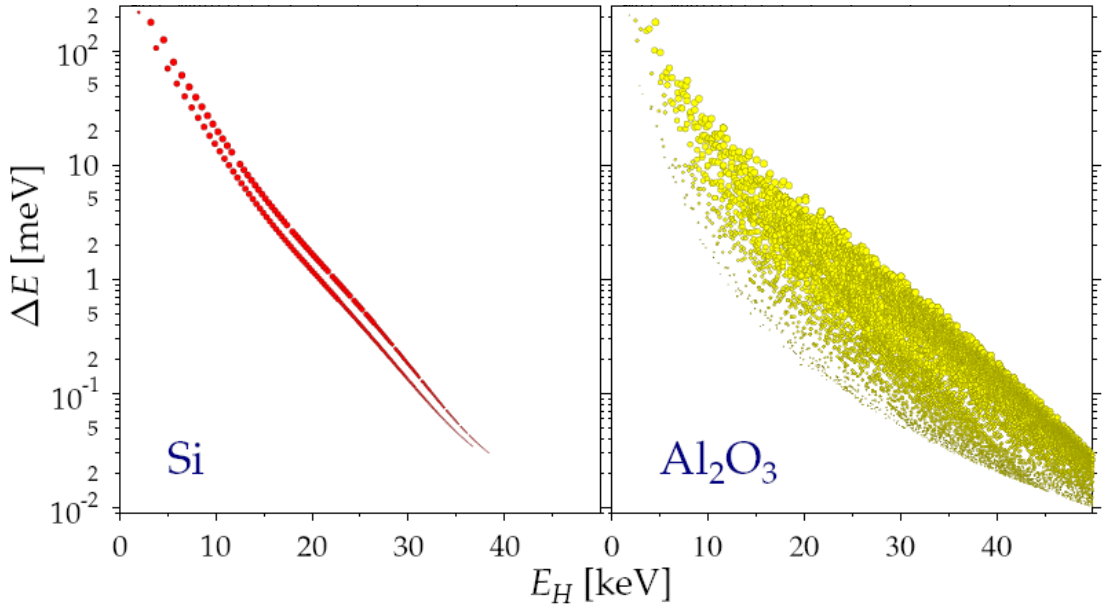

Figure 12.4.1 Energy bandpass for the Bragg reflections in Si and sapphire as a function of the photon energy for which these reflections occur in backscattering. In each case, the size of the point corresponds to the reflectivity of that reflection. The general trend in each case is that higher resolutions are achieved at higher photon energies and with smaller reflectivities.

One possibility is to continue to use perfect crystals in backscattering, but seek alternative (non-cubic) materials that have narrower energy bandpasses, at lower photon energies compared to Si. An example of this approach might be sapphire or quartz. As shown in the right panel of Figure 12.4.1, sapphire can offer reflections that have energy bandpasses as small as 0.1 meV (at high energies). However, sapphire does not appear promising for such very high resolutions, for two reasons. First, in order to get the very high resolutions for low-order reflections requires a very large extinction length—that is, the structure factor is small. From this it follows necessarily that the reflectivity (and hence the efficiency) is low. Further, since the extinction length is (at these resolutions) now comparable to the absorption length in the material, the reflections develop large angular tails (and therefore equivalent tails in energy scans) that would greatly complicate experimental measurements at small energy transfers. The second reason is that, in addition to these fundamental problems, there are severe technical challenges associated with the fabrication of large arrays of such crystals from these materials, challenges which may be insurmountable. We have chosen, therefore, not to pursue such approaches to reach 0.1 meV resolution. We note, however, that it may be useful to utilize quartz and sapphire, or related noncubic materials, for lower resolutions, perhaps >1meV at moderate photon energies.

12.4.2 Asymmetric Optics

Following the discussion above, we have chosen to pursue an alternative approach to achieving very high energy resolutions; that is, to utilize the angular dispersion of x-rays from highly asymmetrically cut crystals. This approach is based on the principle that any asymmetrically cut crystal operating at a Bragg reflection acts as a dispersive element with any wavelength spread in the incident beam, generating angular spread in the exit beam. This concept is illustrated schematically in Figure 12.4.2. Achieving high energy resolution then translates into the much simpler task of achieving high angular resolution, something that may be obtained with more conventional Bragg optics at relatively low energy. Furthermore, by choosing to operate in backscattering, one may tune the dispersive effects simply by tuning the asymmetry angle. Thus one may achieve very high energy resolutions (on the order of $\Delta E/E \sim 10^{-6}$–10^{-8}) even at moderate photon energies (5–10 keV). This approach has been discussed in several articles by Y Shvyd'ko and is discussed at length in [12.4.1].

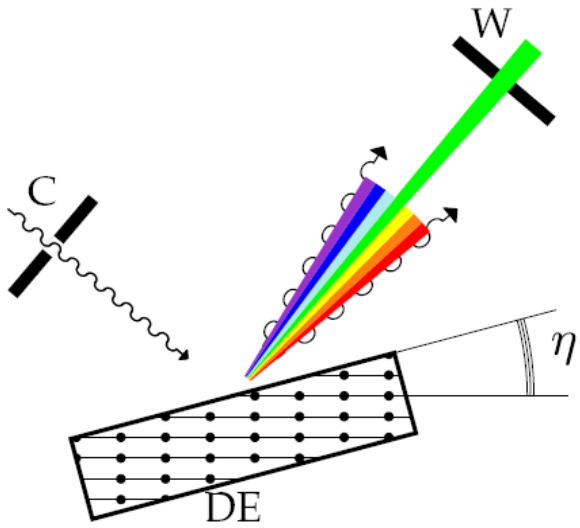

Figure 12.4.2 Schematic illustration of the concept of monochromatization through angular dispersion. An incident beam is collimated by C and Bragg diffracts from an asymmetrically cut crystal. Energy spread in the incident beam is transformed into angular spread in the exit beam. A wavelength selector (W) then selects a given energy bandpass by selecting a particular angular spread. The angular dispersion, and hence the energy resolution, is controlled by the asymmetry angle, η, not by the intrinsic width of the Bragg reflection.

With this approach, the goal of 0.1 meV energy resolution appears feasible. Further, there are a number of advantages inherent to working at lower photon energies, including improved reciprocal space resolution (for the same collection solid angle), proximity to transition metal K-edges (and their possible resonant effects), more efficient detectors, extremely steep wings in the resolution function, and, as discussed above, the intrinsic flux advantage of working closer to the peak of the undulator spectrum.

Chapter 11 discusses a possible spectrometer concept (including the monochromator, sample spectrometer, and analyzer) utilizing such asymmetric optics. However, there are significant risks associated with developing an instrument based on these untried principles today. We outline here an R&D program to mitigate these risks. The goal of this program is to demonstrate the feasibility of the asymmetric optics approach such that one may then design and construct an instrument with a high degree of confidence that it will function as intended.

This R&D plan has been informed by the early work of Shvyd'ko et al. at APS, who have recently taken the first steps in demonstrating the validity of the design principles mentioned here. Figure 12.4.3 shows a schematic of their experimental setup in which two Si(800) crystals, cut with an asymmetry angle of 88.5°, were tested, operating in backscattering at 9.1 keV. The two crystals (labeled D in the figure) were operated back-to-back such that one crystal acted as a monochromator (with a collimator, C, and wave-length-selector, W, collimating the beam and selecting the appropriate wavelength/angular spread, respectively) and the second crystal acted as an analyzer. The W and C crystals were fabricated from a single monolithic block of Si, as shown in Figure 12.4.4. The dispersive elements were comprised of Si(800) crystals 175 mm long, shown in Figure 12.4.5. The relative energy transfer between the two components can be tuned by varying the temperature of one of these dispersive elements with respect to the other. This changes the lattice constant of one piece of Si with respect to the other and hence the energy for which the backscattering condition is obtained. Thus energy scans are, in fact, temperature scans. Similar principles have been tried and tested in more conventional inelastic spectrometers.

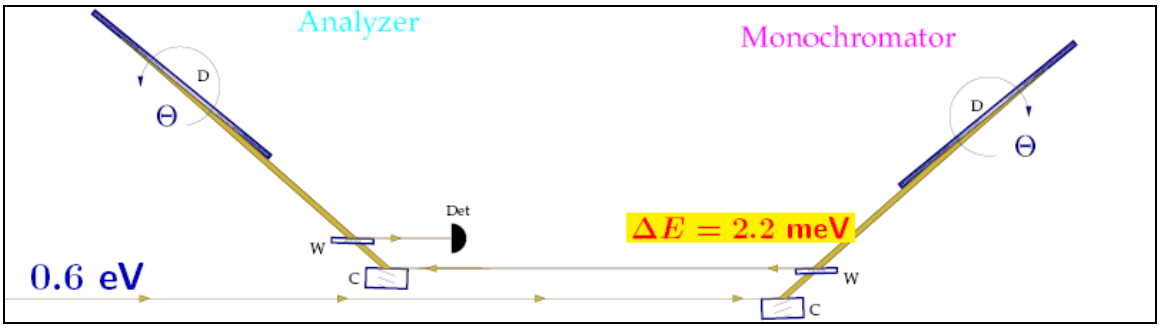

Figure 12.4.3 Arrangement of monochromator and analyzer crystals used in the initial experiments performed at 3ID at APS. The energy resolution of each component was found to be 2.2 meV at an incident photon energy of 9.1 keV.

The experiments, performed at 3ID at APS, demonstrated that the principles discussed above do indeed work—it is possible to construct a monochromator and analyzer based on angular dispersion effects.

However, these first steps remain a long way from making 0.1 meV spectrometers a reality. In particular, the overall resolutions of the instrument in Figure 12.4.3 was 3.1 meV, as show in Figure 12.4.6 [12.4.2, 12.4.3]; that is, each of the two components (monochromator and analyzer) contributed ~2.2 meV energy resolution. This is significantly larger than the theoretically calculated value of 0.7 meV.

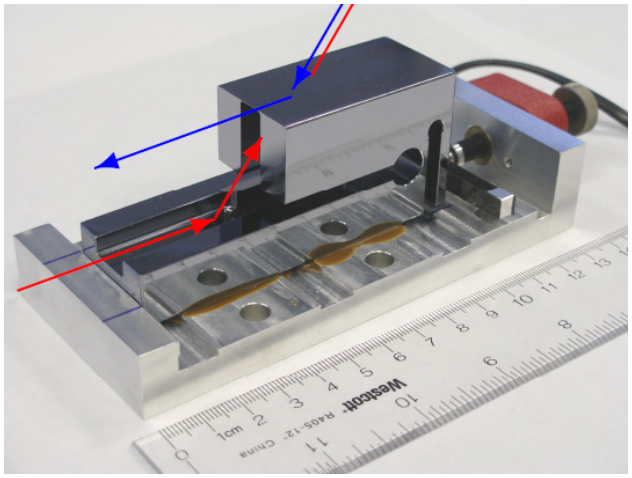

Figure 12.4.4 Monolithic Si crystal used as the collimator (C) and wavelength selector (W) in the experiments at APS. The incident beam (red line) is collimated by the first reflection, and passes through a 200 μm thick section of the crystal. It is then diffracted off a long dispersive element (not shown in this figure) and diffracted from the top surface of the thin section (blue line), which passes only a narrow angular (and therefore energy) spread to the detector.

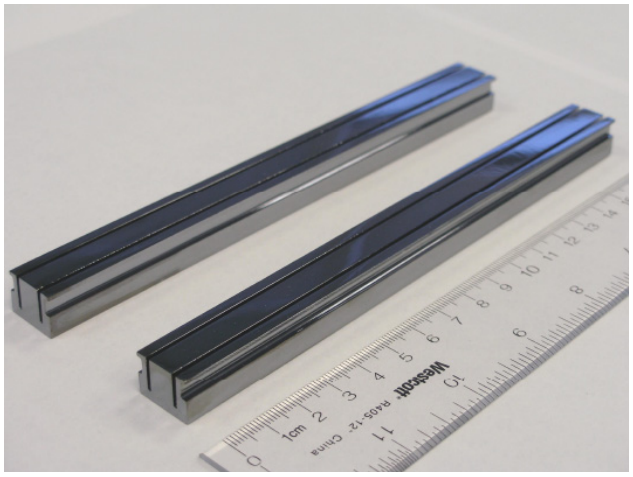

Figure 12.4.5 Si(800) crystals used as the dispersive elements in the experiments at APS. The crystals are 175 mm long and have an asymmetry angle of 88.5°.

The central questions of the R&D program will be to understand why the resolution is broadened beyond the theoretically expected result and then, based on this understanding, to construct prototype devices that demonstrate theoretical performance in resolution and throughput at the 0.1 meV level. Based on the preliminary experiments, a number of possible factors contribute to performance that is lower than expected. These are:

1. **Crystal imperfection**. This includes impurities or other defects that mean the lattice constant does not have the required degree of homogeneity over the length of the crystal.
2. **Strain due to the mounting scheme**. Strain effects associated with gluing or clamping of the dispersive elements crystals, or indeed even the way the angle of W is tuned relative to C via the weak links driven by the pico-motor (see Figure 12.4.4), could contribute to broadening of the Bragg reflections and hence worsening of the energy resolution.
3. **Strain effects due to crystal shape**. Particularly for the C/W combination crystal, there are many cuts close to diffraction surfaces that could introduce strain. Most obviously, the thin, 200 μm section, that allows for anomalous transmission of the beam diffracted from the collimator, C.
4. **Figure error in the surface polishing**. The required figure error for 0.1 meV resolution is less than 0.2 mrad.
5. **Temperature variation along the dispersive element**. Clearly, thermal gradients or inhomogeneities introduce lattice constant inhomogeneities that will broaden the reflections. The required temperature stability and homogeneity for 0.1 meV is 0.5 mK, which would contribute an energy broadening of 0.01 meV, well within tolerances.

Of these five possible factors, preliminary work suggests that the last of these is not important. Specifically, thermometry taken at three different places along the 175 mm dispersive crystal showed a total variation on the order of 4 mK, which would correspond to an energy broadening of 0.1 meV. This is small compared to the theoretically expected value of 0.7 meV and the experimentally observed value of 2.2 meV. Further, the thermal drift was equally small (~4 mK) over 2 days. Thus, at least at the 1 meV level, thermal effects do not yet represent a limiting factor.

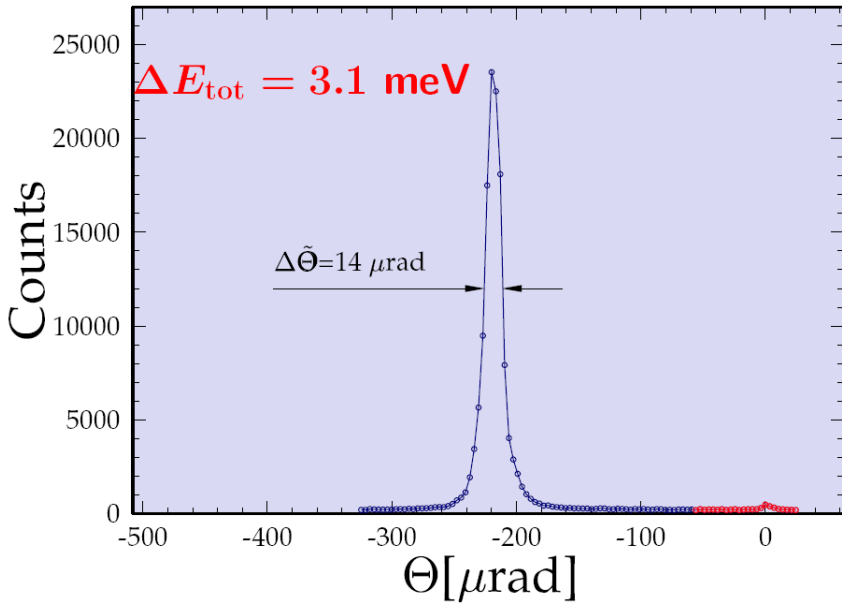

Figure 12.4.6 The effect of rocking the analyzer dispersive element through the aligned condition, with respect to the monochromator. The observed width corresponds to a total resolution of 3.1 meV, and results from the convolution of the monochromator and analyzer contributions.

The early portion of the R&D program will therefore focus on understanding the relative importance of factors 1–4. To this end, new high-purity Si has been purchased (resistivity of 50 kΩcm compared to the 1 kΩcm used in the experiment described above). This will be used as starting material for new crystals to be cut and polished with the required tolerances on "miscut" (<1 mrad) and surface figure error (<0.2 mrad). (Here, *miscut* refers to any deviation from the required asymmetry.) This work will be done at PTB, Germany. With these new crystals in hand, work first will be carried out to demonstrate theoretical performance in the existing temperature ovens. This work will include detailed high-resolution topographical studies of the crystals, both ex situ and in situ to understand any residual strain effects. Once the required performance has

been demonstrated in a pair of crystals, attention will be turned to solving the technical challenges associated with producing a working user instrument operating at 0.1 meV energy resolution based on these principles.

The technical challenges may be divided into four general areas.

1. **Crystal fabrication**. As discussed, it will be necessary to fabricate and mount large, strain-free, high-purity Si crystals. These will be 200 to 300 mm long with <1mrad miscut, and polished to a slope error of <0.2 mrad. In addition, the C/W crystal will be 80 mm long and require a 200 μm thin section, also with <1 mrad miscut. These challenges will be met as part of the initial phase of the R&D program.
2. **Temperature control**. As discussed, this is not believed to be a limiting factor in the current setup, but it will be a challenge to reach the 0.5 mK temperature homogeneity and stability required to reach 0.1 meV energy resolution. This is largely an engineering challenge, but it will require careful design and (probably) prototyping. As outlined in Section 11.5, it is presently envisaged that the analyzer will be broken into segments so that the temperature requirements need only be met over a 200 to 300 mm length, rather than a 2 m length, and a modular approach may be taken to temperature control. Nevertheless, it is clear that this will be one of the challenges associated with this instrument.
3. **Multi-crystal alignment**. The segmented analyzer crystals (up to 10 crystals in the final instrument) must be aligned to within 50 μrad of each other. Again, this is "only" an engineering and design challenge—and certainly there are rotational stages capable of these accuracies at these loads. Nevertheless, achieving this accuracy and maintaining it as the detector arm is rotated, for example, is a non-trivial matter that will require careful development work.
4. **Collimating optics**. Achieving the desired collection solid angle for the analyzer, discussed in Section 11.5 (namely, on the order of 5 to 10 $mrad^2$) will require special collimating optics capable of producing a collimated beam with a divergence of less than 50 μrad. There are a number of possible choices for such an optic, including graded multilayers. However, the design and fabrication work for this will likely be carried out by a vendor and not as part of the R&D program outlined here.

A final component of the R&D program will be the dynamical theory calculations simulating the performance of the monochromator and analyzer. These calculations will not only provide a basis against which to judge measured performance of these optics (including throughput, resolution, and lineshape), but will also allow us to assess sensitivity to various errors in fabrication and implementation, including those discussed here.

References

[12.4.1] Y. Shvy'ko, "X-ray Optics' High-Energy Resolution Applications," Springer Series in Optical Sciences, **89** (2004).

[12.4.2] Yu. Shvyd'ko, M. Lerche, U. Kuetgens, H. D. Rueter, A. Alatas, J. Zhao, "X-ray Bragg diffraction in asymmetric backscattering geometry," *Phys. Rev. Lett.* **97** 235502(2006).

[12.4.3] Yu. Shvyd'ko, U. Kuetgens, H. D. Rueter, M. Lerche, A. Alatas, J. Zhao, "Progress in the Development of New Optics for Very High Resolution Inelastic X-Ray Scattering Spectroscopy," AIP Conf. Proceedings Series, CP 879 (2006).

12.5 Metrology and Reflective Optics

Each new advance in SR source design has driven improvements in beamline optical components and associated metrology instrumentation and techniques. For example, prior to the commissioning of the NSLS x-ray ring early in the 1980s, cylindrical mirrors with RMS slope errors of 2 arcsec (10 μrad) were considered to be of excellent quality, capable of producing focal spots of several tens of microns in a typical soft x-ray beamline. The original NSLS x-ray mirror specifications in the early 1980s called for cylinder mirrors with slope errors of <1 arcsec (5 μrad). Mirrors of this quality could produce focal spots smaller than 10 μm, which was a great advance in the state of the art. Upgrades to NSLS in the 1990s and the advent of third-generation storage rings, such as APS at Argonne National Lab, significantly reduced the size of the electron beam source, enabling focal spot sizes in the range of 1 μm, with mirrors having slope errors of <1 μrad. Such mirror specifications are now routine for beamline optics. NSLS-II represents another leap in synchrotron performance, and a corresponding leap is therefore required of SR mirror fabricators and metrology developers to provide optics with slope errors on the order of 100 nrad.

Reflective optics will be used for many purposes in NSLS-II beamlines. The most widely used application will be for producing micron and sub-micron focal spots with a KB mirror pair. These mirrors will probably be made as long elliptical cylinders, up to 1 m in length, possibly as fixed or adaptive bent optics. Plane mirrors will be used as wavelength filters and first mirror power absorbers. There will be spherical collimating mirrors, grating for spherical grating monochromators, multilayer-coated bent cylinders for high-energy focusing, paraboloids, ellipsoids, toroids, etc. All of these mirrors will need to be produced with surface figure and finish tolerances significantly better than today's standards in order to make full use of the extremely small NSLS-II beam emittance. Excess surface slope error will degrade the performance of the beamline and make the ultimate performance unachievable.

The old optician's quip "If you can't measure it, I can make it," attributed to Norm Brown of LLNL, is absolutely true when mirrors are required that exceed the state of the art in both fabrication and metrology technology. When NSLS beamlines were first constructed 25 years ago, optical metrology techniques for measuring the figure of grazing incidence cylindrical aspheres, such as toroids and ellipsoids, did not exist or were grossly inadequate. The conventional tools that mirror fabricators used at that time to make spherical and flat surfaces, Fizeau interferometers, did not work well for nonspherical x-ray optics surfaces. Recognizing the need to improve metrology instrumentation capabilities for grazing incidence optics, BNL established the Optical Metrology Laboratory for the development of instrumentation and techniques that would allow one to easily characterize the finish and figure on aspheric optics. The success of the OML program has been demonstrated by the gradual improvement of SR optics over the years, enabling the mirror fabricators to keep up with advances in the quality of the storage ring beams. The Long Trace Profiler (Figure 12.5.1), developed at BNL, is now the de facto standard for SR mirror metrology at most large synchrotron facilities around the world. The current commercial version, the LTP V, has evolved over the past 15 years with improvements in optical and mechanical design, enabling measurements with accuracy at the 0.5 μrad level on meter-long mirrors. To achieve the next milestone—100 nrad accuracy—will require a multi-pronged approach to improvements in metrology instrumentation development and mirror fabrication technology.

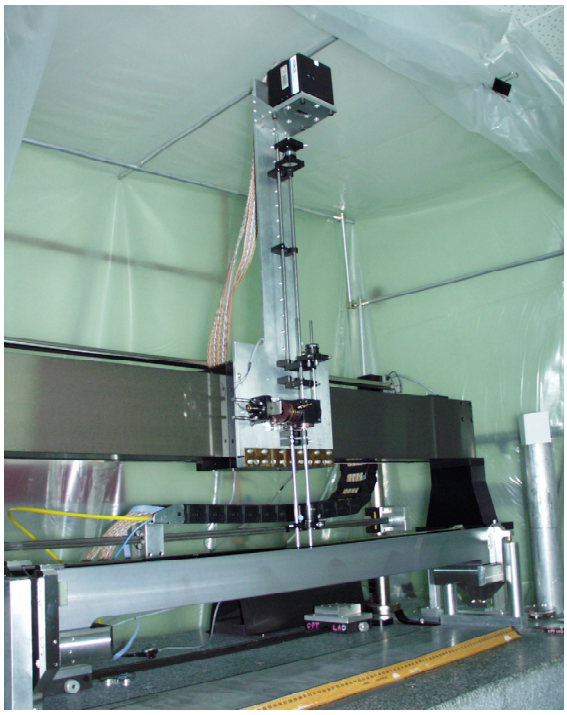

Figure 12.5.1 The current version of the Long Trace Profiler (LTP III) in the Optical Metrology Laboratory at BNL.

12.5.1 Challenges in NSLS-II Mirror Development

From experience over the past 20 years in dealing with various mirror fabricators, it is clear that one cannot expect vendors to develop dedicated metrology for fabricating SR optics at their own expense. This is especially true for small vendors with limited resources. Even for large vendors, the SR mirror market is quite small, and profit margins are not large enough to allow them to spend the resources to develop the proper metrology. Small vendors usually have customized measurement setups that are specific to the part being manufactured. We, as end users, must have a versatile measurement capability that can handle a large variety of optical component parameters. We need to have the metrology to ensure that the delivered optics meet the specified requirements. In the case of NSLS-II optics, we need to have the metrology to ensure that mirror surface slope errors are within 100 nrad of the desired shape and that figure errors are in the nanometer height range over the full length of the surface. We also need to ensure that surface roughness does not exceed a value, typically a few Å, that would cause excessive light to be scattered out of the core of the image. The goals of the reflective optics R&D program are:

- to develop the necessary metrology instrumentation to enable 100 nrad slope error and nanometer figure measurement accuracy
- to provide the manufacturer with the feedback needed so that he can adjust his process and improve the product delivered to us
- to assess the ability of new polishing methods to provide optics with the required surface accuracy

To achieve these goals we have identified five research tasks, the first three as near-term tasks to be initiated immediately and the last two as later-term tasks. The later-term tasks provide metrology capabilities at operating beamlines, while the near-term tasks deal with laboratory R&D issues needed for successful beamline development. These tasks include:

1. development of a next-generation Long Trace Profiler for accurate 100 nrad slope error measurements
2. development of a stitching interferometer system for high spatial resolution measurement of surface topography over the complete 2D surface area
3. evaluation of new polishing technologies for producing KB mirrors, in particular, magnetorheological finishing (MRF) technology that has been developed by QED Technologies in Rochester, NY
4. development of an at-wavelength wavefront metrology capability
5. development of an in-situ LTP for beamline diagnostics

12.5.2 Next-Generation Long Trace Profiler

The current Long Trace Profiler in the Optical Metrology Laboratory, the LTP III, is limited by systematic errors to an accuracy of 1 μrad. The commercial version of the instrument, the LTP V, manufactured by Ocean Optics, Inc. under license from BNL, incorporates a number of improved features and is capable of ~0.5 μrad accuracy. The source of systematic errors in both instruments has been traced to phase shifts in the laser probe beam produced by sub-nanometer surface roughness, and index inhomogeneity in the glass components with spatial period components in the range of 0.1 to 1 mm. In particular, the polarizing beamsplitter cube and the folding mirror flats are the major error sources. In order to increase the accuracy of LTP measurements beyond current state of the art, the quality of the internal glass components needs to be significantly improved. The current glass components are of commercial quality. We will need to have custom components made to extremely tight tolerances.

As with full-size SR mirrors, it is not sufficient to simply place an order for a glass component and expect it to meet the stringent surface and wavefront error specifications. We need to have the instrumentation available to perform the necessary metrology on the components ourselves. Transmitted and reflected wavefront errors are best measured with a conventional Phase-Measuring Interferometer. Recent advancements in commercial PMI technology have made available interferometers based on wavelength modulation phase shifting. For example, the Zygo Verifire MST 633 interferometer can separate the wavefront errors produced by the front and back surfaces of the glass from the glass thickness inhomogeneity errors. Acquisition of this type of interferometer will allow us to reduce the systematic error introduced by these glass components.

Other improvements are necessary to increase the reliability and repeatability of the LTP in the Optical Metrology Laboratory. The present aluminum air bearing translation stage in the OML needs to be replaced with a high-precision ceramic beam. The ceramic air bearing stages that are used in the commercial version of the LTP II have total slope errors on the order of 1 arcsec over the 1 to 2 m travel length. The current OML LTP translation stage has a slope error of ~20 arcsec. Reducing the magnitude of this large translation stage error signal will reduce the fraction of the error signal that leaks into the measured surface profile.

Further, improvements to the detector and control system will result in a more fully automated measurement system, requiring less operator intervention and consequent environmental perturbation of the measurement envelope. Use of a 2D camera instead of a 1D line scan camera will result in a more versatile system.

12.5.3 Stitching Metrology Development

The Osaka University group at the Center for Atomistic Fabrication Technology has demonstrated the necessity of measuring surface figure errors on KB mirrors down to 50 μm spatial periods, in order to produce nearly diffraction-limited nanofocusing optics. The elliptical cylinder shape precludes the use of a conventional PMI as the sole measuring tool. There is no single metrology instrument that can encompass the spatial period range from 0.5 m to 50 μm. The Osaka University group has shown that it is necessary to use stitching interferometry to extend the range of a micro-PMI into the long period region. This has enabled them to produce nearly diffraction-limited KB mirrors by elastic emission machining and plasma chemical

vapor machining, two of the several surface finishing technologies that have been developed at their laboratory over the past 20 years.

We will need to develop a sub-aperture stitching interferometry capability tailored to the types of optics that we anticipate will be used in NSLS-II beamlines. The Osaka system is optimized for 200 mm long mirrors. We will need to extend the range up to 1 m. To do this, we will likely combine a dedicated LTP optical head with a micro-PMI instrument, probably a Zygo NewView system that is normally used for surface roughness measurement. Both instruments will be mounted together on a scanning air bearing stage. A similar system has been developed by Zygo and QED Technologies for Canon in Japan. First results from the Canon Mid Spatial Frequency metrology tool were reported at the OSA OF&T workshop in Rochester earlier in October 2006 by M. Ohtsuka. The Canon system is optimized for spherical aperture optics and does not incorporate a scanning linear stage, but QED is confident that their stitching algorithm can be applied to the scanning head system. One of the unique features of the Canon system is the special Zygo NewView NV-R Optical Surface Profiler measurement head that is used to make the sub-aperture measurements. The internal optics are customized to optimize the instrument transfer function to provide more reliable data at high spatial frequencies. The improvement factor for the 20X objective is shown in Figure 12.5.2.

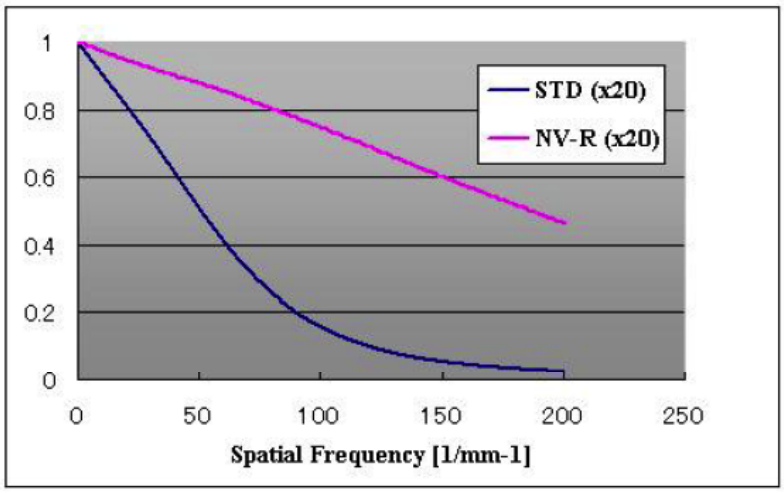

Figure 12.5.2 Improvement in frequency response of the Zygo NewView NV-R optical head used in the Canon lithography optics measurement system. Customized optical components replace standard components in this system.

Source: M. Othsuka, presented at OSA OF&T Topical Meeting, Rochester, NY, Oct. 2006

We will work with Zygo and QED to develop a stitching metrology instrument that incorporates the improved NV-R optical head and utilizes the QED stitching software algorithm. The hardware design and acquisition for this project should take about two years, and the assembly, installation, and commissioning should take another year.

12.5.4 Polishing Technology R&D

The recent developments by Osaka University in producing extremely smooth surfaces with nanometer figure errors are the result of more than 20 years of research into polishing technology, funded mainly by the Japanese semiconductor industry with the backing of the Japanese government. The KB mirrors produced by Osaka for SPring-8 hold the world record for smallest x-ray spot size. Only recently have the Japanese made these mirrors available outside of Japan through a local export company, but this company has not yet delivered any mirrors. The EEM process is so complex that it can only be done with the dedicated machine at Osaka University. The typical time required to polish a KB mirror with this process is 2 to 3 months. We need to explore other avenues for producing elliptically figured cylinder mirrors by other polishing techniques.

Magnetorheological finishing is a promising technique for producing mirrors with the required figure accuracy. MRF has been developed by QED Technologies as spinoff from work done at the Center for Optics Machining at the University of Rochester over the past decade. The MRF process utilizes a strong magnetic

field to change a liquid fluid stream into a relatively hard viscous stream in the vicinity of the workpiece. The MRF fluid carries a polishing compound that polishes the surface. Coupled with high-resolution metrology, the process converges rapidly to correct surface figure errors and produces extremely accurate surfaces, both spheres and aspheres. There is, however, a question about excess residual roughness remaining on the surface that may be an intrinsic property of the polishing process.

We are investigating establishing a collaboration with QED to explore the feasibility of the MRF process to produce KB mirrors suitable for use at NSLS-II beamlines. This is a three-part project. First, QED would demonstrate that they can produce a super-polished Si flat with nanometer figure error. This may involve fine-tuning the chemistry of the MRF fluid to lower the removal rate, since the Osaka work has shown that low removal rates are correlated with smoother surfaces. Second, QED would produce KB elliptical cylinders that will be evaluated at an NSLS or APS beamline. Third, QED would develop a sub-aperture stitching interferometry algorithm for producing long and narrow non-rotationally symmetric parts. This is a significant departure from the typical case of a small rotationally symmetric part, where the stitching algorithm contains a self-consistency check from closure. There is no closure with a rectangular grid-scanning algorithm. The sub-aperture stitching interferometry algorithm will be usable in our stitching interferometer so that we can perform our own metrology check on the delivered optics. If we pursue this effort and QED is successful in developing a polishing process that can produce nanometer quality optics for KB mirrors, they will transfer this technology to the many vendors who have QED polishing machines. We would then have a choice of vendors for custom KB mirrors. The resulting competition should act to produce a source of high-quality mirrors at reasonable cost.

12.5.6 At-Wavelength Metrology

A powerful topographic diagnostic technique for x-ray wavefront diagnostics, developed by Souvorov at SPring-8 and based on the phase retrieval algorithms of Jim Fienup at the University of Rochester, utilizes the information in interference patterns produced by coherent x-rays as seen at various distances downstream from an optical element that interacts with the incident beam. Souvorov has demonstrated that the topography of extremely smooth surface profiles of substrates polished by EEM at Osaka can be reconstructed with Å-level repeatability with this technique [12.5.1]. This wavefront reconstruction technique provides information about how the surface interacts with the x-ray beam under actual operating conditions at the actual operating wavelength. This measurement capability is invaluable for performing diagnostics on optical elements that cannot be characterized with surface profiling instruments at visible wavelengths. Examples of such components are kinoform refractive optics, zone plates, Bragg-Fresnel optics, and multilayer coated surfaces. An at-wavelength measurement technique for these kinds of optical elements is essential for assessing the quality of the fabrication process.

Developing this metrology technique here at BNL would require establishing a beamline for testing optics on NSLS-II. Such a beamline is very briefly discussed in Chapter 11. Initial work would need to be done in the two or three years prior to the start of beamline commissioning so that the methods and techniques would be in place as soon as coherent flux is available at the startup of the machine. The principal equipment needed for this measurement is a high-resolution image converter camera with 0.5 μm spatial resolution. Initial setup work could be done on an existing NSLS beamline and moved over to NSLS-II as soon as coherent photons are available. Other at-wavelength wavefront metrology techniques can also be explored. In particular, Talbot grating imaging, developed by T. Weitkamp at the Paul Scherrer Institute, is a potential candidate for x-ray wavefront distortion measurement. It requires the fabrication of grating structures with micron periods and very high aspect ratios for efficiency at high energies. These gratings can be fabricated by the facilities that will be available at the Center for Functional Nanomaterials. This measurement technique also has applications in imaging weakly absorbing biological structures [12.5.2].

A dedicated beamline for testing optics will have many uses, only a few of which are enumerated here. Other uses include testing multilayer coating uniformity by reflectometry and performing photometric calibration of various detectors.

12.5.7 In-Situ LTP Development

The original In Situ LTP measurements were performed at ELETTRA in 1996 [12.5.3]. Subsequent ISLTP measurements were made on a high heat load mirror at APS that showed significant transient distortion effects when the beam shutter was opened, showed the location of the 100 nm high thermal bump when the slits were nearly closed, and showed an unexplained residual curvature distortion when steady state equilibrium was reached after 15 minutes [12.5.4]. These measurements demonstrated the usefulness of in-situsurface slope error measurement as a diagnostic aid and alignment tool for positioning mirrors in the center of an x-ray beam. We have been developing improved versions of a compact LTP optical system that is easily portable and that can be set up at a beamline to monitor changes in the shape of a mirror in real time.

To take full advantage of the diagnostic capabilities afforded by the ISLTP, it is necessary to design the appropriate view ports into a particular mirror chamber or monochromator and to make provisions for mounting the ISLTP. These tasks should be performed during the design of the actual beamline hardware.

References

[12.5.1] A. Souvorov et al., *J. Sync. Rad.* **9**, p. 223-228 (2002).
[12.5.2] T. Weitkamp et al., *Opt. Exp.* **13** (16) p. 6296-6304 (2005).
[12.5.3] Qian et al., Proc SPIE **2856**, p 172-182 (1996).
[12.5.4] P.Z. Takacs et al., Proc. SPIE 3447, pp. 117-124 (1998).

12.6 Advanced Detectors

12.6.1 Detector Requirements and Challenges

Advanced detector systems will be required to take full advantage of NSLS-II's superlative performance. For a synchrotron experiment, the detector system is an especially critical component that often enables new science. One outstanding example is that of macromolecular crystallography. When the only viable area detector capable of quantitative interpretation was film, macromolecular crystallography was an esoteric pursuit, involving an exorbitant amount of labor to wet-process thousands of films for each experiment. The availability of synchrotron radiation sources made little impact. The development of new, large-area electronic detectors has transformed macromolecular crystallography into a high-throughput research powerhouse, providing key knowledge for the understanding of disease mechanisms and drug design.

In general, it is clear that the trend is toward higher levels of functionality integrated into the detector elements and readout systems. This will include digital signal processing of the analog sensor output as well as digital post-processing of events. These trends are already visible in the high energy physics field, and are beginning to be seen in synchrotron radiation systems. We can expect that pulse height histogramming, time and space correlations, and spectral corrections will all be integrated at the chip level in future detectors.

Conventional computing resources are also beginning to be embedded in more Application-Specific Integrated Circuits, ASICs. At least one programmable gate-array device manufacturer is selling a product with up to four PowerPC processors embedded in the center of a large programmable gate array. In the next years leading to NSLS-II, even more powerful devices can be expected. It is now almost as easy to embed a CPU into an ASIC as it is to include a subroutine in a software program. Modern simulation programs can

accurately simulate the performance of a complete ASIC before manufacture, giving a high degree of confidence that the final device will work as specified.

More sophisticated devices will inevitably lead to increased data capture rates. This is already a limitation for existing detectors, particularly those that deal with images. Add to the large pixel count, the need for energy spectra and/or time-correlation spectra per pixel, plus the need for tomographic information, and dataset sizes can easily expand to terabytes. It is not yet clear how to handle the gigabyte/second data rates expected from the next generation of area detectors, so these more sophisticated devices will need real innovation in data movement technology, or a great deal more customizing of readout systems to reduce data in real time, probably using the embedded intelligence described above.

At NSLS-II, the R&D program for detectors will be driven by the needs of the users for specific detectors. Here, we outline three examples of particular areas of challenge—imaging, spectroscopy, and high-spatial resolution detectors—and the R&D program that would be required to meet these challenges with next-generation detectors. The precise details of the actual R&D program will be determined in accordance with the requirements of the beamlines.

12.6.1.1 Imaging Challenges

Current detectors suitable for acquiring single-crystal and powder diffraction images are rather slow, with readout times of a second or more. This characteristic of 2D position-sensitive detectors is receiving significant attention, due to the large ready market offered by macromolecular crystallography. The Swiss Light Source has recently completed a silicon-based pixellated detector for this application, and it will soon be commercially available. At least one vendor has an independent but similar development underway. There are also detector R&D programs underway in support of Stanford's Linear Coherent Light Source x-ray free-electron laser project, and a program will soon begin in support of the European XFEL project. Consequently, an NSLS-II effort on the development of an imaging detector is not contemplated.

What has not been addressed by any developers so far is the problem of rapidly recording images with time-correlation. Time-correlation spectroscopy is a new technique showing great promise in the field of low-energy excitations in solids and liquids, such as thermal diffusion and critical phenomena. These experiments will be greatly improved by the high brightness of NSLS-II. However, the range of excitation energies accessible to the technique is determined by the time resolution of the detector. For a single-point detector, this can be on the nanosecond scale. Experimenters would like to sample a wide range of momentum transfer (i.e., length scales), so an area detector would be advantageous. Time resolution then translates into the readout speed of the detector. Of course, if each pixel of an area detector were read out photon-by-photon, then the time resolution would be limited by charge collection physics (typically hundreds of nanoseconds). Compared to the full-frame readout of a CCD, this is very fast. The events in each pixel need to be independently recorded in some way. One approach is to design a detector with an autocorrellator on each pixel. That possibility should be explored, making use of continuous increases in microelectronics density and using logarithmic variable time domain techniques to cover a wide range of time correlations in a relatively small footprint.

12.6.1.2 Spectroscopy Challenges

Pixel detectors equipped with energy-resolving capability will require the ability to put a complete energy-histogramming subsystem on each pixel of a large array. Such detectors will be the logical extension of devices currently reaching the experimental floor, which have hundreds of pixels, each with a complete signal-processing chain. These systems were designed for fluorescence detection in absorption spectroscopy experiments with dilute samples, where the experiment feasibility is dominated by the presence of a high parasitic flux of uninteresting radiation. This results in premature saturation of the detector chain, enforcing long acquisition times and eventually preventing a successful experiment. This situation will be worse with NSLS-II, and so we must plan for remedies. Increasing the parallelism even further is one way forward, and

on-chip intelligence to deconvolve acquired spectra on a photon-by-photon basis will be a significant enhancement, bringing improved separation between the desired and parasitic radiation. One could also imagine such a detector bringing a new lease of life to the Laue diffraction technique, since it becomes much simpler to perform the necessary diffracted intensity corrections if one knows the energy of the photon directly. This same knowledge also helps in indexing such Laue patterns, and removes the problem of harmonic overlap. Nevertheless, fabrication of such a detector is no simple undertaking. A high-speed ADC is power-hungry, and one would need on the order of 1 million of them for a reasonably sized detector. As CMOS technology continues to shrink, this will eventually be possible, at least for pixels of dimension 100 micrometers or more. Applications of such a detector might be in microbeam grain-mapping of polycrystalline materials, or high-pressure diffraction experiments. Such studies are important to provide a firmer basis for understanding the properties of real materials on all scales, and are ideally suited to a machine like NSLS-II.

12.6.1.3 Other Applications

Some of the highest demand from materials scientists is for polycrystalline diffraction—in particular, the type of instrument that uses a crystal analyzer to achieve very high angular resolution. Unfortunately, such instruments are intrinsically slow, since a large angular range must be scanned point-by-point with small angular steps. At NSLS, we have demonstrated a new instrumental arrangement that provides such high resolution without scanning, based instead on a focusing technique and using a high-resolution, high-speed linear position-sensitive detector. This detector is based on our silicon microstrip technology, and could easily speed up such data acquisition by a factor of 1,000. This would open up the field of time-resolved high resolution polycrystalline diffraction for the first time. This instrument could easily be combined with one of the high-rate spectroscopy detectors discussed above, to make a very powerful combined-function microprobe.

12.6.2 Infrastructure and Technologies

12.6.2.1 Sensor Fabrication and Novel Sensor Development

To develop the advanced detectors such as those described above, new technologies will be needed. The first requirement is the ability to produce complex, low-noise circuitry that is monolithic with the high-resistivity silicon detector element. Commercial foundries and processes do not routinely use high-resistivity silicon material, so processing it requires either a special agreement with a commercial foundry, or an in-house facility. Although BNL has a modest foundry for the production of simple sensor diodes, it is not adequate for a program to develop the new devices discussed above. However, there is significant in-house expertise in device design, both at the sensor level and at the integrated circuitry level. This BNL-based team is internationally recognized as among the leaders in the ionizing radiation detector field, having a long and successful track record.

The cost of establishing a foundry to provide the required capabilities at BNL is prohibitive, so we have begun discussions with IBM Research, based in Yorktown Heights, NY, on a collaboration to try to adapt standard foundry processes to our needs. These exploratory discussions are currently in the context of detector development for Stanford's LCLS, but the technology to be developed will be fully applicable to NSLS-II detectors. This approach requires a much smaller capital investment.

12.6.2.2 CAD Tools

The development of any electronic device at the chip level relies heavily on computer-aided design and engineering tools to handle the large and complex manipulations required. At the basic level, electric field profiles must be modeled within the volume of the silicon itself, a region in which the electrical properties of

the silicon varies on the nanometer length scale by orders of magnitude, and are not known from first principles. At a higher level, integrated components are formed by selective doping of areas of silicon through masks. The dimensions of these selected areas are sub micron, and are controlled by complex geometric rules, obtained through much R&D in device fabrication labs. The only way to perform such graphical manipulations efficiently is by liberal use of computers. Since these tools are the basis of the largest industrial enterprise in the world, they are sophisticated and expensive.

BNL has been involved in custom integrated circuit design for many years. The readout of signals from pixelated solid state sensors requires the use of such dedicated monolithic front-end electronics (i.e., ASICs) if the detector performance is to be optimal. Front-end ASICs can provide low-noise amplification, filtering, signal processing, efficient derandomization, sparsification, storage, and multiplexing of the signals from the individual segments of the sensors. Highly specialized ASICs were originally developed mainly as analog circuits, but the complexity and amount of digital circuitry has rapidly increased. For example, in the 10+ years that BNL has been developing state-of-the-art front-end ASICs, the transistor count grew from about 1,000 per ASIC to more than 600,000 per ASIC in 2005.

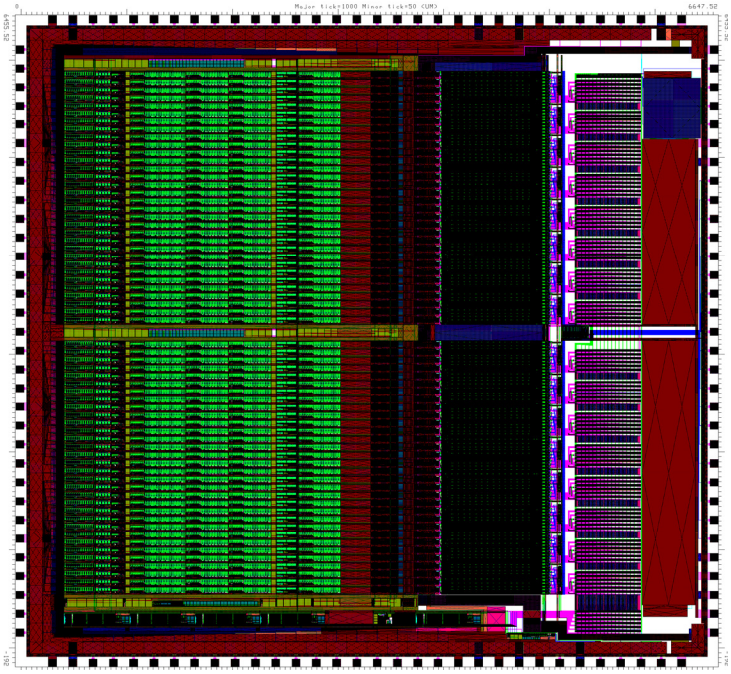

Figure 12.6.1 Layout of a 64-channel ASIC for high-rate counting with multiple energy discrimination. Size 6.65×6.65 mm², transistor count 601,000, layout tool MAGIC, design tool Capture/PSpice.

The development of a front-end ASIC starts from a conceptual diagram and proceeds with transistor-level design, advanced and extensive simulation, conversion of the schematics into a specialized layout, verification of the layout and parasitics extraction, and further iterations through the design and layout phases as needed. Once the layout is ready, the ASIC can be fabricated, in most cases using commercial foundries. The ASIC prototype, once fabricated, is thoroughly characterized without and with the sensors and, if needed, it undergoes more (typically one or two) additional review cycles of design and fabrication. Developing an ASIC requires, for each design phase, the use of specialized computer-aided design tools. The CAD tools currently adopted by the BNL ASIC design group have reached the limits of their capabilities.

As we progress to detectors which have such microcircuits directly integrated with the sensor, all of these CAD tools become necessary from the start, since we have effectively combined the sensor and front-end ASIC into a single monolithic structure. The following CAD tools will be acquired:

- analog and mixed signal transistor level design and simulation: Cadence Virtuoso Schematic Editor and Cadence Virtuoso AMS
- analog and mixed signal layout generation: Cadence Virtuoso Layout Editor

- layout extraction and layout vs. schematics comparison: Cadence Assura

12.6.2.3 Readout Electronics

Some form of electronic subsystem is required to take the signals from the detector and deliver them to the data acquisition system. This is conventional electronics, typically printed circuit boards in surface-mount technology, plus some mechanical enclosure.

12.6.2.4 Beamline Integration and Data Acquisition

It is extremely important that any detector be integrated into the user experiment through appropriate and adequate software. Since the NSLS-II control system will be EPICS-based, it is expected that all detectors will also conform to that standard, minimizing the amount of custom software necessary for this integration. Software to implement the scientific aims of the experiment is not considered in this section, but this should not be taken as minimizing its importance.

12.6.3 Detectors Needed for Proposed Beamlines

A range of standard, commercially available detectors will be useful for NSLS-II beamlines, but we do not discuss them here. They will be discussed in the description of each beamline. In addition to these currently available devices, the following are examples of new types that will be required. These, or other similar detectors, may be developed through focused efforts driven by specific needs identified by the scientific case and technical requirements for the beamlines constructed at NSLS-II.

- massively parallel Silicon Drift-Detector array for microprobe / fluorescence holography
- “speckle” detector with autocorellator
- large angular coverage silicon microstrip detector for polycrystalline diffraction

12.7 Insertion Devices

In Chapter 8 we specified the types of insertion devices that are needed to meet user requirements and to achieve the unprecedented brightness goals of NSLS-II. We presented the optical performance and spectral characteristics of these IDs. They are based on proven designs, and in some cases push the state of the art in what we believe to be rational and realizable extensions of existing technology. In this section we present conceptual magnetic designs of the various ID types that will meet the performance requirements and constraints. We also identify and describe the R&D and prototyping needed to verify each design concept, to resolve any unknowns, and to test advanced concepts for future upgrade paths. We describe novel mechanical concepts that may simplify ID designs and/or improve their performance. Finally, we describe magnetic measurement systems that will be developed to verify and optimize ID performance.

12.7.1 Tunable Hard X-ray Sources

A decade ago, the hard x-ray region of the spectrum by undulators could only be covered at high-energy machines, such as ESRF, APS, and SPring-8. The advent of a mini-gap, short-period in-vacuum undulator, dubbed IVUN, [12.7.1] in 1997 at the National Synchrotron Light Source has had a lasting impact on the design of synchrotron light source facilities all over the world. With the use of mini-gap, short-period undulators, a medium-energy ring (~3 GeV) can now produce tunable hard x-rays between 2 keV and 20 keV. Many years of successful operation of IVUs at SPring-8 [12.7.2], NSLS, and, more recently, at SLS and ESRF have demonstrated the reliability of IVUs. The NSLS currently has three IVUs in operation.

A long-standing concern in the ID community has been that the permanent magnets in small-gap IVUs would be gradually demagnetized and degraded by radiation, due to their proximity to the electron beam and exposure to synchrotron radiation. The conservative approach has been to use Sm_2Co_{17} magnets, rather than the higher field NdFeB magnets, because its lack of boron ought to make Sm_2Co_{17} more radiation resistant. However, after many years of successful operation at SPring-8, NSLS, and SLS without any signs of demagnetization, NdFeB IVUs with proper magnets have proven to be quite radiation resistant. The newest high-remanence, high H_{cj} grades of NdFeB (such as NEOMAX AH series), developed for use in hybrid car motors, should be particularly robust and radiation resistant. We have used this high-temperature NdFeB in our most recent IVU and have based our PM ID designs for NSLS-II on this same magnet material.

Curiously, some out-of-vacuum undulators at APS have experienced localized demagnetization, particularly those with smaller aperture vacuum chambers. Detailed simulations and radiation measurements suggest that the main source of the demagnetizing radiation is the tapered part of the aluminum vacuum chamber itself. Thus, out-of-vacuum IDs, such as the elliptically polarized undulators, may be more vulnerable to demagnetization than IVUs. Another contributing factor may be that the magnet grade used in APS undulators does not have particularly high H_{cj} and therefore does not withstand even localized radiation-induced head.

Advantages of IVUs over fixed-chamber, out-of-vacuum IDs are 1) that the former can be opened to provide a wide aperture during machine commissioning or beam studies, and 2) the lack of neutron-producing materials at transitions would mitigate magnet demagnetization.

A subject that needs further study is the impedance of the variable-gap IVUs. In Chapter 6, it was shown that the H-shaped space created by the gap space and the chamber forms a waveguide that contributes to transverse impedance. The RF transitions at the extremities of an ID must be properly tapered to reduce the geometric impedance. Modeling and RF measurements of real IVUs will be part of the R&D effort.

12.7.1.1 Cryo-Permanent Magnet Undulator

Recently the Cryo-Permanent Magnet Undulator (CPMU) has been proposed [12.7.3], as a simple means to enhance the performance of permanent magnet IVUs. The baseline design for a hard x-ray undulator for NSLS-II is based on a short-period linear undulator of the CPMU type. This is the U19 device described in Chapter 8.

The enhancement is based on the fact that NdFeB has a negative temperature coefficient of about –0.1%/K at 20°C for the remanent field (B_r), and also –0.5%/K for the intrinsic coercivity (H_{cj}). Therefore, one can expect higher field and higher radiation resistance simply by cooling the magnet array to lower temperature. However, NdFeB exhibits a spin orientation below somewhere around 150K and its B_r starts decreasing as the temperature goes below this value [12.7.6]. An obvious advantage of operating NdFeB at the plateau around 150K (in addition to gaining 11 to 13% higher field), is greatly reduced sensitivity of the field to temperature gradients.

To test the effect of cooling NdFeB undulators, we measured our decommissioned 0.3 m Prototype Small-Gap Undulator in dry ice at –71°C, and demonstrated that the field increased as expected at –0.1%/°C, or about 9% when cooled down by ~90°C. However, this measurement did not reach the plateau in the B_r vs. temperature that is expected at around –120°C. Analysis of the Hall probe data showed no significant increase in phase error, or in trajectory error, except in the end terminations. We also measured a 10-pole 13.5 mm period PM-hybrid prototype in dry ice with similar results.

The SPring-8 group recently compared warm and cold (130K) measurements of a 1 m long pure-permanent-magnet CPMU. They found that while the fields increased as expected, magnetic field errors scaled and tracked with temperature as well. This suggests that a CPMU can be shimmed at room temperature, and it will remain optimized when it is cooled. This also supports the notion that a CPMU is inherently “fail-safe,” in that it will still work well, albeit over a reduced tuning range, even if the cryocooling

fails. If this result holds true for a hybrid CPMU, we will save an enormous amount of time in the magnetic shimming and spectral optimization of CPMUs by avoiding multiple cool-downs and warm-ups during the iterative shimming process. An important R&D task will be to verify by cold and warm measurements that field errors track with temperature in a hybrid CPMU as well.

12.7.1.2 "Cryo-Ready" MGU Installed in NSLS

NSLS has recently constructed and installed a 1 m long "cryo-ready" MGU for beamline X25 (18 mm period, B_y = 0.95 T at 5.6 mm gap) [12.7.7]. It has provision for cryogenic cooling by circulating cold He gas from a refrigerator through channels embedded in the magnet array platens. For the test we were able to cool it to 130K by circulating boil-off N_2 gas. This test demonstrated that the mechanical features designed to accommodate the large differential thermal contraction of the cold magnet arrays relative to the warm vacuum vessel worked. We mapped the undulator before and after thermal cycling and found no measurable magnetic changes.

12.7.1.3 Optical Gap Measurement

First-order gap control is performed using four external stepper motors with a linear encoder feedback system that positions each magnet girder to a mean reproducibility of 1 micron. The 1 m magnet length required multiple structural feed-throughs in the vacuum envelope to assure continuity between rigid external structural girders and the in-vacuum magnet girders. However, magnetic and mechanical measurements indicated that gap-dependent nonlinear magnetic forces, environmental temperature gradients, and operational conditions caused deflections of the in-vacuum magnet girders exceeding specifications. The external linear encoders could not measure these effects, and correction by the primary gap control system would be ineffective. The CPMU direct measurements of the magnet gap differed by greater than 1 mm with respect to the gap, as inferred by the external linear encoders. These measurements indicated that relying exclusively on a conventional external linear encoder-based control system is insufficient under extreme conditions, and a direct means of gap measurement and a secondary means of gap control are necessary to maintain micron control of the magnet girders over the full range of environmental and operational conditions. An LED-based system (e.g., Keyence LS-7030) that has a measurement accuracy of ±2 μm and repeatability of ±0.15 μm can be employed to provide a secondary means of gap control, to permit correction over the regime of these tertiary effects for up to 100 microns of nonlinear gap control. Very fine taper/bow control can be achieved by embedding temperature-controlled heaters for each post. This method successfully worked for the X25 MGU at NSLS.

12.7.1.4 Optimizing the CPMU Design

Table 12.7.1 shows the possible combinations of period length, achievable peak field, and effective values of deflection parameter ($K_{y\,eff}$) at the undulator gap of 5 mm for warm (20ºC) and cold (–120ºC) in-vacuum devices calculated by the same Radia [12.7.8] model used for the X25 MGU. These are all hybrid structures with vanadium permendur poles. In this table, the effective K value for the non-sinusoidal field is calculated as

$$K_{x,y\,eff}^{\,2} = 2\,\langle \gamma^2 \frac{v_{x,y}^{\,2}}{c^2} \rangle , \qquad (12.7\text{-}1)$$

where c is the speed of light in vacuum, γ is the Lorentz factor, and v is the velocity of the electrons.

Table 12.7.1 Period-Length vs. Maximum Flux Density and Effective K Value for IVU at Room Temperature and 150K.

Period Length (mm)	Warm (B_r = 1.29 T) B_{peak} (T)	Warm K_{eff}	Cold (B_r = 1.45 T) B_{peak} (T)	Cold K_{eff}
16.0	0.88	1.28	0.98	1.43
17.5	1.00	1.57	1.11	1.74
19.0	1.11	1.86	1.21	2.03
20.0	1.17	2.05	1.26	2.22
21.0	1.22	2.22	1.31	2.40

All of the NSLS MGUs have severe limitations in their length. Therefore, the ideal magnetic termination at the extremities has to be compromised in order to increase the number of full-field-strength periods. Hybrid devices tend to have an inherently larger gap dependence of integrated field strength, due to the nonlinear characteristics of pole materials and anisotropy of permanent magnets. Various termination schemes that minimize the gap dependence for pure permanent magnet devices have been developed [12.7.9]. However, designs for hybrid devices have limited effectiveness. End effects tend to be less important for small-gap undulators than for large-gap, high-field wigglers.

12.7.1.5 Minimizing Phase Error

A critical requirement for short-period, in-vacuum MGUs in a medium-energy storage ring is retaining high spectral brightness, up to the 7th or even the 9th harmonic. Loss of spectral brightness is well correlated with optical phase error. Phase error can be defined as the cumulative path length difference between the electron's actual trajectory and an ideal trajectory, expressed in degrees of phase at the fundamental optical wavelength. Cumulative optical phase error of 2° RMS is considered state of the art and will be the target for all NSLS-II undulators. This is an especially challenging requirement for small-gap, short-period IDs, as shown below.

Phase error arises from three sources: 1) systematic gap error, 2) trajectory wander, and 3) random phase errors. We will next describe the techniques we have developed and use routinely to minimize phase error from these three sources.

Systematic phase error can be caused by a) bowing of the magnet arrays due to attractive magnetic forces, b) gap taper, and c) nonflatness of the magnet mounting surfaces. These are long-range gap variations, on the scale of many undulator periods, which cause a gradual variation of field amplitude, wiggle amplitude, and therefore trajectory path length, without trajectory steering. To obtain a mechanical tolerance budget for these effects in the X25 MGU, we started with a finite-element analysis of an initial mechanical design for the magnet support beams, suspended on two hangers, under a distributed magnetic load of 8,000 N (due to the peak field of I T at a 5.6 mm gap). The resulting deflection profile was scaled to a field amplitude profile, which was numerically integrated to obtain the trajectory and, finally, a cumulative phase error profile. Figure 12.7.1 is a plot of the gap error (blue) and resulting cumulative phase error (magenta) vs. longitudinal position Z. The peak-to-valley deflection of 3 microns results in a RMS phase error of 0.75°. The figure shows that two supports per meter can induce a phase error of 0.75 degrees, due to deflection resulting from B = 1 T. Solid aluminum platens are assumed in this simulation.

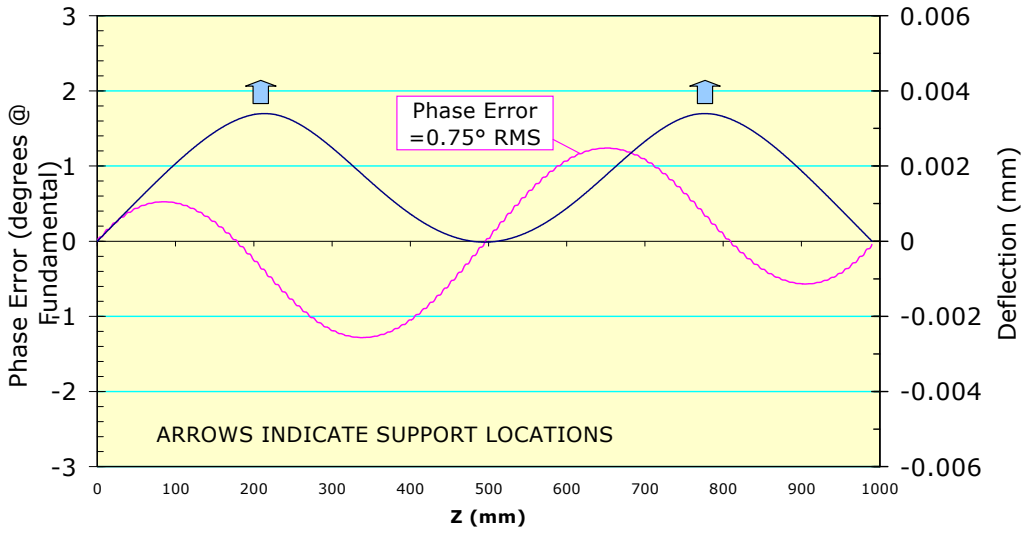

Figure 12.7.1 Phase error created by the mechanical deflection of aluminum magnet platens, due to the magnetic force of B = 1T.

The phase error created by 3.3 microns of linear tapering in 1 m is presented in Figure 12.7.2.

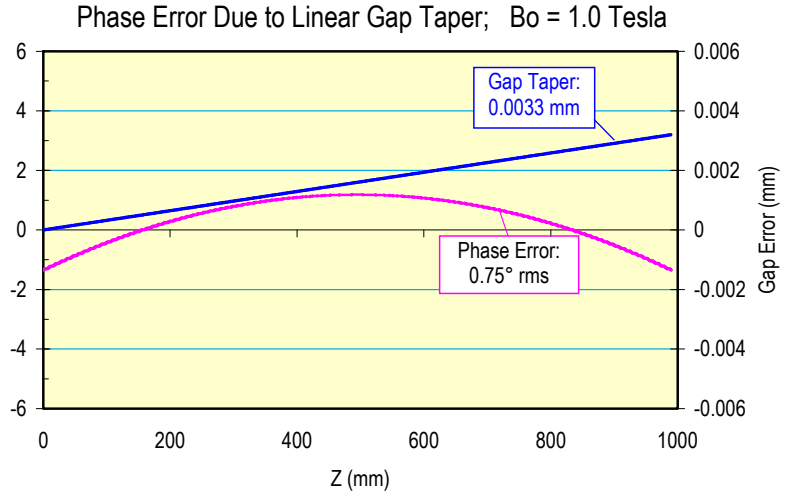

Figure 12.7.2 Phase error created by linear gap taper. B_0 = 1.0T.

Trajectory wander is caused by local, random field amplitude errors, which cause the trajectory to deviate from a straight line. The longer path is reflected in a phase error. Local steering errors can also accumulate over the length of the undulator as both integrated dipole (first integral error) and trajectory offset (second integral error). We routinely use the Pulsed Wire technique to quickly visualize the trajectory in undulators, identify the location and magnitude of steering errors, and apply steering shims to correct them. The pulsed wire easily displays both the horizontal and vertical components of a trajectory, including the contribution of the Earth's field.

Random phase errors are nonsteering errors that remain following trajectory straightening and the removal of systematic phase errors. In a PM-hybrid undulator, random phase errors are mainly caused by variations in the strength of individual magnets, as well as by pole positioning errors. To minimize these, the individual magnets are first measured, then sorted, paired, selected, and assigned to specific locations in the arrays. Various manual and computer-aided sorting and selection algorithms have been developed and are considered standard practice.

Earth's field causes significant trajectory deflection in long undulators. The measured local Earth's field is about 0.4 Gauss with an inclination of about 14° from the vertical. The vertical component contributes an

integrated (horizontally deflecting) dipole error of about 40 Gauss-cm/m. In a 3 m long CPMU, that adds up to a nontrivial dipole error of 120 Gauss-cm. The horizontal component is about 0.1 Gauss and oriented toward magnetic North. The effective (vertically deflecting) dipole error is <10 Gauss-cm/m and depends on the azimuthal orientation of the ID in the ring. The effect of Earth's field is readily visible on the pulsed wire as a parabolic trajectory component. It can be compensated by distributed trajectory shimming, or with external Helmholtz coils. In the X25 MGU we added a pair of 10-turn horizontal coils around the undulator vacuum vessel, powered by the end-pole trim supply from the old X25 wiggler previously residing at that location. Using the pulsed wire, we determined the optimal current to cancel Earth's field in the X25 MGU to be about 3.5 A. The small horizontal component was not compensated.

Other error specifications, such as maximum first and second integral and allowable integrated multipole requirements, will be specified before the engineering design phase.

12.7.1.6 Effect of Magnetic Field Errors on the Undulator Harmonics

The performance of real undulators is known to be poorer than the ideal case owing to magnetic field errors, despite valiant efforts to minimize such errors. It is generally accepted that the parameter which best relates magnetic field errors to spectral output is the RMS phase error ϕ. The RMS phase error ϕ is defined as the RMS path length difference between the real and ideal electron trajectories. It is calculated at the poles of the undulator and normalized to the wavelength of the fundamental harmonic (n = 1). (At higher harmonics (n >1), the RMS phase error is $n\phi$.) To date there has been no complete analytic treatment of the spectral effects of the phase errors. It has been argued that, for a zero-emittance electron beam, the relative on-axis brightness of the odd undulator harmonics n = 1, 3, 5, … emitted by an undulator with uncorrelated and Gaussian distributed phase errors is given by

$$B(n,\phi)/B(n,0) = e^{-n^2\phi^2} \tag{12.7-2}$$

where ϕ is the RMS phase error.

Recently, we have found empirically that this formula tends to underestimate the effect of phase errors for real undulators. For the two LCLS undulators discussed below, the expression above for a zero-emittance beam can be made to agree reasonably well with the result derived from magnetic measurements only if the RMS phase error is increased by ~20% from the measured value ($\phi \rightarrow 1.2\phi$). This is a large "correction" factor; more accurate results can be obtained by feeding the measured magnetic field profiles directly into undulator codes, such as UR or SPECTRA. Moreover, there is no analytical formula for phase error effects when the emittance needs to be taken into account, so we need to resort to numerical calculations.

Simulations were performed using measured magnetic field data from a set of undulators with RMS phase errors spanning a range from 2.0° to 3.7°. The measured magnetic field profiles and the storage ring parameters for NSLS-II were used as inputs to the undulator code UR in order to simulate realistic undulator spectral performance. If the results are a well-behaved function of phase error, one can then make a determination of the maximum tolerable RMS phase error required to achieve a particular level of undulator spectral performance. As discussed below, the results confirm the intuition that achieving a 2° RMS phase error, or better, is important for maintaining high spectral brightness for the high NSLS-II harmonics (7, 9, and 11). These results also confirm the idea that the phase error effects become more significant as the ring emittance decreases.

12.7.1.6.1 Relative On-Axis Brightness for Harmonics 7, 9, and 11 vs. RMS Phase Errors for NSLS-II Undulators

Computer simulations of the relative on-axis brightness as a function of the RMS phase error were performed using the NSLS-II emittance and real measured magnetic fields of three undulators. Comparisons

were made to the spectral performance of the same undulators with hypothetical ideal magnetic fields. The results are detailed below and show, for example, that the 9th harmonic undulator radiation degrades by about 15% if the RMS phase error increases from 2.0° to 3.0°.

12.7.1.6.2 Conditions

The NSLS-II storage ring parameters for a 5 m long low-β insertion device straight section were used for these simulations. The following parameter values were used: emittances ε_h=0.55 nm, ε_v=0.01 nm, energy spread δE/E=0.1%, and β-functions β_h = 2.7m, β_v=0.945m. The resultant electron beam sizes and divergences are σ_h=38.5 μm, σ_v=3.1 μm, σ_h'=14.2 μrad, and σ_v'=3.2 μrad.

The following three undulators were studied:

- Linac Coherent Light Source undulator number 1 (LCLS #1), period length=3.0 cm, 113 periods; K and ϕ measured at 6.8 mm gap: K=3.50 and ϕ=3.54°
- Linac Coherent Light Source undulator number 2 (LCLS #2), period length=3.0 cm, 113 periods; K and ϕ measured at 6.8 mm gap: K=3.49 and ϕ=4.21°
- APS short undulator A (APS #40), K = 2.80, period length = 3.3 cm, 62 periods; K and ϕ measured at 10.5 mm gap: K = 2.80 and ϕ = 3.68°

Numerical calculations of the on-axis brightness for these three undulators were performed. In order to study the dependence on the RMS phase error, the LCLS undulator fields were scaled in both field strength (uniformly to a lower value) and period length to simulate a change of the RMS phase error (the RMS phase error decreases when the K value becomes smaller). Very minor adjustments to the on-axis view angle were applied, and as such, those fields represent real devices with true magnetic field errors. It is worth noting that for the LCLS undulators, the period length was scaled from 3.0 cm to 1.9 cm to simulate a shorter period-length undulator, such as the NSLS-II U19 CPMU hard x-ray undulator. This procedure allowed us to study undulators which have RMS phase errors covering the range 2.0° to 3.7°.

12.7.1.6.3 Results

The on-axis brightness of the 7th, 9th, and 11th harmonics, relative to the brightness of the corresponding harmonics of a hypothetical, ideal magnetic field undulator, is plotted in Figure 12.7.3 for the three undulators described above, simulated for their performance in the NSLS-II storage ring. The relative brightness of the 3rd and 5th harmonics is much closer to 100% and is not shown in this figure.

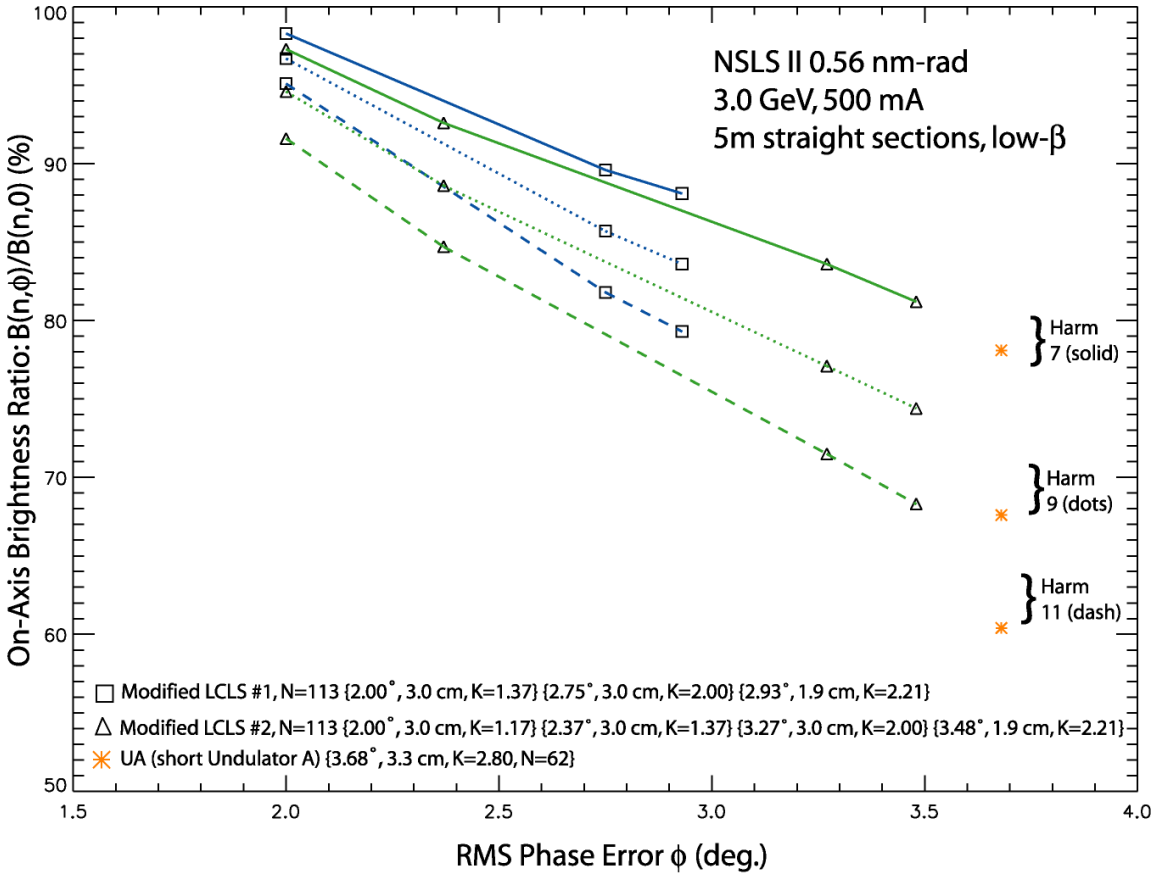

Figure 12.7.3 On-axis brightness of the 7th, 9th, and 11th harmonics of three undulators relative to the brightness of the corresponding harmonics of an ideal magnetic field undulator, as a function of the RMS phase error.

The key results of these simulations are as follows: improving the RMS phase error from 3.0° to 2.0° changes the relative brightness of the 7th harmonic from 86 to 98% (Δ_7 = 12% points), the 9th harmonic from 81 to 96% (Δ_9 = 15% points), and the 11th harmonic from 75 to 93% (Δ_{11} = 18% points).

12.7.1.6.4 Conclusions

The relative brightness of the NSLS-II undulator harmonics depends sensitively on the RMS phase error. The higher the harmonic number and the higher the RMS phase error, the faster is the rate of reduction. The rate of reduction is somewhat sensitive to the actual distribution of phase errors for real devices, but is much less sensitive to the actual K value or the undulator period length. For example, by improving the RMS phase error from 3.0° to 2.0°, the 9th harmonic would gain about 15%.

The effect of phase error becomes greater as the emittance of the storage ring decreases. For example, the performance drop for NSLS-II undulators would be 2 to 5% greater for harmonics 7–11 than for the same devices at APS, as a result of the smaller emittance of NSLS-II.

Future work on this subject should include simulations using the measured fields from recently built undulators around the world, including the 18 mm period undulator installed at NSLS beamline X25 in December 2005, which has a period length very close to the U19 CPMU proposed for NSLS-II and has a measured RMS phase error close to 2°.

12.7.1.7 Baseline CPMU Magnetic Design

The baseline design for the NSLS-II hard x-ray planar device is derived from the NSLS cryo-ready undulator developed for X25. The X25 mini-gap in-vacuum undulator has an 18 mm period length, a minimum magnetic gap of 5.6 mm and length of 1 m, and is designed to be operated at 150 K. The NSLS-II U19 CPMU will have a minimum gap of 5 mm and will be 3 m long, but most of its other requirements are similar to those for the X25 MGU. The main parameters are given in Table 12.7.2.

Table 8.2.3 shows the expected mechanical tolerances of the magnetic arrays.

Table 12.7.2 Mechanical Tolerances.

Item	Tolerance
Magnet/pole width [μm]	±100
Magnet height [μm]	± 25
Magnet thickness [μm]	±25
Pole height [μm]	± 25
Pole thickness [μm]	± 10
Pole-to-pole flatness [μm]	±10
Period [μm]	±10
Magnet array pitch/yaw/roll (relative) [μrad]	± 25
Magnet array horizontal/vertical rack [μm]	± 5
Gap control [μm]	± 5
Gap repeatability [μm]	± 5

The phase error for the device is required to be less than two degree RMS. Slight tapering, platen bowing, and other factors must be carefully controlled to achieve this level of phase error. As mentioned above, a novel gap measurement system using a commercial, high-precision, LED-based optical micrometer was incorporated in the X25 MGU to back up the linear encoders and to correct for gap changes due to differential contraction during cryogenic operation. The system monitors the magnet gap optically through viewports at either end of the MGU, ensuring gap accuracy of ±2 μm.

Figure 12.7.4 shows an isometric rendering of the MGU magnet arrays by Radia. Blue magnets have identical size and two different sized magnets are shown in green. Pieces in magenta represent permendur poles.

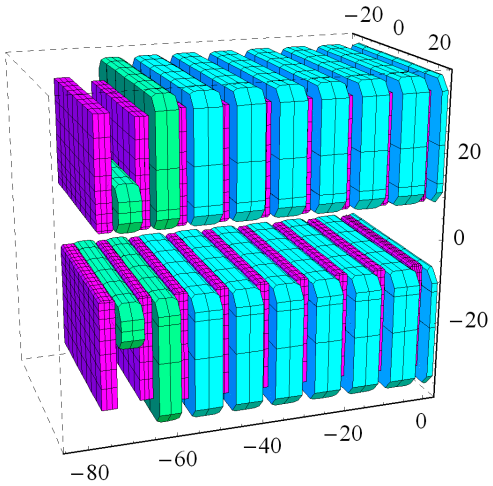

Figure 12.7.4 MGU magnet arrays. Only the first few periods are shown, for clarity. Units are millimeters.

The Radia simulations shown here were performed with a symmetrical model so the angular kick could be estimated. In the actual device we are likely to use an anti-symmetric structure to minimize the residual first integral. The values of magnet susceptibilities used are χ_m (para) = 0.02, χ_m (perp) = 0.42. The field and trajectory computed from the model are plotted in Figure 12.7.5 for gaps of a) 5.0 mm and b) 11.0 mm. The trajectory is calculated by a particle-tracking Runge-Kutta routine. The particle is launched with zero offset and angle (x = 0, x' = 0), and its position and angle are calculated every 0.53 mm (36 points per period). The gap dependence of the first integral is shown in Figure 12.7.6. The amount of change in the first integral found here can be easily compensated by external coils.

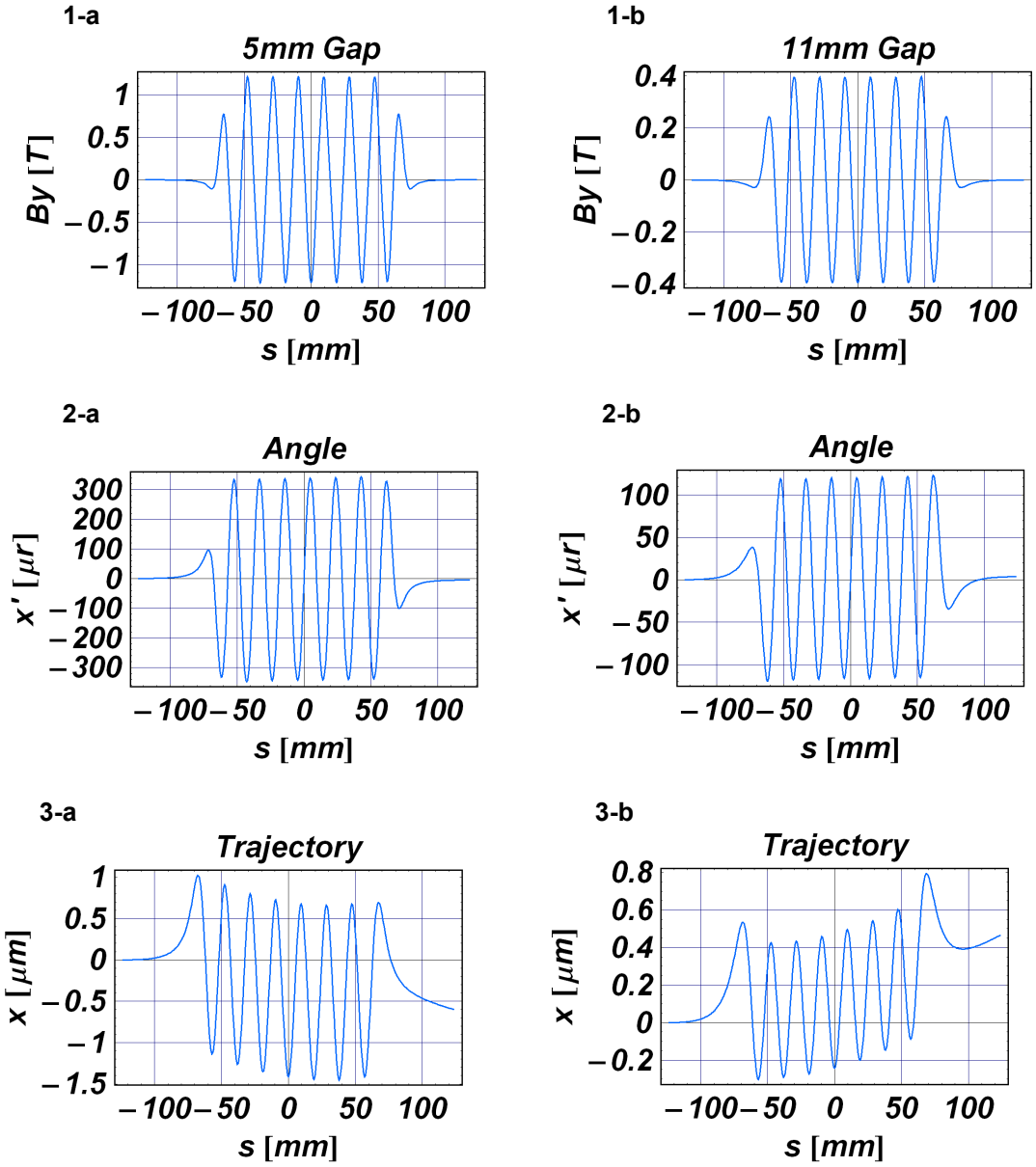

Figure 12.7.5 Gap dependence. Field, angle, and trajectory plots for the 7-period model for (column **a**) minimum gap (5.0 mm) and (column **b**) maximum operating gap (11.0 mm).

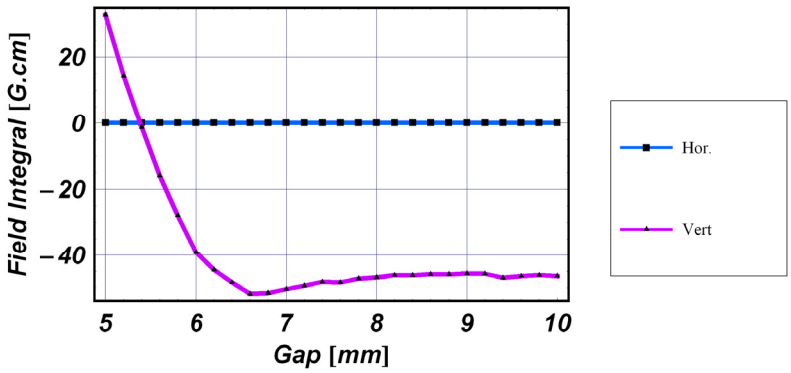

Figure 12.7.6 Gap dependence of the first integrals simulated for U19.

12.7.1.8 New Magnetic/Pole Materials Development

An avenue of further development of CPMUs is to investigate other rare-earth magnets that do not exhibit the spin re-orientation transition at 150K. For example, PrFeB has similar Br as NdFeB at room temperature, but its Br continues to increase further all the way down to 4K. PrFeB would permit use of liquid nitrogen to cool the CPMU to 77K and thereby attain an additional 5 to 7% increase in field. NEOMAX produced a few research samples of PrFeB several years ago, and again just recently. Although the material is not available commercially, we are discussing with NEOMAX and with SPring-8 the possibility of a PrFeB development project.

We will also investigate the use of exotic pole materials, such as oriented dysprosium, with a reported saturation flux density up to 3.5 Tesla at cryogenic temperatures. This opens the possibility of a CPMU built with PrFeB magnets and Dy poles, operating at 77K or lower with significantly higher performance than with NdFeB and permendur poles. This may ultimately reduce or eliminate the need for the complexity of superconducting undulators. This project will draw on the expertise in dysprosium and permanent magnet materials at the BNL Materials Science Department. If development of both PrFeB magnets and oriented Dy poles is successful, a short prototype undulator magnet module could be constructed and tested in our existing Superconducting Undulator Vertical Test Facility.

12.7.1.9 Vacuum and Mechanical Systems Development

A 3 m device will be constructed with three 1 m modules that are similar to the X25 MGU. The vacuum chamber is rectangular and opens along its length to facilitate magnetic field measurements and shimming. Most of the required vacuum components are mounted to this cover for easy access and for a cost-effective design. These components include ion pump/titanium sublimators, getter pumps, an RGA analyzer, a glow discharge cleaning system with associated pumping and view ports, an ion gauge, and bleed-up ports. The X25 system successfully achieved a pressure of less than 5×10^{-10} Torr, including magnets, after bakeout. The conceptual design in a CAD model is shown in Figure 12.7.7.

Techniques first demonstrated in the cryo-ready X25 MGU will be optimized and incorporated for the NSLS-II development program for the control system of the CPMU. Systems such as an in-vacuum gap separation system will be modeled that can provide precision gap control with negligible effects from external temperature fluctuations and ultimately demonstrate a cost-effective alternative to more conventional gap separation and control systems.

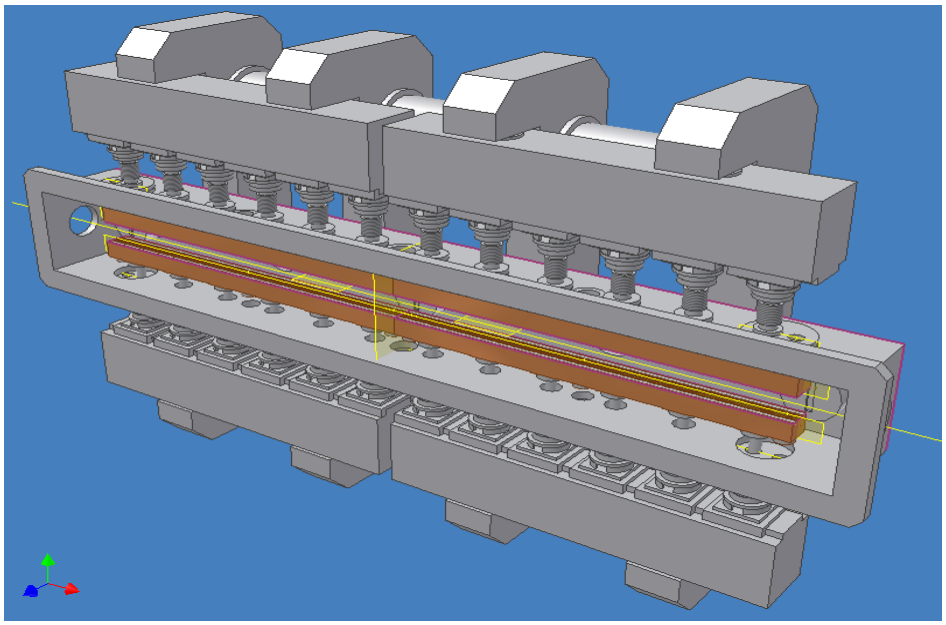

Figure 12.7.7 Conceptual design of U19.

12.7.1.10 CPMU Magnetic Measurement Systems Development

Two types of measurement systems are used to characterize the field quality of an insertion device at the magnetic measurement laboratory at NSLS. The first is a pulsed-wire measurement system that can be used to check the trajectories in both horizontal and vertical directions. It is also used to find the correct coil current of a Helmholz coil to cancel the earth field. The second type is a Hall probe mapping system. The Hall probe scan is done "on-the-fly," starting from a precise home position, acquiring the desired number of samples per undulator period.

One of the challenges for CPMU development is to establish an accurate low-temperature field measurement system. For properly designed undulators, the differences in field quality between room temperature and low temperature are expected to be small. However, it is essential that the field quality be verified at the actual operating temperature. A vertically oriented cryogenic magnetic measurement apparatus for prototype undulator models up to 0.4 m in length has been developed and used at NSLS [12.7.10]. In order to measure full-length devices in a horizontal orientation, a new measurement scheme must be developed. The magnetic measurement should be done in the vacuum vessel at the cold operating temperature, but not necessarily in UHV. Figures 12.7.8 and 12.7.9 delineate the concept of an in-vacuum, in-situ Hall probe mapper. It is mounted on the large rectangular front flange of the chamber. Hall probe position accuracy is maintained by a laser tracker and piezo controller.

For field integral measurements, an in-vacuum moving wire system has already been developed by ACCEL and ESRF. A similar mechanism can be used for a pulsed-wire system.

There is no convenient way to make in-situ (i.e., in-vacuum) field error corrections unless a remote-control magnet adjustment mechanism is incorporated in the magnetic arrays. In the absence of this development, field error correction must be performed iteratively, where each iteration requires a lengthy series of warm-up, venting, measurement, adjustment, pump-down, and cool-down steps. Our goal is minimize the number of such iterations by 1) designing the mechanical components to minimize the systematic field errors resulting from warm-up and cool-down, and 2) developing an efficient scheme of warm shimming and cold measurement. Ideally, field errors may track with temperature, so shimming at room temperature may suffice.

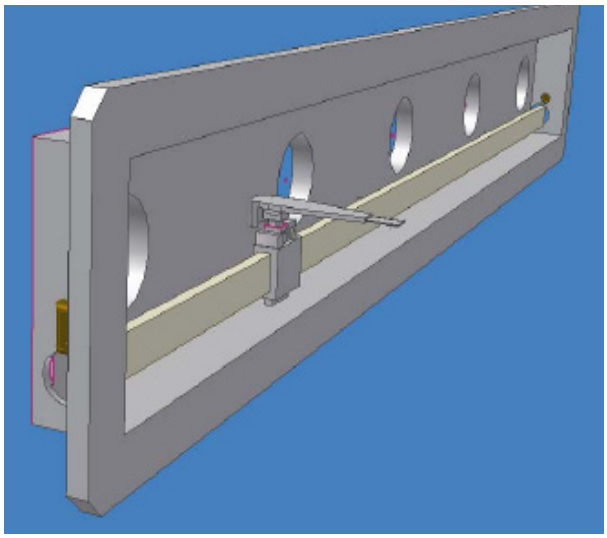

Figure 12.7.8 Hall probe mapper mounted on the flange cover.

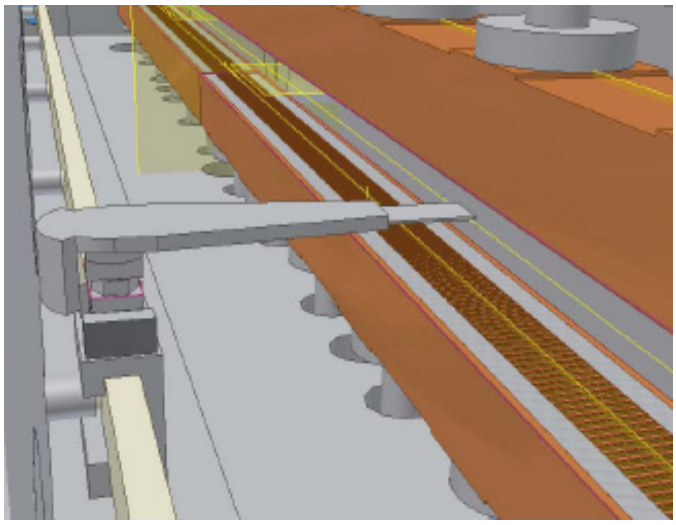

Figure 12.7.9 Mapper position with respect to the magnet arrays.

This cold magnetic field mapping system is essential for CPMU or HTSCU development. This system will be designed to be used primarily in the measurement laboratory but can also be used to perform in-situ measurements of insertion devices in remote locations such as a synchrotron tunnel. This system will incorporate a horizontal vacuum chamber that could accommodate either a CPMU or HTSCU that is 3+ m long and that demonstrates efficient installation of in-situ shimming and measurement of the magnet modules without the need for chamber reassembly. Cryogenic hall probe, pulsed/vibrating wire, and moving wire will be investigated. The research phase will demonstrate the incorporation of an in-vacuum measuring system with the vacuum vessel and precision gap separation mechanisms.

The goal of this development is to demonstrate cryogenic undulator measurement concepts that will ultimately be used in the characterization, shimming, and in-situ measurements of all the production in-vacuum and cryogenic insertion devices.

12.7.2 Variable Polarization Device

The variable polarization undulator, also known as an elliptically polarized undulator, EPU, is becoming more popular, as its impact on beam dynamics can now be controlled to an acceptable level. Currently, no in-vacuum EPU has been constructed, because of the difficulty of having moving parts and a strong force in a UHV environment. Therefore, the baseline design for NSLS-II will be the permanent magnet out-of-vacuum EPU45 and EPU100 devices described in Chapter 8, but R&D will be carried out to investigate in-vacuum EPU designs.

Various schemes to generate variably polarized light from an insertion device have been proposed. An electromagnet-based design that switches the polarity cannot cover the required photon energy range (250 eV–2 keV). The most popular design, based on PM technology, is the Advanced Planar Polarized Light Emitter (APPLE) type [12.7.11]. It has been popular because it can generate all the possible polarization states with the minimum number of magnets. However, it also has a few deficiencies. Strong multipole components inherent to the design would reduce the dynamic aperture of the machine. This effect is due to the fact that horizontal field and vertical field are coupled, so static optimization for different gap and phase is difficult. In long-period devices, the electron's wiggle amplitude can be large enough for the field rolloff to affect the trajectory and result in a so-called "dynamic field integral," which is not measured by stretched

wires or long coils. Recent efforts by various laboratories have mitigated these problems for limited types of operations [12.7.12].

There is an alternative design proposed for HiSOR by SPring-8 [12.7.13]. It separates the magnets for horizontal and vertical field, for ease of tuning as well as more moderate skew multipoles, at the expense of weaker achievable horizontal field. Detailed tracking studies will be carried out to decide which type of device is appropriate for NSLS-II.

Another concern for NSLS-II EPUs is the possible demagnetization of the permanent magnets by the use of the APS-style narrow gap vacuum chamber. Improvements to the vacuum chamber design will be investigated in order to minimize the source of radiation at the extremities of the chamber.

12.7.2.1 Anisotropy of Permanent Magnets

Rare-earth magnets used for insertion devices have permeability close to unity, so that, to first order, the magnetic induction from individual magnet blocks can be superposed to obtain the total field. However, more careful analysis shows that there is anisotropy in those magnets. The components of the permeability that are parallel to the preferred direction of magnetization (easy axis), and perpendicular to this direction, are different and lager than unity. The magnetic susceptibility χ_m and polarization J are defined as follows:

$$B = \mu H = \mu_0 \mu_r H = \mu_0 (\chi_m + 1) H , \quad (12.7\text{-}3)$$

$$J = \mu_0 \chi_m H \quad (12.7\text{-}4)$$

where B is magnetic induction, H is magnetic field strength, μ_0 the permeability of vacuum, and μ_r is the relative permeability defined for convenience.

The permeability can vary at different points on the hysteresis curve. For example, the value at the beginning of magnetization is termed initial permeability, and the largest gradient in the B-H curve is called maximum permeability. What is important in a magnetic circuit is the reversible or recoil permeability, which is the slope of a minor loop in the second quadrant. The recoil permeability is usually approximated by the slope of the major loop at H = 0. For NEOMAX 42AH, the susceptibility is estimated by the slope of the J-H curve around H = 0. The estimated values of susceptibilities from these curves are:

$$\chi_m \text{ (para)} = 0.02, \ \chi_m \text{ (perp)} = 0.42. \quad (12.7\text{-}5)$$

These values indicate that in the region where the magnetic flux lines deviate from the preferred direction of magnetization, the material can be nonlinear. For planar insertion devices, this region corresponds mostly to end sections, which determines the gap dependence of the field integral, in practical terms. However, in most EPUs, the field directions inside magnets vary greatly, depending on the array phase. For the CPMU these values will need to be measured at the operating temperature, in order to be valid.

12.7.2.2 Advanced Options

In-vacuum EPU is still an R&D subject. The performance of any type of ID strongly depends on the available minimum magnetic gap. Development of a 2.5 m long in-vacuum EPU is under consideration. If initiated, BNL would assemble magnet and pole materials, develop in-vacuum gap separation and magnet module axial position actuators, and procure a vessel and undulator support system. Measurements and characterization of the EPU fields under various gaps and phases would be made, as well as field corrections. The in-vacuum EPU could then be installed for the X-1 beam line of NSLS to verify performance prior to the move to NSLS-II. The goal of this development would be to advance the state of the art in EPU technology, to demonstrate the first in-vacuum EPU, to resolve the uncertainty in the methods of measurement and

shimming of EPUs to permit reliable and cost-effective operation, and to perfect a new class of insertion device, the in-vacuum EPU, that can be offered to meet the needs of NSLS-II users.

To switch the helicities at higher than 1 Hz, a tandem structure is needed so that light with opposite helicities is produced simultaneously for various switching schemes. In this case, each ID is located away from the center and the required beam stay-clear gap would increase. If a slower switching frequency is tolerated, one longer device with mechanical phase change is possible. Another possibility is to set up two helical undulators in tandem and have a phase shifter between them to change the resulting polarization [12.7.14]. In this case, two helical undulators can be in-vacuum type if limited tuning range can be tolerated. Table 12.7.3 shows the characteristics of an APPLE-II type EPU.

Table 12.7.3 Characteristics of an APPLE-II Type EPU. Assumed Br of the magnets is 1.35T.

Period Length (mm)	Magnetic Gap (mm)	Helical ModePeak Field (Bx = By)	EffectiveKx / Ky	Linear ModeEffective Ky
40	6.5	0.87	3.2	4.87
42	8	0.77	3.0	4.76
45	10	0.68	2.87	4.67
45	11	0.62	2.6	4.38

12.7.2.3 EPU45 (APPLE-II) Magnetic Design

One possibility is to install twin devices in an 8 m straight section. Assume that we can have a 5 mm vertical aperture for a 3 m device placed at the center of the 5 m straight, with vertical beta function equal to 1 m at the insertion center. In this case, the ring aperture (A) is:

$$A = \frac{gap}{\sqrt{\beta(end)}} = \frac{gap}{\sqrt{\beta_0 + (end)^2 / \beta_0}} = \frac{5mm}{\sqrt{(1+1.5^2)m}} = 2.77mm/\sqrt{m}\,. \tag{12.7-6}$$

We must verify that this is sufficient, but once we determine that this is acceptable, the required aperture y for an insertion device of length L placed at the center of a straight with beta-function β_0 at the center is determined to be

$$y = A\sqrt{\beta_0 + \frac{(L/2)^2}{\beta_0}} \tag{12.7-7}$$

For the 8 m straights β_0 = 3 m, we find the required vertical aperture is 7.4 mm at the half length of 3. 5 m. An 8 mm aperture chamber at APS allows 2.5 mm extra for the magnetic gap of their insertion device. Therefore, we will assume that the magnetic gap of the NSLS-II insertion device is close to 10 mm.

The minimum photon energy to be covered is 250 eV. An EPU45 with an APPLE-II type configuration shows the characteristics listed in Table 12.7.4. Here, the remanent fields of the NdFeB magnets are assumed to be 1.35 T.

Table 12.7.4 APPLE-II Type EPU45 Parameters.

Period length [mm]	45
Peak field (helical mode: v/h) [T]	0.68 / 0.68
Effective K	2.87
Minimum photon energy in helical mode [eV]	206
Minimum gap [mm]	10
Magnet horizontal size [mm]	50
Magnet vertical size [mm]	45
Remanent field (B_r) [T]	1.35

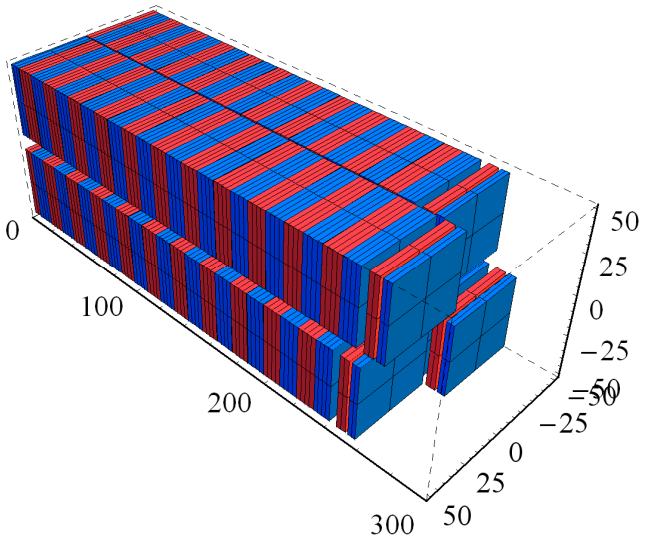

Figure 12.7.10 Magnet arrays of EPU45. Only the first few periods are shown for clarity. Units are millimeters. Vertically magnetized magnets are in red and horizontally magnetized magnets are in blue.

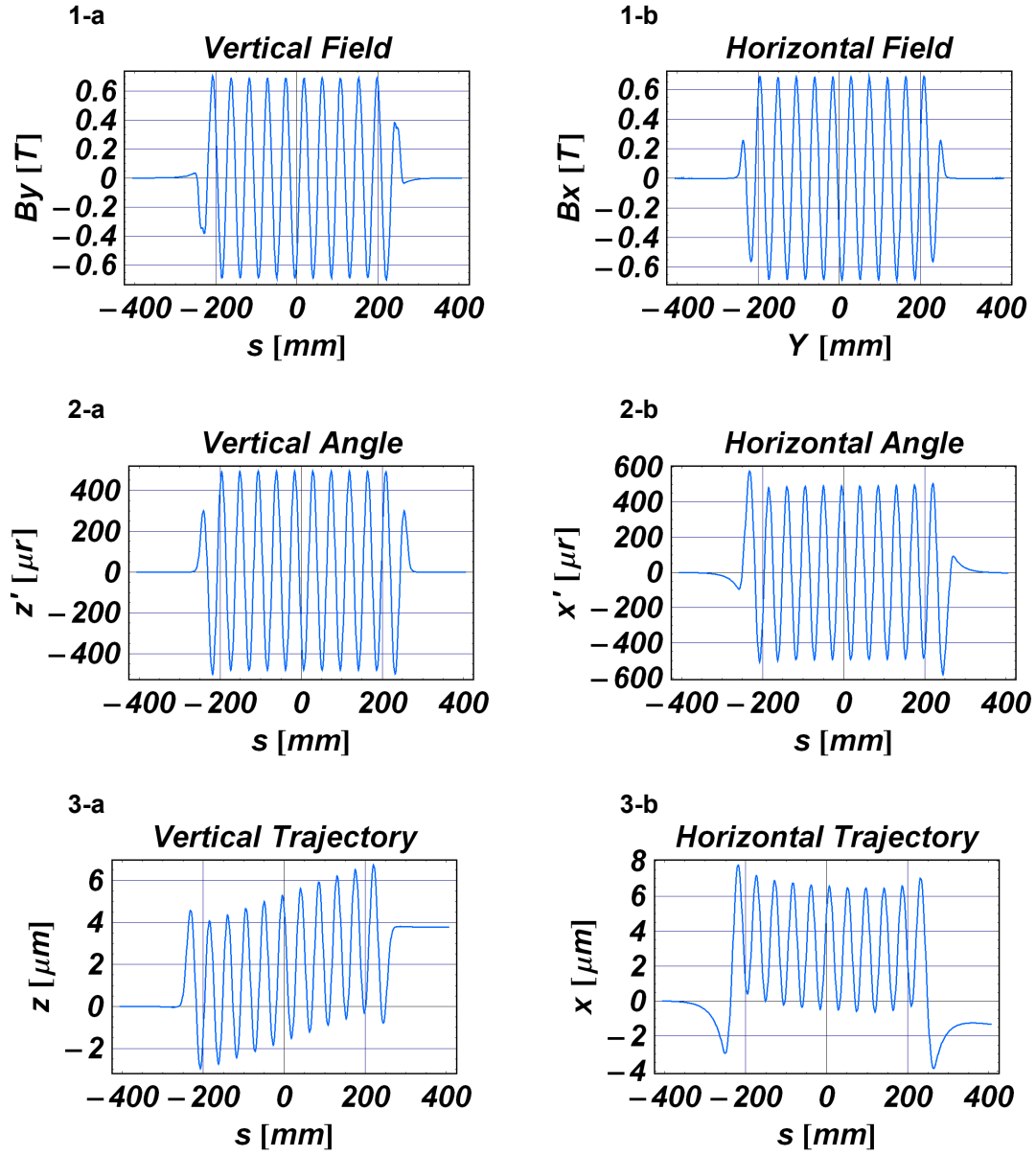

Figure 12.7.11 Field, angle and trajectory plots for the 11-period model of EPU45 in helical mode. **a)** vertical field, horizontal angle, horizontal trajectory and **b)** horizontal field, vertical angle, and vertical trajectory at a gap of 10 mm.

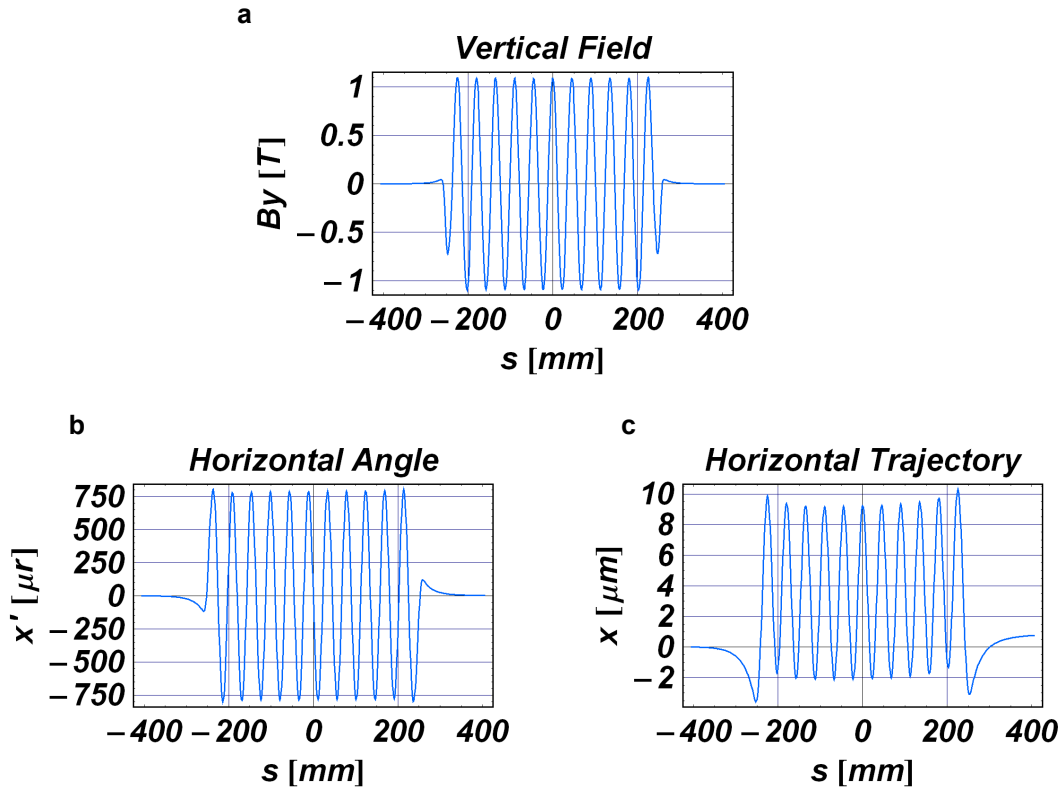

Figure 12.7.12 Field, angle, and trajectory plots for the 11-period model of EPU45 in linear mode. **a)** vertical field, **b)** horizontal angle, **c)** horizontal trajectory at a gap of 10mm.

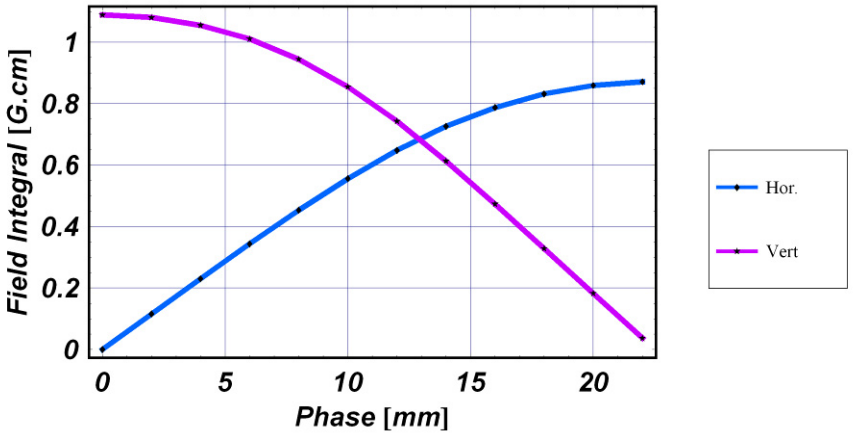

Figure 12.7.13
Fields vs. phase.

F

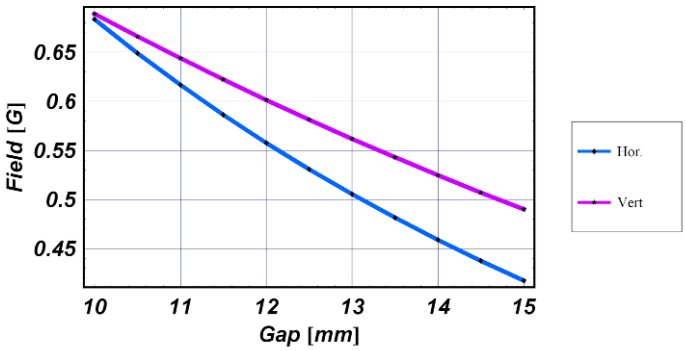

Figure 12.7.14 Fields vs. gap in helical mode.

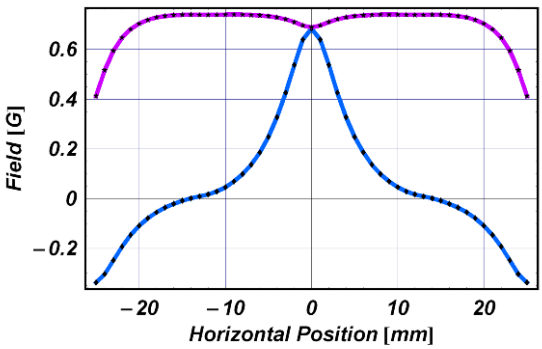

Figure 12.7.15 Fields vs. horizontal position at the origin in helical mode.

12.7.2.4 EPU50 (HiSOR) Magnetic Design

To alleviate a highly sharp horizontal field profile and the coupling of vertical and horizontal fields from the same magnet, a new design with three magnet arrays in each jaw has been proposed and implemented at UVSOR and HiSOR in Japan. Unlike the APPLE-II design, one array in the center produces vertical field and two arrays on the sides generate horizontal field. Therefore, each type can be separately shimmed to perfection. The horizontal field profile is more benign than that from APPLE-II. The parameters for the HiSOR design are shown in Table 12.7.5, and a Radia drawing shows the design (see Figure 12.7.16).

Table 12.7.5 HiSOR-Type EPU50 Parameters.

Period Length	5 mm
Peak Field (helical mode: v/h)	0.53 / 0.53T
Effective K	2.49
Minimum photon energy in helical mode	240 eV
Minimum gap	10 mm
Side Magnet Size (H/V)	50 / 45 mm
Center Magnet Width	14 mm
Remanent Field (Br)	1.35T

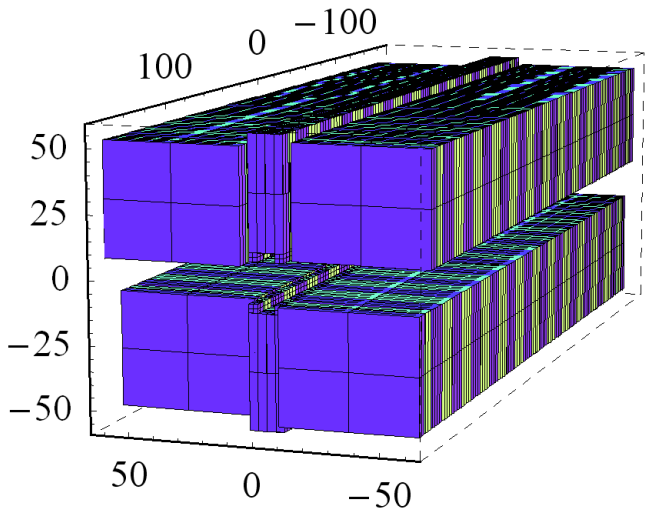

Figure 12.7.16 Magnet arrays of HiSOR-EPU50. Only the first few periods are shown, for clarity. Units are millimeters. Vertically magnetized magnets are in light green and horizontally magnetized magnets are in purple.

One disadvantage of the HiSOR design is that the maximum horizontal field is weaker than that of the APPLE-II for the same period length, due to the increased distance between the two arrays. Hence, slightly longer period length is required to obtain the same photon energy as with the APPLE-II design. If vertical linear polarization is needed, the vertical arrays can be shifted out of phase. However, some longitudinal components remain at the extremities, and tracking studies are needed to determine the detrimental effect.

The grooved-shape magnets in the center arrays improve the vertical field uniformity (see Figure 12.7.17).

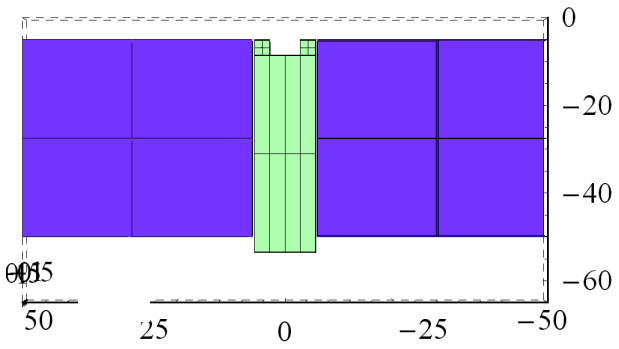

Figure 12.7.17 Cross-section of a magnetic array. Light green is for the vertical field and purple is for the horizontal.

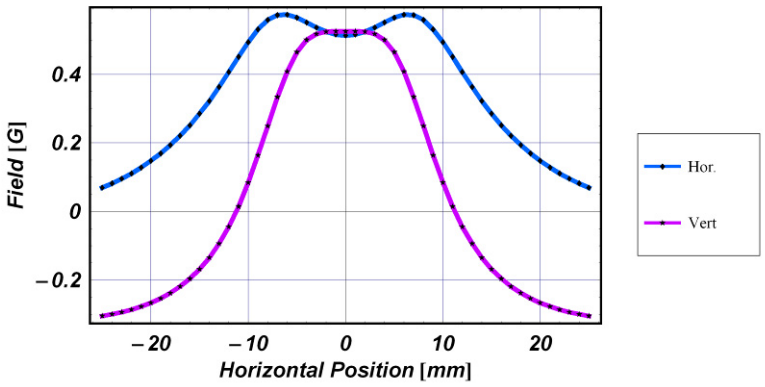

Figure 12.7.18 Field profile vs. horizontal position in helical mode.

12.7.3 Damping Wigglers

In Chapter 7 we defined two key parameters of the Damping Wigglers (DWs): a peak field of 1.8 T and an eventual total length of 35 m. The peak field value was chosen to be high enough to radiate sufficient power for adequate emittance damping, but not so high as to create excessive energy spread. The DWs are also useful as high-flux, high-brightness broadband sources in the hard x-ray range.

The initial installed length of DWs will be 21 m, composed of three wigglers, each 7 m long. A third key design parameter is the minimum magnetic gap. The estimated vertical stay-clear aperture at ±3.5 m from the center of the 8 m straight section is 10 mm. Allowing for beamtube wall thickness of 1.5 mm, plus 1 mm clearance between the beamtube and the magnet poles, we obtain a minimum magnetic gap of 15 mm. From empirical design formulas developed by Elleaume for various planar undulator (wiggler) technologies [12.7.15], we find that 1.8 T peak field can be produced at that gap by a conventional PM-hybrid wiggler with a period of 100 mm, using high-field NdFeB magnets (Br = 1.35 T) and vanadium permendur poles. With less expensive low-carbon steel poles, a somewhat longer period (~110 mm) would be required. In either case, these parameters are in the realm of wigglers that have been produced by industry. Of course, the 7 m length may be comprised of two 3.5 m long DWs, or three 2.3 m long units in tandem.

Unlike users of undulator radiation, wiggler users expect a broad, dipole-like spectrum. Therefore, minimizing phase errors is not important. Shimming of DWs is concerned mainly with trajectory straightness. In fact, gap taper, or variation in pole periodicity are sometimes introduced in wigglers intentionally to spoil coherence and to smooth the spectrum.

DWs must meet the same integrated dipole and multipole error specifications imposed on all IDs. However, since they will operate at fixed gap, these errors can be shimmed out more easily than in variable-gap IDs, without concern about gap-dependence. The next sections discuss some additional design considerations for DWs.

12.7.3.1 Dynamic Field Integral

The integrated field seen by sinusoidally wiggling electrons [12.7.16] is

$$\int B_y ds \approx \frac{-L}{2k^2 B\rho} B_y(x_i) \frac{dB_y(x_i)}{dx} , \qquad (12.7\text{-}8)$$

where L is the device length, k_w is the 2ρ/period length, ρ is the radius of curvature of the trajectory, and x_i is the horizontal displacement of the electron. This is called dynamic field integral, and it scales as ID period squared and as the derivative of the transverse field roll-off. An important aspect of optimization of long-period wiggler magnetics is how to determine the necessary transverse pole width to minimize the effect of the dynamic field integral effect while minimizing attractive force, which is proportional to the magnet area, and keeping the cost as low as possible. Beamtracking reveals the detrimental effect of this integral on the beam dynamics.

12.7.3.2 Attractive Force and Size/Cost Challenges of the Damping Wigglers

For NSLS-II, the damping wigglers will be used as a broadband source. The design calls for 7 m of damping wiggler in an 8 m straight. In reality, it is easier to combine two 3.5 m devices or five 1.4 m units. The approximate attractive force of a linear device is given as follows:

$$F_{ID} \approx \frac{B_y^2 WL}{4\mu_0}, \tag{12.7-9}$$

where W is the horizontal width of poles or magnets, L is the total length of the device, and μ_0 is the permeability of the vacuum. With W = 100 mm and B_{oy} = 1.8 T, the attractive force per meter is about 65 kN. A variable-gap device must have a structure that is rigid enough to not create an intolerable multipole field due to defection. As this is an out-of-vacuum device, many different designs have worked properly in storage rings.

Wigglers of this type, from 2 to 4 meters in length, have been designed and build to specification by industry for many synchrotrons. The mechanical structures to support and control the gap of these wigglers are generally massive and expensive. A detailed design study will consider alternative magnet configurations that could lessen the need for these massive structures. The goal of this project is to design a magnet configuration that can utilize a relatively compact, lower-cost magnet support system that ultimately could reduce the cost of these wigglers significantly.

12.7.3.3 Non-Sinusoidal Field Effect

Another issue for long-period undulators is the deviation from sinusoidal field, which effectively reduces the deflection parameter. (This is not an issue for wigglers, where the critical energy depends on peak field only.) We examine a hybrid undulator with permendur poles with the parameters shown in Table 12.7.6.

Table 12.7.6 U100 Wiggler Parameters.

Period length [mm]	100
Nominal peak field [T]	1.8
Remanent field (B_r) [T]	1.35
Gap [mm]	1 5
Magnet horizontal size [mm]	150
Magnet vertical size [mm]	100
Pole horizontal size [mm]	100
Pole vertical size [mm]	75
Air gap [mm]	0.1
Chamfer (magnet) [mm]	2.0
Chamfer (pole) [mm]	1.5
Corner cut (magnet) [mm]	3.0
Gap offset (magnet) [mm]	0.25

By varying the pole thickness while keeping fixed the total period length, we have calculated the peak magnetic field (induction) and effective K_y, as shown in Table 12.7.7. When the pole thickness is reduced from 19 to 18 mm, the peak field increases from 1.80 to 1.82 T and effective K_y decreases from 15.8 to 15.7. This indicates that the field deviates too much from the sinusoidal form.

Table 12.7.7 Comparison of Peak K_y and Effective K_y with Varying Pole Width.

Pole Thickness (mm)	Peak Field (T)	Peak Ky	Effective Ky
18	1.82	17.0	15.7
19	1.80	16.8	15.8
20	1.77	16.5	15.8
21	1.72	16.1	15.6

There are various ways to obtain a field closer to pure sinusoidal shape than the example above. One relatively simple solution is to add side magnets to boost the field while the pole thickness is increased. Wedge-shaped poles are another way to boost the field, in contrast to simple rectangular pieces. In either case, the cost would increase due to extra complexities.

12.7.3.4 Baseline Damping Wiggler Design

A conventional hybrid structure with permendur poles has been chosen for the NSLS-II device. Soft iron poles are significantly cheaper than permendur but produce inferior results, requiring complicating compensations such as side/back magnets or nonrectangular poles and magnets to achieve the required field (1.8 T) with a given magnet gap (15 mm). Figure 12.7.19 is an isometric rendering of the U19 magnet arrays by Radia. The magnets shown in magenta magnets have identical size; two different sized magnets are shown in green. Pieces in yellow represent permendur poles. Figure 12.7.20 shows the end view of the array.

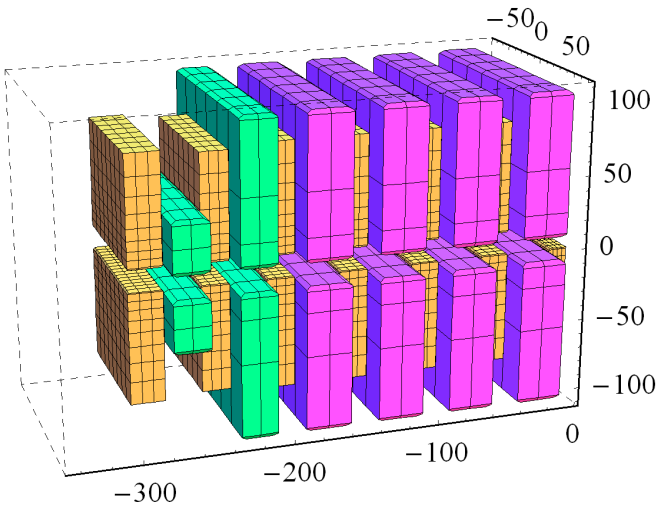

Figure 12.7.19 Magnet arrays of U100. Only the first few periods are shown, for clarity. Units are millimeters.

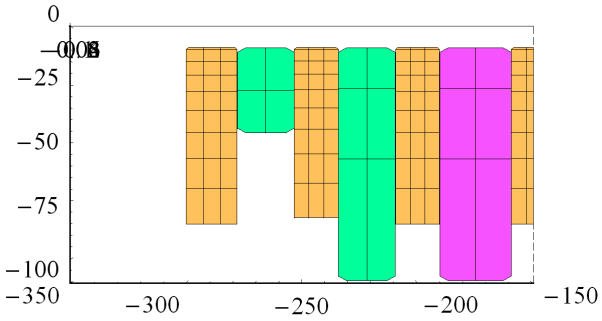

Figure 12.7.20 End view of U100.

The field and trajectory computed from the model are plotted in Figure 12.7.21, for a gap of 15 mm. The trajectory is calculated by a particle-tracking Runge-Kutta routine. The particle is launched with zero offset and angle (x = 0, x' = 0), and its position and angle are calculated every 2.78 mm (36 points per period). Gap dependence of its first integral is shown in Figure 12.7.22. The amount of change in the first integral can be easily compensated by external coils.

a

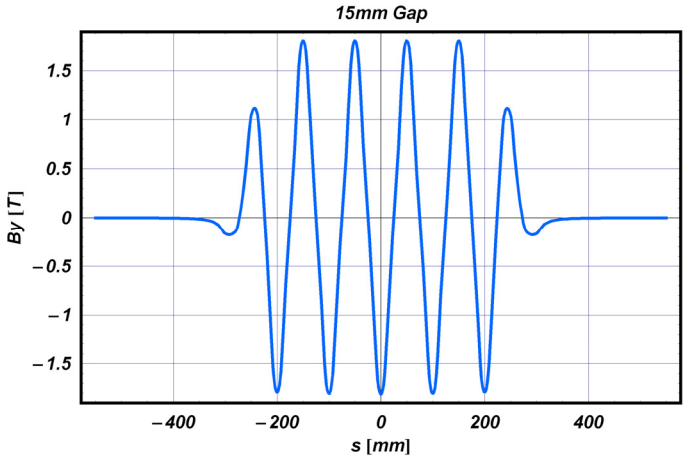

Figure 12.7.21 Field, angle, and trajectory plots for the five-period model of U100.

a) Vertical field.

b

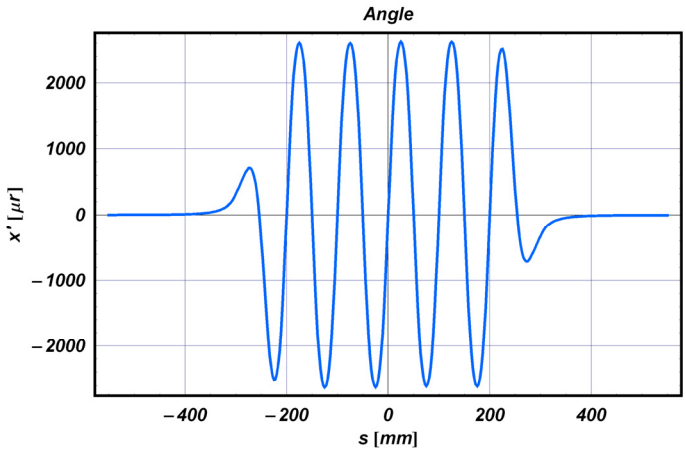

b) Horizontal angle.

c

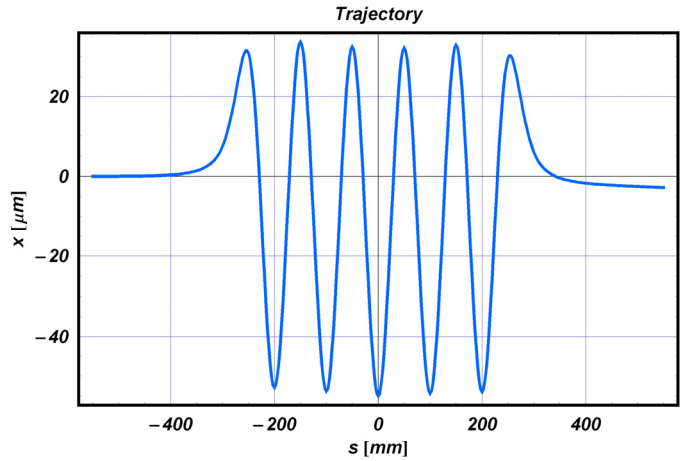

c) Horizontal trajectory at a gap of 10 mm.

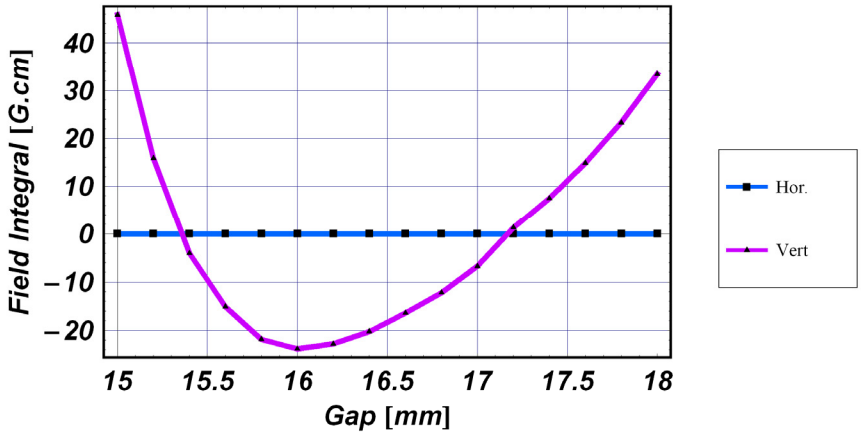

Figure 12.7.22 First field integral dependence on the gap.

12.7.3.5 R&D Elements for DW Development

Superconducting devices, especially HTSC versions, can be considered as an alternative choice for DWs. However, these DWs are an integral part of the light source lattice and any failure would result in the degradation of emittance, which affects all the users in the facility. Therefore, it is essential to achieve extremely high reliability for the HTSC-based DWs to be considered as an alternative for PM-based DWs. Extensive reliability studies will be necessary if this option is pursued.

Another subject is a novel gap separation mechanism, which should simplify the mechanical structure of the device. Attractive force for wiggler magnets is much larger than that by an undulator, so conventional structures tend to be very rigid and heavy in order to avoid deflection. As NSLS-II DWs are presumed to be fixed-gap devices, no strict requirement for gap parallel is required for the open position. One option is the scheme employed at the Source Development Laboratory at BNL, which utilizes inner and outer cages with roller bearings. Other possibilities will be considered.

12.7.4 Insertion Devices for Future Consideration

In this section we briefly discuss three other types of insertion devices that will be explored in our R&D program. If these prove feasible, they would provide a number of benefits and will be considered for future installation at NSLS-II.

12.7.4.1 Quasi-Periodic Undulator

Undulators designed to produce tunable vacuum ultra-violet and soft x-rays are of necessity long-period devices with period lengths of 40 to 100 mm or more. Because the characteristic K-parameter is proportional to the product of peak field and period, long-period undulators have necessarily high K values. Planar and elliptical undulators with high K-values produce spectra rich in harmonics (primarily odd-integer harmonics, since even harmonics are suppressed on-axis). In fact, the first few harmonics produced by high-K IDs have higher brightness and generate more SR power then the fundamental. If the user's monochromator is tuned to the fundamental, unwanted harmonics corresponding to higher orders of the monochromator pass through the exit slit unimpeded, polluting the monochromatic light and imposing an excessive heat load on optical components.

The Quasi-Periodic Undulator [12.7.17] was developed to overcome this problem. As the undulator's field amplitude pattern is altered, integer harmonics can be suppressed and replaced by noninteger harmonics. The latter do not coincide with higher orders of the monochromator and do not pass through the exit slit. The transmitted light is then purely monochromatic, and sensitive optics are protected. The monochromator must still absorb the unwanted harmonic power somewhere, but this can be accomplished by cooled absorbers at the exit slit. As with a conventional undulator, the monochromator can be tuned to any of the noninteger harmonics of the QPU to extend the spectral coverage of the instrument.

To date, several Pure Permanent Magnet QPU structures have been built. The QPU concept has been applied to both planar and APPLE-II type IDs. In circular polarization mode, the APPLE-II generates only fundamental radiation on-axis, so the QPU is of no benefit in that case. But in planar and elliptical modes, the quasi-periodicity helps manage the harmonic power and improves spectral purity, as described above.

12.7.4.2 Superconducting Wiggler

Higher photon energies (above 20 keV) can be effectively covered by a superconducting wiggler at NSLS-II. For a field range of 3.5 T, 60 mm period length, and a 10 mm magnetic gap, low-temperature SCW technology is now well established. However, achieving 6.0 T with the same period and gap will be a challenging task. In contrast, devices based on the use of **h**igh-**t**emperature **s**uper**c**onductors are a very promising approach for medium-field wigglers and would reduce the cost of both construction and operation. However, the current density now available for HTSC wire remains inadequate to produce the necessary field. Thus, the baseline design for the NSLS-II SCU will be the SCW60 device described in Chapter 8, which is based on conventional LTSC technology, but R&D will be carried out to investigate HTSC wiggler designs.

12.7.4.3 Superconducting Undulator

The first superconducting undulator in an electron storage ring was installed at LURE, Orsay in 1979. Since then, various devices for FELs have been developed [12.7.19]. In the past fifteen years, IVUs have been the primary device for short-period undulators. One of the reasons for not using SCUs in the storage ring is the difficulty of opening the necessary gap for injection. A new SCU with a variable gap mechanism has been in operation at ANKA [12.7.20] for the past few years. It has a rather complicated two-vacuum vessel structure, one vacuum for UHV and the other for insulation. The vessels are separated by 300μm stainless steel foil. The required performance was barely achieved due to 1) excessive heat load, which reduced the critical current achievable, and 2) a structural problem that contributed to the degradation of phase errors.

SCUs with conventional NbTi wire face serious problems to reduce the heat load onto the device's cold mass to a level manageable with modern cryocoolers. Unfortunately, state-of-the-art cryocoolers have a cooling capacity of less than a few watts at 4K. What is needed is a different type of LTSC wire that can withstand higher operating temperatures. One approach is to use Nb_3Sn; this is being pursued by the ALS group [12.7.21]. This type of wire is best suited for high-field applications. However, it is difficult to create the precise structure required for undulators, due to the wind and react process. Another approach is to use APC NbTi wire, which is supposed to be operated at much higher current density than conventional NbTi wire. Using this approach, extra space for heat shielding may be available for a fixed-gap vacuum chamber.

Even with these developments, SCUs based on LTSC technology will still have substantial thermal challenges. It may be that SCUs will not be viable until future developments in HTSC technology make it possible to manufacture an HTSC device. There is reason to be optimistic about this, and the NSLS-II project will monitor HTSC industry developments.

Another issue for SCUs is field correction. Extra wiring to correct phase errors has been attempted, but distributed integrated multipole corrections appear to be difficult. They might require correction at the end of the device. These also are issues for future development.

12.7.4.4 Revolver Type

If one type of magnetic array cannot satisfy the user's requirement, two or more different arrays could be used interchangeably, in a "revolver" type undulator system [12.7.18]. Revolver designs have been built at SPring-8 and ESRF and are operating reliably. In-vacuum revolver undulator was also developed by SPring-8 and installed at Pohang Light Source in Korea. This is a subject for future consideration, depending on the user requirements.

References

[12.7.1] T. Tanabe, et al., "Development of an In-Vacuum Minipole Undulator Array for National Synchrotron Light Source In-Vacuum Undulator," *Rev. Sci. Instrum*. 69 (1), pp 18 – 24, (1998).

[12.7.2] H. Kitamura, "Recent development of insertion devices at SPring-8," *Nuc. Instr. & Meth. A* 467-468 (2001) p 110.

[12.7.3] T. Hara, et al., "Cryogenic permanent undulators," *Phys. Rev. ST*, Acc. and Beam, Vol. 7, p.050720 (2004).

[12.7.4] R. Rossmanith, et. al., "A Year's Experience with a Superconducting Undulator in the Storage Ring Anka," Proc. 2006 European Particle Accelerator Conference, Edinburgh, Scotland (2006).

[12.7.5] S. Chouhan, et al, "Research and Development of Variable Polarization Superconducting Undulator at theNSLS," Proc. 2005 Particle Accelerator Conference, Knoxville, USA (2005).

[12.7.6] M. Sagawa, et al., "Magnetic properties of rare-earth-iron-boron permanent materials," *J. Appl. Phys.* 57 (1985) pp 4094.

[12.7.7] T. Tanabe, et al., "X-25 cryo-ready in-vacuum undulator at the NSLS," AIP SRI2006 conference proceedings (to be published).

[12.7.8] O. Chubar, P. Elleaume, and J. Chavanne, *J. Sync. Rad*. 5, pp. 481–484 (1998).

[12.7.9] J. Chavanne, et al., "End field structures for linear/helical insertion devices," Proc. 1999 Particle Accelerator Conference, New York p 2665 (2005).

[12.7.10] D. Harder, et al., "Magnetic measurement system for the NSLS superconducting undulator vertical test facility," Proc. 2005 Particle Accelerator Conference, Knoxville, USA (2005).

[12.7.11] S. Sasaki , et al., "A new undulator generating variably polarized radiation," *Jpn. J. Appl. Phys*. 31 (1992) L1794.

[12.7.12] J. Bahrt, et al., "Preparing the BESSY APPLE-undulators for top-up operation," AIP SRI2006 conference proceedings (to be published).

[12.7.13] A. Hiraya, et al., "Undulator at HiSOR–A compact racetrack-type ring," *J. Sync. Rad.* (1998) 5, pp 445.

[12.7.14] T. Hara, et. al., "SPring-8 twin helical undulator," *J. Sync. Rad*. (1998) 5, pp426.

[12.7.15] P. Elleaume, et. al., "Design considerations for 1 Å SASE undulator," *Nuc. Instr. & Meth A* 455 (2000) p. 503.

[12.7.16] J. Safranek, et. al., "Nonlinear dynamics in a SPEAR wiggler," *Phys. Rev. ST*, Acc. and Beam, Vol. 5, p.010701 (2002).

[12.7.17] S. Sakaki, et al., "Conceptual design of quasiperiodic undulator," *Rev. Sci. Instrum*. 66 (2), p 1953 (1995).

[12.7.18] H. Kitamura, et. al., "Recent developments of insertion devices at SPring-8," NIM-A, 467, (2001), pp 110.

[12.7.19] G. Ingold, et al., "Fabrication of a high-field short-period superconducting undulator," *Nuc. Instr. & Meth. A* 375 (1996) p. 451.

[12.7.20] A. Bernhard, et al., "Planar and Planar Helical Superconductive Undulators for Storage Rings: State of the art," Proc. 2004 European Particle Accelerator Conference, Lucerne (2004).

[12.7.21] S. Prestemon, et al., "Design and evaluation of a short period Nb3Sn superconducting undulator prototype," Proceed. 2003 Particle Accelerator Conference, Portland, U.S.A. p 1032 (2003).